Investigation of range verification in carbon ion therapy using Monte Carlo simulation

By

ANANTA RAJ CHALISE

Presented to the Faculty of the Graduate School of

The University of Texas at Arlington in Partial Fulfillment

of the Requirements for the Degree of

DOCTOR OF PHILOSOPHY

THE UNIVERSITY OF TEXAS AT ARLINGTON

August 10, 2020

Supervising Committee:

Dr. Mingwu Jin, Supervising Professor

Dr. Yujie Chi, Supervising Professor

Dr. Wei Chen

Dr. Qiming Zhang

Dr. Amir Shahmoradi

Dedicated to:

My grandma Talkumari Acharya

ACKNOWLEDGMENTS

The success of this dissertation, excluding my own effort, depended largely on the guidance, support and encouragement of many helping hands.

Foremost, I would like to express my sincere gratitude to my respected advisors Dr. Mingwu Jin and Dr. Yujie Chi, for their excellent guidance, patience, constant motivation, enthusiasm, knowledge and providing me with an excellent atmosphere throughout my dissertation work. Their guidance has been crucial during the time of my PhD training.

Besides my supervisor, I would like to acknowledge with much appreciate to Dr. Qiming Zhang, Dr. Wei Chen and Dr. Amir Shahmoradi for agreeing to serve as committee member and for taking their time to support and guide me.

I would like to express my wholehearted thanks to Professor Alex Weiss. My sincere thanks also go to all my professors and whole staff of Physics Department for their direct or indirect support and assistance since the beginning of the work. Special thanks go to Miss Stacey for keeping us in track of all the deadlines and helping in every manner she could and to Dr. Suman Satyal for such an amazing experience I had as a TA.

All my major simulations were conducted in Texas Advanced Computing Center (TACC). So, I would also like to acknowledge TACC for all the support and computing resources we got for this work. I am grateful that my research was supported partially by the Seed Grant in Particle Therapy from the University of Texas Southwestern Medical Center and the U.S. National Institutes of Health under Grant No. NIH/NCI R15CA199020-01A1.

I would also like to thank all my colleagues, past and present, at UTA. I particularly like to thank Dr. Cong Zhao, Thomas Bates, Youfang Lai, Harsh Arya, Damon Sprouts, Shiwei Zhou, Marcos

Guillen and Eric Amador for their valuable support, discussions and encouragement. I thank all my friends here in UTA Matthew, Yuting, Nil, Lalit and Dr. Michael Greene for making my life comfortable during the first few semesters. I owe special thanks to my friend Suman Shrestha who has been tremendous support throughout my graduate studies. My family in US, Bijay Chalise and family, Santosh Pahari and family and Nisha Thapa and Sanjib Paudel, you have been incredibly supportive for last five years and can't thank you enough for all the love and support you have provided.

I would like to express my special gratitude towards my parents Nava Raj Chalise and Krishna Kumari Chalise, sister Namuna Chalise, brother Ananda Raj Chalise for their unwavering support in all my endeavors. Finally, I must thank my wife for bearing with me and keeping me sane without whom I may have never completed this work.

August 10, 2020

ABSTRACT

INVESTIGATION OF RANGE VERIFICATION IN CARBON ION THERAPY USING MONTE CARLO SIMULATION

Ananta Raj Chalise, Ph.D.

The University of Texas at Arlington, 2020

Carbon ion therapy is one of the advanced forms for radiotherapy and currently only available in few developed countries. Unlike conventional radiation therapy methods, carbon ion therapy has high potential in treating deep-seated and photon-radiation resistant tumors owing to its unique dose-conformality, higher relative biological effect and lower oxygen enhancement ratio. However, due to the lack of precise range verification tools in routine clinic, carbon ion therapy has not been used to its full potentiality. In this work, we used a Monte Carlo simulation tool, Geant4, to investigate range verification for carbon ion therapy. Geant4 is one of the well-stablished Monte Carlo simulation tools for the passage of particles through matter. Using Geant4, we have focused on exploring two of the key avenues in range verification for carbon ion therapy: positron emission tomography (PET) and prompt gamma imaging (PGI). These two methods have been extensively studied as possible solutions to the range uncertainty problem of carbon ion therapy to minimize the treatment margin and to lower the radiation to the organs at risk.

In the first part of this work, we explored the potential of increasing the signals in PET through the use of radioactive carbon (C-11) ions instead of the stable carbon (C-12) ions at different

incident energy levels. Their impact on PGI was also investigated if C-12 ions were replaced by C-11 ions. Prompt gammas (PGs) and annihilation gammas (AGs) were recorded for post-processing to mimic PGI and PET imaging, respectively. We used both time-of-flight (TOF) and energy selections for PGI, which boosted the ratio of PGs to background neutrons to 2.44, up from 0.87 without the selections. The ion inelastic process channel (for ions heavier than He^{2+}) produced more PGs than the other channels, with a sharp drop in PG counts near the Bragg peak. AG yield from C-11 was 6~11 folds higher than from C-12 at low energies (penetration depth of several cm) and 30%~60% higher at high energies (penetration depth of dozens of cm) in PMMA. PG yield from C-11 is comparable to that from C-12 (0.87-fold in the worst scenario). Range verification in this regard can be benefited largely from PET signal boost while maintaining similar PG yield if C-12 ions were replaced by C-11 ions. These results demonstrate that using C-11 ion beams for potentially combined PGI and PET has great potential to improve online range verification accuracy and precision.

In the second part of this work, we focused on the evaluation of the multi-slit camera, which is a mechanical collimation for PGI over a large field of view along the longitudinal beam axis, with the aim to explore the optimal setups of the camera relative to the phantom. Five parameters including slit and slab width, height of collimators and placement of detector as well as collimators were interrogated, which led to thousands of simulations. To facilitate the massive simulation, we first used an isotropic gamma source with an energy spectrum of interest and five evaluation metrics, including signal-to-background ratio, sensitivity, spatial resolution, peak-to-second peak ration, and slab-to-slit ratio to quantify the performance of each configuration. Afterward, a simulation with C-12 ion beam irradiation on a water phantom was used to assess the range

verification performance of the top ranked configuration on each metric. Our preliminary results suggested that signal-to-background ratio and sensitivity outweigh other metrics for capturing the distal fall-off of PG in a uniform phantom. This work lays a strong foundation for future system design of PGI for real-time range verification and monitoring.

Ananta Raj Chalise, PhD

The University of Texas at Arlington, 2020

Table of Contents

Contents

LIST OF FIGURES

CHAPTER 1: INTRODUCTION

The discovery of X-ray in 1895 by William Conrad Roentgen opened a completely new avenue in the field of medicine namely radiology and radiation oncology. Besides diagnostic and research usage of X-ray in medicine, it found its application for cancer treatment just within 7 months of its discovery (Connell and Hellman 2009). Thereafter many groups were involved in the study of effect of radiation in different types of cancers (Connell and Hellman 2009). Hence, the field of radiotherapy began to evolve.

About 2 and half decades later, proton was coined and discovered by Rutherford in 1919. And with the advent of first particle accelerator by Laurence in 1936, the whole new world of particle research was possible. Various properties of ions travelling through the medium were being studied. Wilson was the first to propose the use of proton produced from accelerator for cancer therapy due to its advantageous dose distribution (Wilson 1946). In this seminal paper, he described how the emerging high energy machine can attribute to possibility of charged particles to treat deep seated tumors and gave biophysical rationale of using such ions. In 1954, Lawrence and his team, who were working on the cyclotron, used proton to treat the first human patient. They irradiated the pituitary gland to suppress the pituitary function for a hormone-dependent breast cancer patient (Tsuboi 2020). Proton therapy along with other particle therapy which were primarily limited to lab based research facility got out of lab setup and began deploying in clinical setup such as Loma Linda University Medical Centre in 1990 and the first dedicated clinical heavy ion facility was constructed at National Institute of Radiological Sciences (NIRS) in Chiba, Japan (Minhoara *et al* 2010).

1.1 Ion interaction with matter

1.1.1 Electromagnetic and nuclear process

1.1.1.1 The ions stop in matter

For therapeutic purposes, the range of ions for treating deep-seated tumors will have to be up to 30 cm, which corresponds to 430 MeV/u for Carbon ion (β=v/c ~0.7) and 220 MeV/u for proton and helium ion (β ~0.6) in terms of energy. At these therapeutic energy levels, the ions primarily lose energy to the medium, through which it is traversing, via in-elastic collision with the electrons of the medium, i.e. electronic stopping. The electronic stopping power can be defined as the rate of average loss of energy per unit path length for the given target medium. The electronic stopping power for proton and carbon ions is shown in figure 1.1 (blue and red solid lines). This stopping power can be described by the Bethe-Bloch formula (Bethe 1930, Bloch 1933), whose relativistic version given by Fano (Fano 1963) that includes the shell correction term C/Z_t and density correction term $\frac{\delta}{2}$ as follows:

$$-\frac{dE}{dx} = \frac{4\pi e^4 Z_t Z_p^2}{m_e v^2}\left[\frac{\ln(2m_e v^2)}{< I >} - \ln(1-\beta^2) - \beta^2 - \frac{C}{Z_t} - \frac{\delta}{2}\right] \qquad 1.1$$

where, Z_t represents atomic number of the target atom, Z_p is the electric charge of the projectile, e and m_e are the charge and mass of electrons respectively, v is the velocity of the projectile and <I> is the mean ionization energy of the medium.

Equation 1.1 shows the inverse square dependence between the loss of energy and the velocity of projectile, which means that there is higher loss of energy for lower velocity. For the higher energy case, the electrons of the projectile atoms are fully stripped off and hence in this case Z_p is exactly equal to the atomic number of the atom. This however is not the case for lower energies (below 10 MeV/u). For this case, there is an interplay between ionization and

recombination process. Hence, the mean charge for lower energy cases is lower and hence the equation 1.1 is not valid in its original form. But if were to replace Z_p with Z_{eff} as given by the empirical formula below (equation 1.2), the equation 1.1 will still be valid for lower energy.

$$Z_{eff} = Z_p\left(1 - e^{-125\beta Z_p^{-\frac{2}{3}}}\right) \qquad 1.2$$

The modified equation 1.1 for the case of lower energy (below 10 MeV/u) becomes:

$$-\frac{dE}{dx} = \frac{4\pi e^4 Z_t Z_{eff}^2}{m_e v^2}\left[\frac{\ln(2m_e v^2)}{< I >} - \ln(1-\beta^2) - \beta^2 - \frac{C}{Z_t} - \frac{\delta}{2}\right] \qquad 1.3$$

From equation 1.2, we notice that ion effective charge (Z_{eff}) drops towards the end of the track (range) and hence the electric stopping power also drops sharply due to the square dependence of the Z_{eff} as seen in equation 1.3. Besides, it also turns out that the binding energy of the electron also becomes comparable with the energy that were being lost as result of ion-electrons collision.

Throughout the track of the projectile, the maximum energy transfer only occurs in the Bragg-peak region and the relation for the velocity of the projectile in this region is given in equation 1.4. The projectile velocity given by equation 1.4 is like Thomas-Fermi model's neutral atom's electron. Also, it is worth noticing that the projectile velocity is dependent solely on the charge of the projectile and this value increases with the increase in charge as we can see in figure 1.

$$v_p \approx Z_p^{\frac{2}{3}} v_0 \qquad 1.4$$

where v_0 is Bohr velocity given by $v_0 = e^2 \times 2\pi/h$.

The maximum kinetic energy that can be transferred to a free electron in a single collision by incident particle of mass M is given by the equation 1.5 (Kraan 2015)

$$T_{max} = \frac{2m_e c^2 \beta^2 \gamma^2}{1 + 2\gamma \frac{m_e}{M} + \left(\frac{m_e}{M}\right)^2} \qquad 1.5$$

Towards the very end of the trajectory when the ion energy drops below 10 keV/u, elastic collision between the projectile and target nuclei begins to contribute and becomes a dominant process. This energy-loss mechanism is called as nuclear stopping power. Along with the electronic stopping power, the nuclear stopping power (in dashed lines) of Carbon and hydrogen are also shown in figure 1.1. The value for Hydrogen nuclear stopping is almost negligible compared to others as shown in figure 1.1

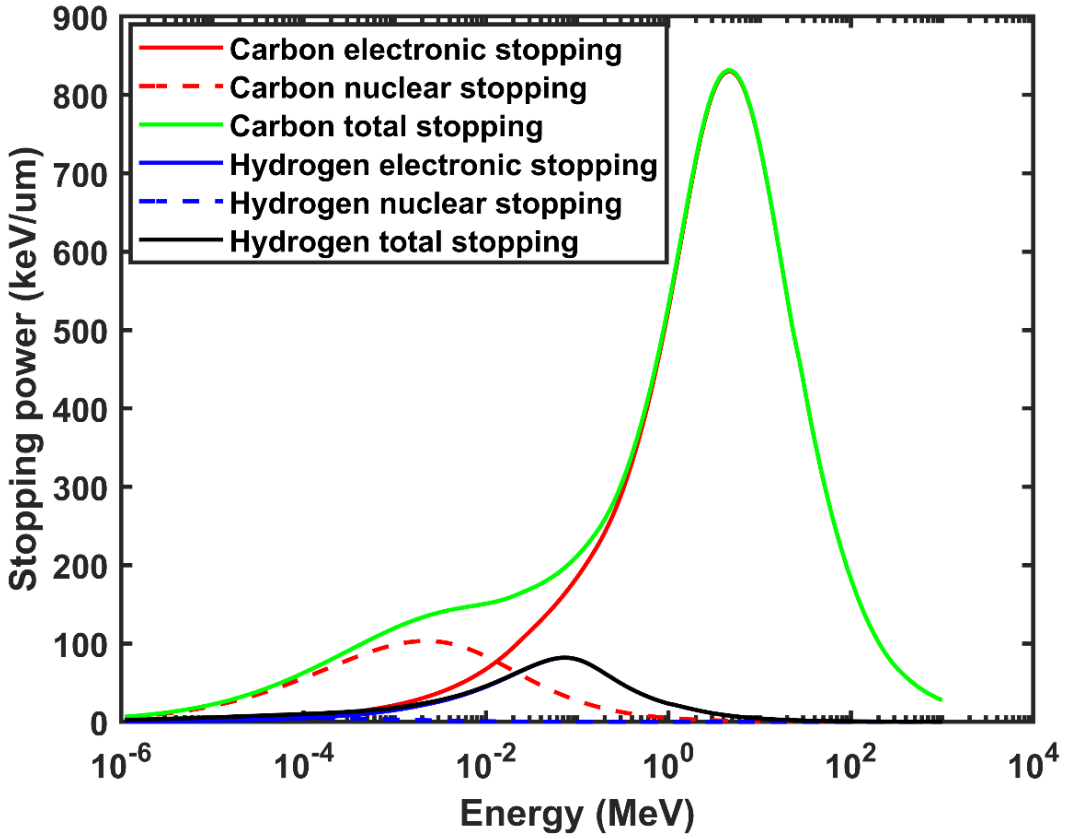

Figure 1.1.: Electronic, nuclear and total stopping power of carbon and hydrogen in PMMA as calculated by SRIM code (Ziegler et al 2010)

Total energy loss which constitutes the combination of both electronic and nuclear stopping power has direct relation with the physics dose. Physical dose of an ionizing radiation is defined as the mean energy deposited in defined tissue mass. Mathematically, we can express the physical dose in the form of equation 1.6

$$D[Gy] = 1.6 \times 10^{-9} \times \frac{dE}{dx} \times F \times \frac{1}{\rho} \qquad 1.6$$

where F is the fluence of particles, ρ is the density of the absorber material and dE/dx is the total energy loss as described earlier. The dose hence calculated in equation is expressed in Gray (Gy) if the units for stopping power is expressed in terms of keV/µm, the fluence is cm^{-2} and density is gm/cm^3.

1.1.1.2 Energy loss straggling or range straggling

In the previous section, we looked into energy losses by ions and we assumed that the energy losses by the decelerating ions were rather a smooth and continuous process. Thus, we took into the consideration of mean energy losses and neglected individual energy loss of ions. However, when we are considering many ions instead of a single ion, cumulative small variations in energy loss of all those individual ions have a key role in shaping the Bragg curve and this phenomenon is known as energy loss straggling or range straggling (Newhauser and Zhang 2015). Without getting too much into mathematics, as we can see from figure 1.2, the range straggling is higher for deeper penetration depth and hence, we see that Bragg-peak is broader for C-11 210 MeV/u than C-11 100 MeV/u. Also, we notice that the height of the dose peak is smaller for the higher energy case (210 MeV/u) than the lower energy case (100 MeV/u), meaning that fewer particles reached to the Bragg-peak region for the higher energy case. In addition, the mass of the ion also plays a significant role in the energy-range straggling. For the comparable range of carbon

and hydrogen ions in water in figure 1.3, we see that the Bragg-peak of proton is wider than that of carbon ion because range straggling is approximately inversely proportional to the square root of particle mass (Schardt *et al* 2010, Testa 2010).

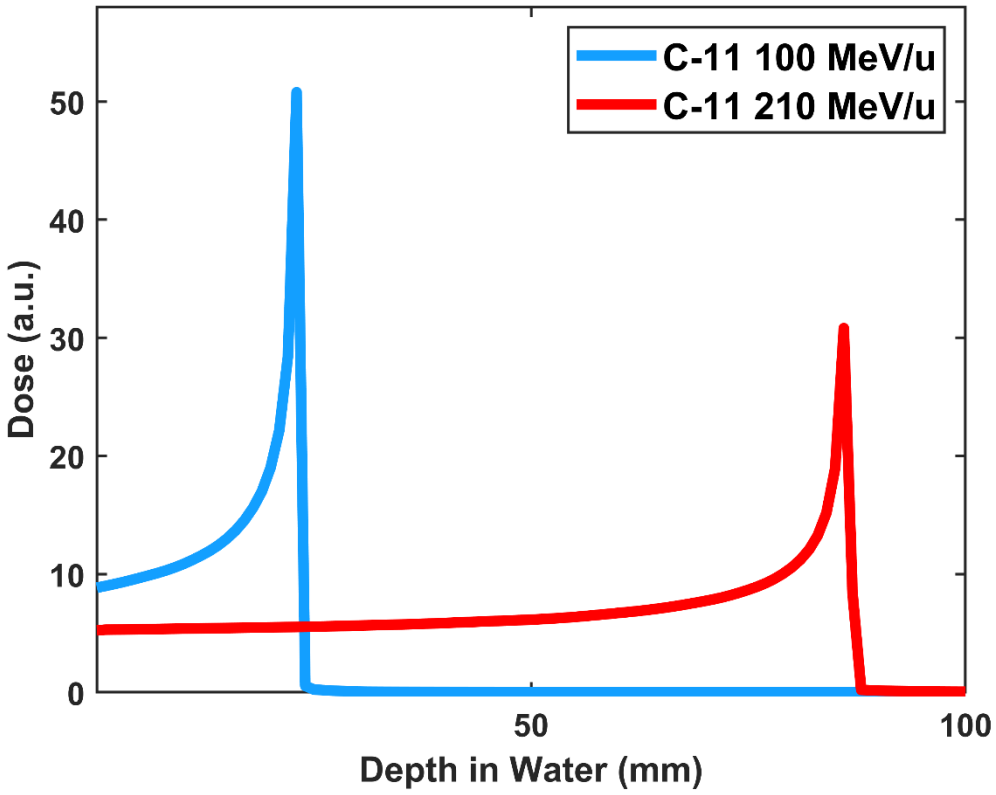

Figure 1.2: Depth dose profile of C-11 100 and 210 MeV/u showing range straggling for different energies of same ion species

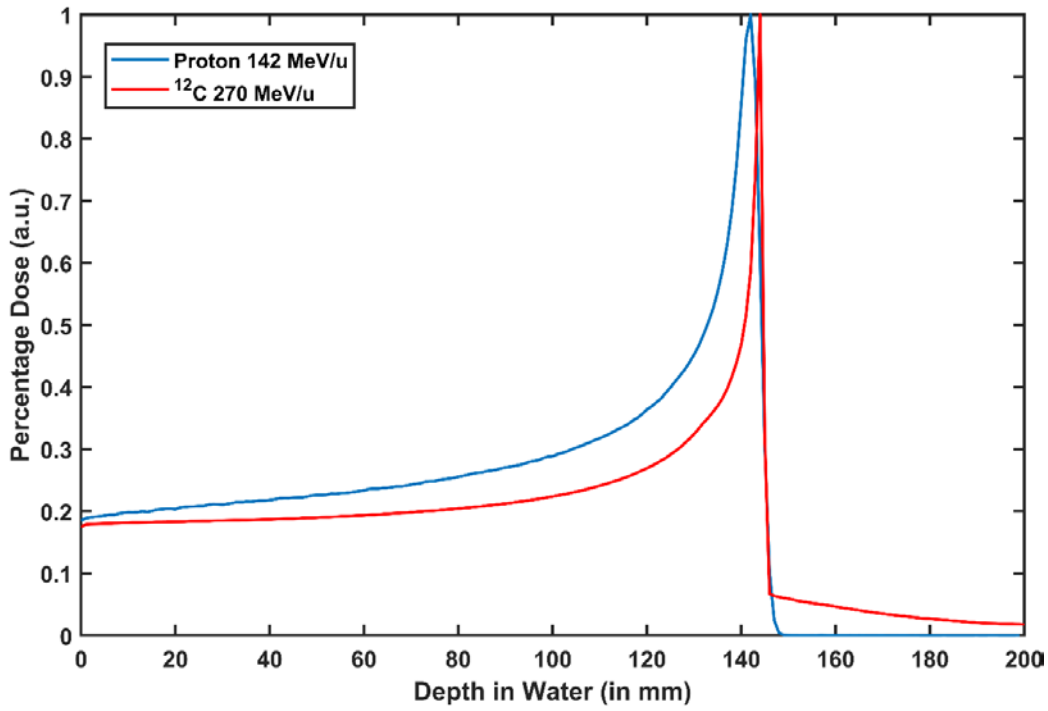

Figure 1.3 Depth dose profile of proton and carbon ion with a comparable range

1.1.1.3. Lateral deflection/ beam spread

We know that the energy loss mechanism is mainly governed by the interaction of the ions with the electrons of the target molecules and that the energy loss due to nuclear stopping power is relatively low. Nuclear interaction, however, plays a vital role in broadening the beam in the lateral direction. This lateral broadening is due to the elastic Coulomb interaction of the ion beam with the target nuclei. The scattering angle Θ at a penetration depth d, due to the aggregate of smaller deviations of multiple ions from the initial beam direction, can be approximated by a Gaussian function with standard deviation as proposed by Highland (1975),

$$\sigma_\theta = \frac{14.1}{\beta\, p\, c} Z_p \sqrt{\frac{d}{L_{rad}}}\left[1 + \frac{1}{9}\log_{10}\left(\frac{d}{L_{rad}}\right)\right] \qquad 1.7$$

where L_{rad} is the radiation length of the medium, β is velocity relative to speed of light (v/c), p is momentum and c is the speed of light.

Because of the term $\beta\ p\ c$ in the denominator in the equation 1.7, we see that the lateral spread is more pronounced when the particle energy decreases. As we see in figure 1.4 for the case of hydrogen and carbon, carbon ions have very little scattering compared to hydrogen ions. This property has been one of the reasons for preferring heavier ions rather than lighter ones for therapeutic purposes and can be particularly useful if there are organs at risk (OAR) in the vicinity of the treatment site. Less lateral spreading helps to protect the OAR.

1.1.1.4 Nuclear collisions of hadrons at different energies

Besides the electromagnetic interaction, the charged particles also undergo nuclear interaction with the target nuclei. Compared to the electromagnetic interaction, the nuclear interaction leads to significantly less energy loss, but has higher significance with regards to range verification. Unlike the electromagnetic interaction, there is no universal model that can accurately describe the nuclear interaction.

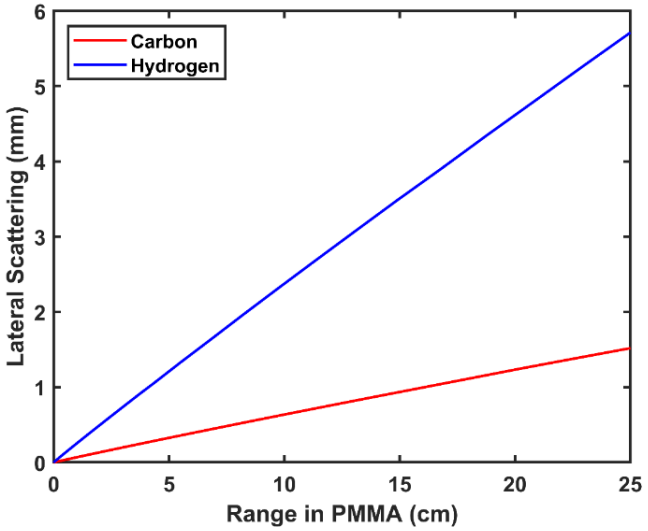

Figure 1.4 Lateral scattering vs range in PMMA for Carbon and Hydrogen ions with different energies calculated by SRIM code (Ziegler et al 2010)

For lighter ions like proton, due to the nuclear interaction there will be fission of target nuclei, whereas for the case of heavier ions, there is fission not only in the target, but also in the projectile nuclei. Based on the locations, these interactions can be classified as central collision, peripheral collision or Coulomb force induced process. The most frequent one is the peripheral collision, where the projectile particle loses one or several nucleons. This in fact can be described by the abrasion-ablation model, which results in fragmentation of projectiles as well as the target nuclei as shown in figure 1.5. Central collision though rare than peripheral collision results into large transfer of energy, thereby causing the projectile to break into smaller pieces.

Fragmentation of the projectile depends on ion type, its energy, and the medium through which it is traversing. In the case of ^{12}C 200 MeV/u beam in water it has been found that only 70% of the projectile make all the way to the Bragg peak intact and the rest undergoes the nuclear interaction. Whereas for the case of 300 MeV/u, the percent of carbon ions reaching the Bragg peak intact drops drastically to 30 % from 70 % (Park and Kang 2011).

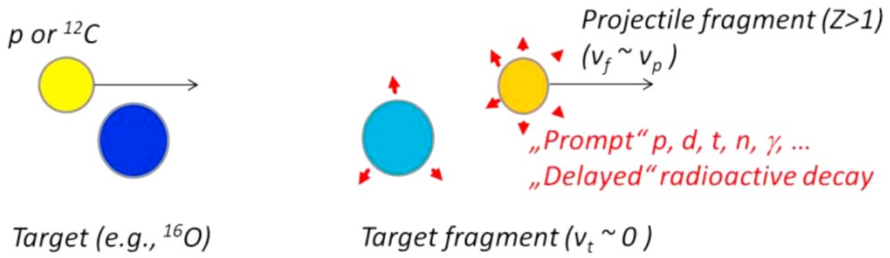

Figure 1.5 : Illustration of nuclear fragmentation interaction (Parodi 2016)

1.1.1.5 Emission of prompt gamma

As indicated in previous sub-section, the most common nuclear interaction is peripheral collision and can be explained by the abrasion-ablation model. In this model, the overlapping nucleons of the projectile and target nuclei abrades, thereby creating a fireball. Other nucleons, however, are impacted very insignificantly. In the ablation process, the unaffected nucleons from the projectile as well target nuclei and fireball undergo de-excitation processes via nucleon evaporation and light clusters (Battistoni *et al* 2016). During this de-excitation process of excited nuclei to the ground state, gamma is emitted. Since this process takes place instantaneously, these gammas are termed as prompt gamma. Prompt gamma has the potential of online Bragg-peak tracking, i.e. real time when the treatment is conducted (Zarifi *et al* 2019).

1.1.1.6 Emission of annihilation gamma

As we discussed in previous section, the nuclear interaction has a significant toll on the primary particle. Due to these nuclear interaction, lighter fragments of different masses are created. Of different fragments, one interesting group of nuclei are also generated, namely positron emitting nuclei (PEN). These nuclei do travel almost at the similar velocity of the projectile beam and stop at the similar location as the main beam. PENs are unstable isotopes and undergo β^+ decay i.e. $A(Z,N) \rightarrow A(Z-1, N+1) + e^+ + \gamma_e$ (Pshenichnov *et al* 2006). These positrons then annihilate with

the electrons ($e^+e^- \rightarrow \gamma\gamma$) in the medium and create two pairs of annihilation gamma of 511 keV, which can be utilized to determine the treatment beam range.

1.2 Carbon ion therapy

1.2.1 Origins of hadrontherapy

If we are to treat deep seated tumors, care must be taken such that the healthy tissues around the tumor receive a minimal amount of radiation dose. As previously mentioned, since Wilson's paper in 1946, the advantage of charged particles for localized dose was known. Lawrence Berkley Laboratory (then LBL but currently LBNL) at the University of California then performed pioneering work on particle therapy and began treating cancer patients with protons and helium in 1954 and 1957, respectively (Mohamad *et al* 2017). By the time this center was closed in 1992, it performed treatment of 433 patients with ^{20}Ne ions and was the only heavy ion radiotherapy center in the world (Schardt *et al* 2010). After its closure, Heavy Ion Medical Accelerator (HIMAC) in Japan started to treat patients with carbon ions in 1994. Afterwards, Paul-Scherrer-Institute (PSI) in Switzerland along with Gesellschaft fur Schwerionenforschung (GSI) in Germany were also built for heavy ion therapy. Fast forward to present, as of July 2020, there are 12 carbon ion treatment facilities and 92 proton facilities in operation worldwide (PTCOG 2020).

1.2.2 Advantage of carbon ion therapy compared to other radiotherapy

1.2.2.1 Physical aspect

Conventional radiotherapy like photon and fast neutrons therapy has an exponential absorption of dose as we can see for the case of 25 MV photon in figure 6. But in the case of carbon

ion beams and other ion beams, we see that the energy deposition increases with depth and has a very sharp maximum towards the end of its range as shown in figure 1.6. This sharp peak region is known as Bragg peak named after Bragg who performed pioneering work on alpha particles. As can be seen from figure 1.6, the higher the energy of the ion, the deeper is the penetration in the medium. i.e. the range is longer.

As discussed in previous sections, the type of the incident ions and range straggling affect the shape of Bragg peak, e.g. in figure 1.3 the Bragg peak of carbon ions is sharper than that of proton. Also, the dose fall-off in the lateral region for carbon is more rapid than for proton due to less lateral spread. However, it is worth mentioning that at the end of peak, we see the dose of carbon does not come to a stop as rapid as proton. This is due to the lower atomic fragments of carbon ions, whose biological effect is nominal (Tsujii and Kamada 2012).

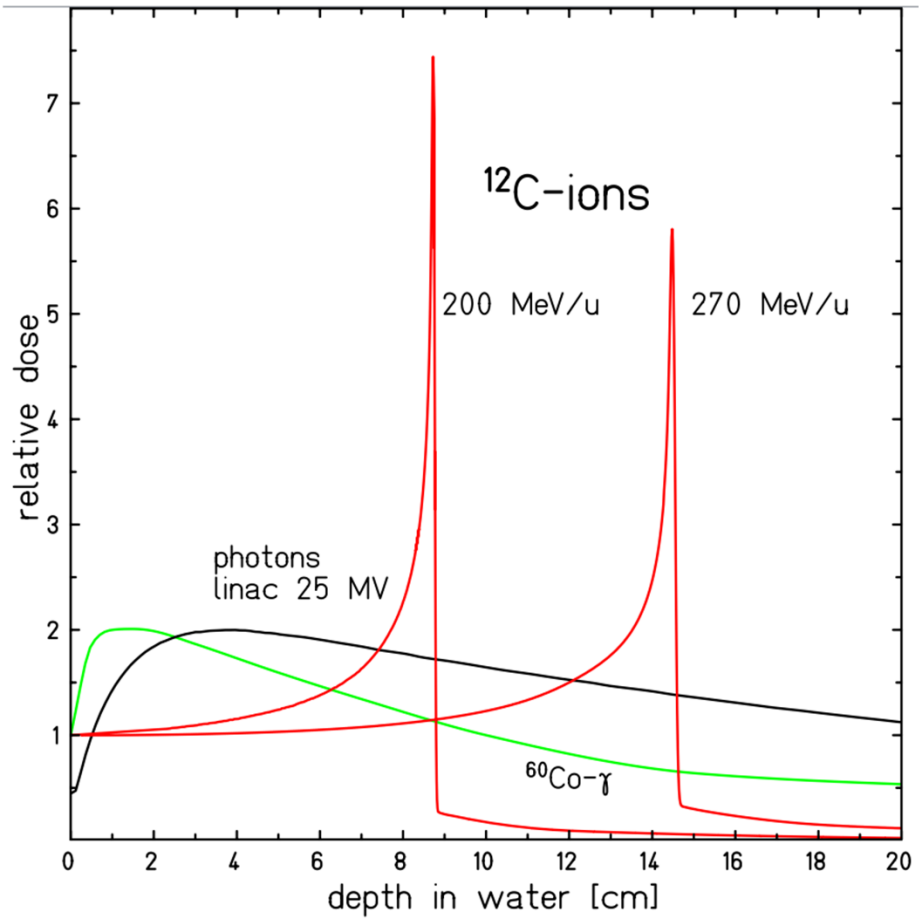

Figure 1.6 Dose profile oi photons from different source and carbon ions of different energy in water (Schardt *et al* 2010)

1.2.2 Radiobiological effect

Before delving into the biological aspect of the advantage of carbon ion therapy, we define several key terms in radiotherapy. The first term is linear energy transfer (LET), which is loss of energy by the particle per unit path length (DANZKER *et al* 1959). Different radiations have different LET. Low LETs are those which ionize sparsely and includes photons, protons and electrons. And densely ionizing radiations are termed as high-LET and includes carbon and fast neutrons. Higher LET radiations kill cells more efficiently than low LET radiations (Hendry 2005).

Relative biological effectiveness (RBE) is defined as the ratio of doses of two radiation beams such that they achieve the same biological endpoint (for instance, cell survival) under the same condition (Mohamad *et al* 2018). For RBE, 250kVp photons are usually used as a reference radiation. Thus, RBE implicates that an individual who received 1 rad dose from α particle will suffer more damage to tissues that that who received 1 rad dose from 250 kVp photon radiation (Marion 1974). Finally, the term of oxygen enhancement ratio (OER) is defined as the ratio of dose achieving the same biological endpoint between hypoxic and normoxic conditions. This helps to distinguish for the fact that for the same radiation of the same dose, its effect differs greatly due to the presence or absence of oxygen in the tumor during the treatment. For instance, in the case of clinically relevant megavoltage photons, the OER can differ as much as by 2.5 to 3.5 (Chang *et al* 2014). So, LET, RBE and OER are key factors in determining the efficacy of radiation. RBE and OER for X-ray, proton and carbon ions are shown in figure 1.7.

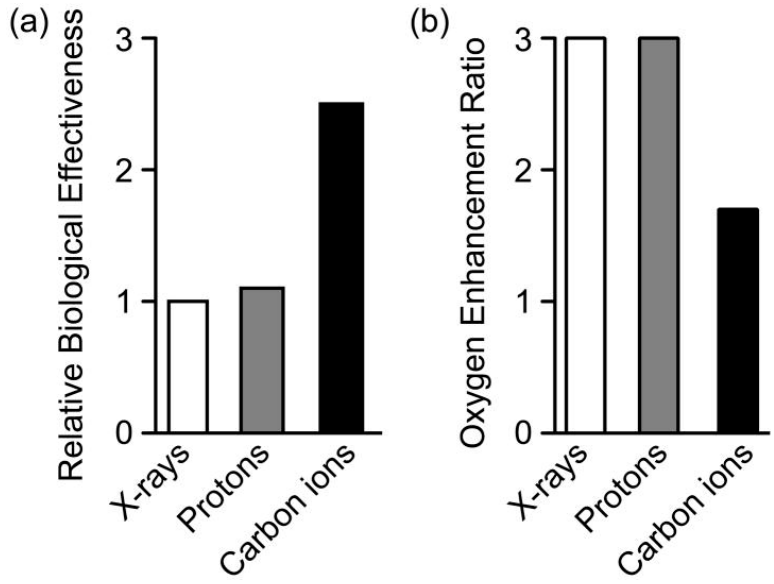

Figure 1.7 : Comparison of X-ray, proton and carbon ions in terms of their RBE and OER (Allen et al 2011)

In particle therapy, ions with higher RBE and lower OER are preferred for treatment beams. Until LET reaches 100 keV/μm, RBE generally increases with increased LET. However, for OER, RBE decreases with increasing LET. Though higher LET ions have mostly optimum OER (nearly 1), higher LET can also cause excessive damage to normal tissues. In this regard, carbon ions have a good combination of RBE and OER as depicted in figure 1.7, and are considered as one of the best choices in particle therapy (Mohamad *et al* 2018).

1.2.3 Carbon ion therapy delivery system

1.2.3.1 Types of accelerators

There are broadly two kinds of accelerators, namely Cyclotron and Synchrotron, used in particle therapy to accelerate treatment particles to the desired energy level. In the cyclotron accelerator, particles are injected at the center of the accelerator and follow a spiral path to it extraction point at the extremity. The illustration of a cyclotron is shown in figure 1.8, which consists of a large circular magnet such that it offers constant magnetic field between the pole-faces. As long as the particle is inside the “dee” (D) of the cyclotron, it is not under the influence of the electric field and hence move along a circular path. However, there is a potential difference between the two Ds. Every time the particles passes from one D to the opposite D, the accelerating voltage increases the particle energy and the radius of the particle orbit becomes larger. This acceleration process repeats until the particles reach the designed energy and are extracted from the extraction point at the extremity.

Currently, all clinical carbon ion therapy facilities in operation are based on synchrotron (PTCOG 2020). Synchrotrons are circular machines where particles are forced to circulate around a closed orbit as shown in Figure 1.8. For synchrotron acceleration, ions already accelerated up to few megaelectron volts are injected into the ring. They then pass through the radio frequency cavity

to accelerate to the desired energy and velocity. Unlike cyclotron, the magnetic field of synchrotron must be varied such that the particles remain in the track. In this regard, synchrotron is more complicated than cyclotron. The schematic for the synchrotron made by HITACHI is shown in figure 1.8 (Moore. *et al* 2015).

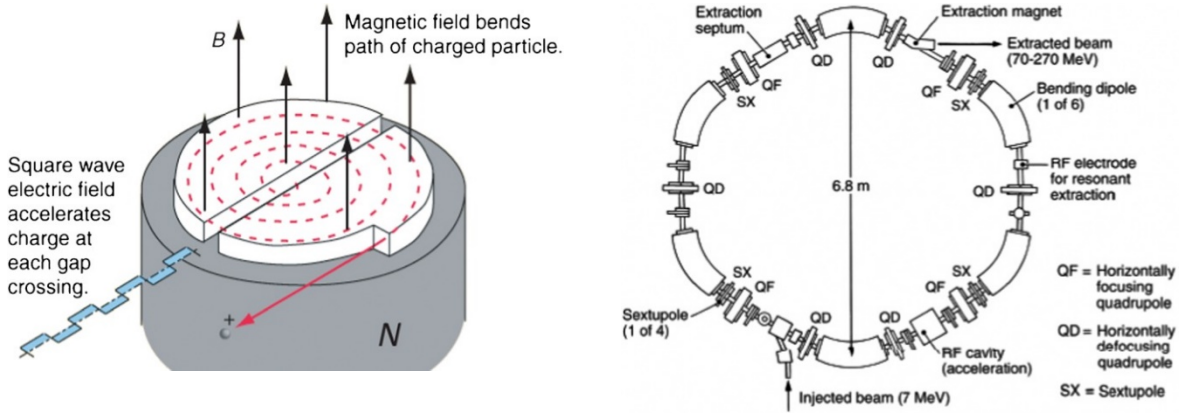

Figure 1.8 Illustration of a cyclotron (left) and a synchrotron (right) (Moore. et al 2015)

Both accelerators have their own pros and cons. Cyclotrons are highly reliable easier to operate compact machines. Although they can deliver extremely stable beam, lack of energy variations becomes a major drawback. Synchrotrons offer the flexibility of energy variation, at the expense of requiring a particle injector and more complex machines to operate.

1.2.3.2 Beam delivery system

The ion beam that comes out of the accelerator is pencil-like and has to be delivered to the cancer site, which is usually much larger than the beam size. Therefore, a beam delivery system is needed to enable this small-size beam to treat a large target region. The overview for three-dimensional methods for beam delivery is tabulated in Table 1.1. The two major types of systems are passive and active beam shaping. The schematics for passive and active beam delivery systems are shown in figure 1.9 (Jakel 2006, Karger *et al* 2010).

Table 1.1: Overview of three-dimensional beam delivery methods (Minohara et al 2010)

	Lateral outline of target				Target thickness	Distal target depth	
	Laterally spread out of pencil beam		Fine shaping of radiation field		Spread out of Bragg peak (SOBP)	Adjust the maximum depth	Fine adjust to the target end
Passive beam shaping	Wobbler magnets + scatterer	•	Patient-specific collimator	•	Ridge filter	Range shifter with fixed beam energy	Patient-specific compensator
	Double scatterer		Multi-leaf collimator (static)		Range modulator		
Layer stacking method	Wobbler magnets + scatterer		Multi-leaf collimator (dynamic)		Scanning mini-SOBP by range shifter at fixed beam energy		Patient-specific compensator
Active beam shaping	Spot scanning			•	Range shifter with fixed beam energy		
	Raster scanning				Variable beam energy		

1.2.3.2.1 Passive beam shaping

Passive beam shaping, as the first beam delivery method, is widely used in proton therapy as well as heavy ion therapy. With the help of a variable degrader, which may be a varying thickness rotating wheel or a wedge-shaped wobbling plate, different depths are achieved for spread out Bragg peak (SOBP) as shown in Figure 1.9a. On top of it, patient specific collimators are designed to adjust the lateral dose distribution and the range compensator helps to adjust the distal edge of the tumor. Therefore, a whole tumor can be treated by a mono-energetic beam at once.

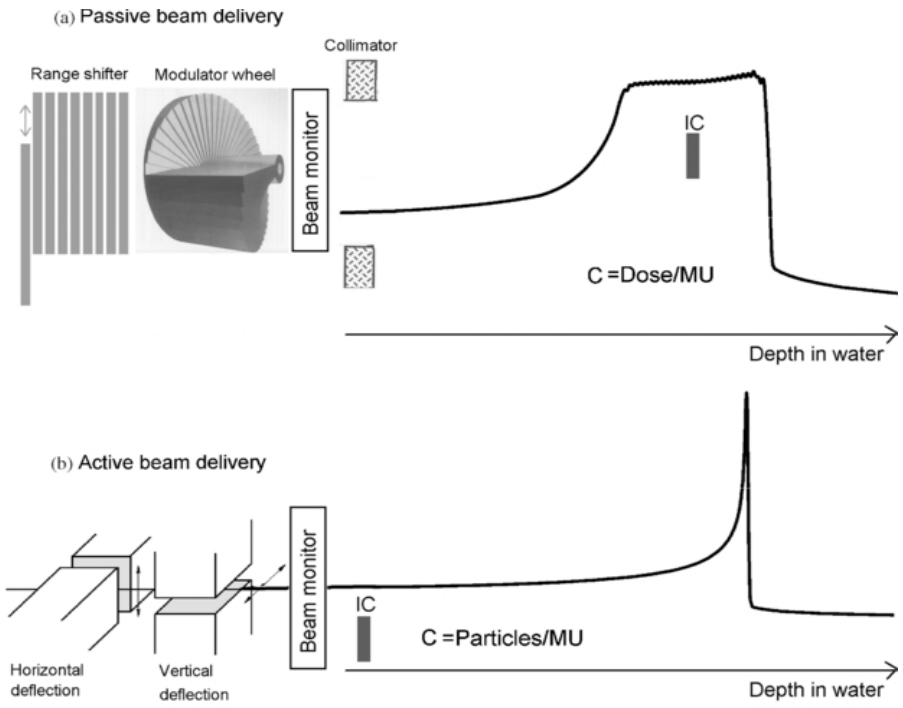

Figure 1.9 Passive (a) and active (b) beam delivery systems (Karger et al 2010)

1.2.3.2.2 Active beam delivery system

This type of beam delivery system is also called the pencil beam scanning method and takes advantage of the charge of ions being used to treat the patient. The target volume is literally painted with the pencil beam with the help of the varying electric field in horizontal and vertical directions as shown in Figure 1.9b. In this beam delivery method, the target volume is converted into several thin longitudinal layers and irradiated layer by layer.

1.3 Challenges in carbon ion therapy range uncertainties

1.3.1 Range uncertainties

We have outlined the advantages of carbon ion therapy in previous sections. One of the key advantages of using particle therapy in general is the sharp dose peak of ions, which can be put to the best use for treating tumors adjacent to critical organs at risk (OAR). However, if there

is any misalignment or miscalculation during the treatment that causes range uncertainties, a high radiation dose would be imparted to the OAR. In this regard, particle therapy is considered a double-edged sword. Due to this fact, a considerable amount of safety margin has to be in place, and hence particle therapy has not been able to produce its maximum benefit owing to range uncertainties. These uncertainties stem from various sources, including measurement uncertainty in water for commissioning, compensator design, beam reproducibility, patient setup, CT imaging and calibration, CT conversion to tissue and range degradation (Paganetti 2012).

1.2.4 Possible solutions

Unlike photons in phototherapy, carbon ions in particle therapy usually do not escape the patient body during the treatment. Since carbon ions stop in the body, the difference of the ion beam intensity before and after entering the body is not available to verify the dose distribution and range. Secondary radiations emitted during the beam irradiation process have been found to co-related with the beam range, and hence can be utilized for the range verification purposes. Annihilation gamma and prompt gamma have been extensively studied and are finding places in clinics to verify the range after or during the treatment. The imaging methods utilizing these two types of gammas are explained in the following subsections.

1.2.4.1 Positron emission tomography (PET)

The primary usage of PET in hadrontherapy was for verifying the stopping position of low-dose radioactive ion beam before the usage of regular-dose stable ion beam (Parodi 2016). Later it was found that positron emitting nuclei (PEN) were generated as a result of nuclear fragmentation reaction of the projectile of the therapeutic beam and the tissues of the patient body (Tobias *et al* 1977), which can be imaged by PET. In the case of heavier ions, distinct peaks were found in the proximity to the Bragg peak indicating that PEN were generated near the Bragg peak.

This correlation is the basis for using PET for the range verification purpose. One integrated PET for proton therapy is shown in figure 1.10

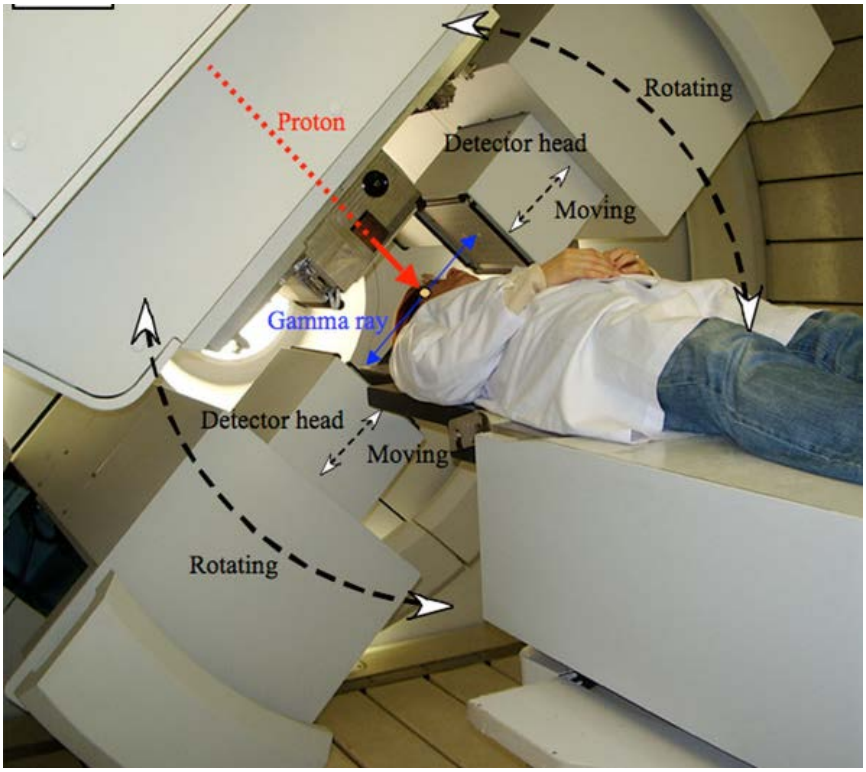

Figure 1.10: PET used in clinic integrated with proton delivery gantry for imaging right after the treatment (Parodi and Polf 2018)

1.2.4.2 Prompt gamma imaging (PGI)

During the deexcitation of nuclei due to imparting the carbon ions on the body tissue's nuclei, gamma photon radiations are promptly emitted. Though these prompt gammas were considered as interference for PET in the early days, Stichelbaut and Jongen later found that their peaks and fall-offs are also correlated with the position of the Bragg-peak (Parodi 2016). Experimental verification of PGI followed shortly after this discovery. Now PGI has been deemed as one of the most suitable modalities for on-line range verification because of the short time scale within which these prompt gammas are generated.

1.4 Geant4 simulation

Different simulation packages were instrumental in earlier studies for PET and PGI. Especially for PGI, a proof of concept was first conducted with the help of simulation, and then the experimental verification followed subsequently. Various packages are available in the field of which we decided to use Geant4 because of its growing usage, versatility, powerful as well as being an open source package with great support from the developers.

Geant4 is an object-oriented C++ programming language based open source toolkit built by international collaborators for simulating the passage of particles through matter (Agostinelli *et al* 2003). Originally designed with application in high energy physics (HEP), this toolkit has now found its application beyond HEP and is routinely used in space physics and medical physics. As it is a general toolkit, a special application must be developed using domain knowledges from the user, who provides all the necessary information to run the application. There are, however, many examples provided, which can be adapted to the particular user applications. The software is designed with flexibility in mind and hence accepts various inputs from the user. Because of this flexibility, the software requires a certain level of programming for the configuration in its source files as well as header files. In this regard, Geant4 requires knowledge of the C++ programming language and hence may not be so much user friendly as the dedicated simulation package, such as GATE.

Upon initialization of the main program, the G4RunManager routine with the help of DetectorConstruction and Physicslist constructs the geometry and the materials of the experiment setting and the detector. It also declares the particles that act as the primary or the secondary, and the processes that handle these particles and the production cuts. A typical working logic of Geant4 is depicted in the flowchart in figure 1.11. In any Geant4 simulation, the user must define the

geometry of their experimental setup, followed by the primary particles used for the simulation and the physics that will govern the simulation. Visualization and analysis of the data in terms of tuples and histogram are however optional for a Geant4 simulation and dependent on the user preference.

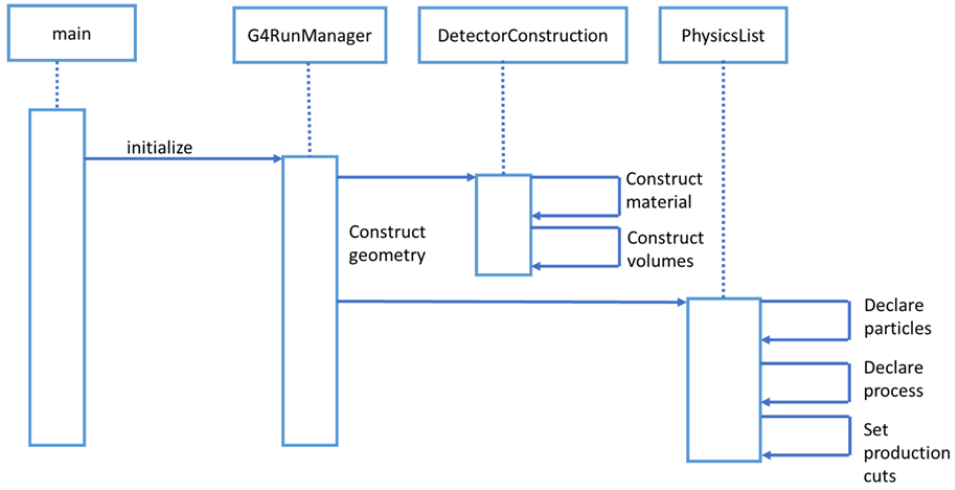

Figure 1.11: The workflow of Geant4 simulation (web)

Geant4 keeps tracks stack of all the events and processes them in order as shown in figure 1.12. From this stack, each particle is picked and moved till it either exits the simulation world or reaches energy below the tracking level. At the end, the simulation keeps the record of the information that a user intends to collect.

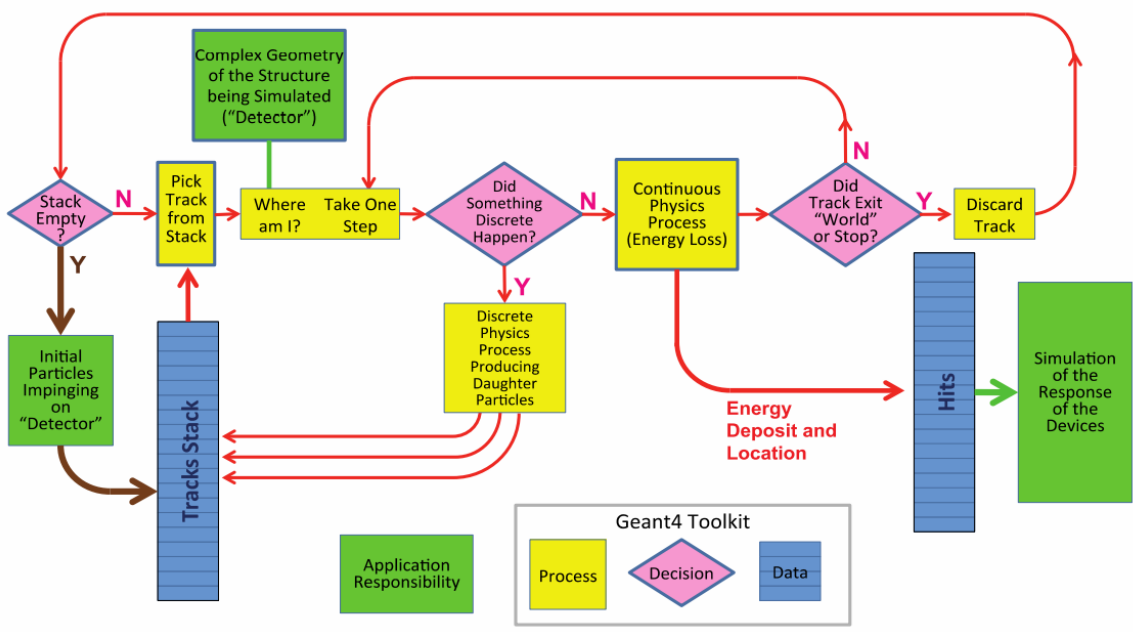

Figure 1.12: Event and track loop in Geant4 (Anon 2012)

One of the important key user inputs for any simulation is the physics processes. Geant4 has collections of various physics models (sometimes alternative models as well) to govern the physics of various particles and photons ranging from 250 eV up to several PeV. There are 7 major physics processes which define how particles interact with the materials. These processes are: electromagnetic, hadronic, decay, photolepton-hadron, optical, parametrization and transportation. Besides these processes, users also have the option to choose from various cross-sectional data. So, the physics list can be tailored to specific need by the user. Lately, Geant4 has started to provide with the reference list, which includes the necessary processes and cross-sections, so that the user does not have to get into the details of defining them for the individual particles. For the simulations related to carbon ion therapy in this work, the reference physics list, namely QGSP_BIC_HP, is recommended (Zarifi *et al* 2019).

In the QGSP_BIC_HP reference physics list, the inelastic hadron-nucleus processes are implemented by the Quark Gluon String, pre-compound (QGSP) and binary cascade model.

Binary cascade takes care of π^+, π^-, K^+, K^-, K_L, K_S, Λ, Σ^+, Σ^-, Σ^0, Ξ^-, Ξ^0 and Ω^- interactions from 0 to 12 GeV and QGSP takes care of protons, neutrons, pions and kaons above 12 GeV. Kaons and pions whose energy are below 91 GeV are governed by G4PiNuclearCrossSection for π^+ and π^-, G4ChipsKaonPlusInelasticXS for K^+, G4ChipsKaonMinusInelasticXS for K^- and G4ChipsKaonZeroInelasticXS for K^0. However, for energies higher than 91 GeV, the Barashenkov-Glauber cross sections are used. The G4HadronElastic model is used for all hadrons in the case of elastic interaction except for protons and neutron where G4ChipsElasticModel is used between 0 to 100 TeV. The Gheisha elastic cross section are employed at all energies for deuterium, tritium and alpha whereas the Glauber-Gribov elastic cross sections are used for all energies of ^{3}He (Geant4 Collaboration 2017).

From the available physics list, QGSP_BIC_HP has been found to be better with regards to gamma yield and energy profile. So, for both of our studies this reference physics list was used. We adapted the Hadrontherapy example (Cirrone *et al* 2009) included in the Geant4 advanced examples to achieve our simulation goals in this work.

1.5 Thesis composition

This thesis describes our detailed study of the range verification in carbon ion therapy using Monte Carlo simulation. It has two main parts. In Chapter 2, we studied beam range verification of carbon-11 and carbon-12 using prompt gamma and annihilation gamma measurements. This part of the thesis has been submitted in Biomedical Physics & Engineering Express (Chalise et al. 2020). In Chapter 3, we studied various configuration of multi-slit collimators for prompt gamma imaging. We plan to submit this part of the thesis to The Physics in Medicine and Biology Journal (Chalise et al. 2020, in preparation). In Chapter 4, we present a summary of our work as well as

future work. Finally, in Appendices, we gave two examples to run simulations described in Chapters 2 and 3.

REFERENCES

Agostinelli S, Allison J, Amako K, Apostolakis J, Araujo H, Arce P, Asai M, Axen D, Banerjee S, Barrand G, Behner F, Bellagamba L, Boudreau J, Broglia L, Brunengo A, Burkhardt H, Chauvie S, Chuma J, Chytracek R, Cooperman G, Cosmo G, Degtyarenko P, Dell'Acqua A, Depaola G, Dietrich D, Enami R, Feliciello A, Ferguson C, Fesefeldt H, Folger G, Foppiano F, Forti A, Garelli S, Giani S, Giannitrapani R, Gibin D, Gómez Cadenas J J J, González I, Gracia Abril G, Greeniaus G, Greiner W, Grichine V, Grossheim A, Guatelli S, Gumplinger P, Hamatsu R, Hashimoto K, Hasui H, Heikkinen A, Howard A, Ivanchenko V, Johnson A, Jones F W W, Kallenbach J, Kanaya N, Kawabata M, Kawabata Y, Kawaguti M, Kelner S, Kent P, Kimura A, Kodama T, Kokoulin R, Kossov M, Kurashige H, Lamanna E, Lampén T, Lara V, Lefebure V, Lei F, Liendl M, Lockman W, Longo F, Magni S, Maire M, Medernach E, Minamimoto K, Mora de Freitas P, Morita Y, Murakami K, Nagamatu M, Nartallo R, Nieminen P, Nishimura T, Ohtsubo K, Okamura M, O'Neale S, Oohata Y, Paech K, Perl J, Pfeiffer A, Pia M G G, Ranjard F, Rybin A, Sadilov S, Di Salvo E, Santin G, Sasaki T, et al 2003 Geant4—a simulation toolkit *Nucl. Instruments Methods Phys. Res. A* **506** 250–303

Allen C, Borak T B, Tsujii H and Nickoloff J A 2011 Heavy charged particle radiobiology: Using enhanced biological effectiveness and improved beam focusing to advance cancer therapy *Mutat. Res. - Fundam. Mol. Mech. Mutagen.* **711** 150–7

Anon 2012 *Transforming Geant4 for the Future Report from the Workshop on Transforming*

Geant4 for the Future

Augusto R S, Mendonca T M, Wenander F, Penescu L, Orecchia R, Parodi K, Ferrari A and Stora T 2016 New developments of 11C post-accelerated beams for hadron therapy and imaging *Nucl. Instruments Methods Phys. Res. B* **376** 374–8

Battistoni G, Mattei I and Muraro S 2016 Nuclear physics and particle therapy **1** 661–86

Bauer J, Unholtz D, Sommerer F, Kurz C, Haberer T, Herfarth K, Welzel T, Combs S E, Debus J and Parodi K 2013 Implementation and initial clinical experience of offline PET/CT-based verification of scanned carbon ion treatment *Radiother. Oncol.* **107** 218–26

Bethe H 1930 Zur Theorie des Durchgangs schneller Korpuskularstrahlen durch Materie *Ann. Phys.* **397** 325–400

Bloch F 1933 Bremsvermögen von Atomen mit mehreren Elektronen *Zeitschrift für Phys.* **81** 363–76

Bom V, Joulaeizadeh L and Beekman F 2012 Real-time prompt gamma monitoring in spot-scanning proton therapy using imaging through a knife-edge-shaped slit *Phys. Med. Biol.* **57** 297–308

Chang D S, Lasley F D, Das I J, Mendonca M S, Dynlacht J R, Chang D S, Lasley F D, Das I J, Mendonca M S and Dynlacht J R 2014 Oxygen Effect, Relative Biological Effectiveness and Linear Energy Transfer *Basic Radiotherapy Physics and Biology* (Springer International Publishing) pp 235–40

Chatterjee A, Alpen E L, Tobias C A, Llacer J and Alonso J 1981 HIGH ENERGY BEAMS OF RADIOACTIVE NUCLEI AND THEIR BIOMEDICAL APPLICATIONS *Int. J. Radiat. Oncol. Biol. Phys.* **7** 503–7

Chi Y, Tian Z and Jia X 2016 Modeling parameterized geometry in GPU-based Monte Carlo

particle transport simulation for radiotherapy *Phys. Med. Biol.* **61** 5851–67

Chuong M, Badiyan S N, Yam M, Li Z, Langen K, Regine W, Morris C, Snider J, Mehta M, Huh S, Rutenberg M, Nichols R C and Nichols R C 2018 Pencil beam scanning versus passively scattered proton therapy for unresectable pancreatic cancer. *J. Gastrointest. Oncol.* **9** 687–93

Cirrone G A P, Cuttone G, Di Rosa F, Mazzaglia S E, Romano F, Attili A, Bourhaleb F, Russo G, Kataniemi P, Heikkinen A, Marchetto F and Jungwook S 2009 Hadrontherapy: An open source, Geant4-based application for proton-ion therapy studies *IEEE Nuclear Science Symposium Conference Record* pp 4186–9

Connell P P and Hellman S 2009 Advances in radiotherapy and implications for the next century: A historical perspective *Cancer Res.* **69** 383–92

DANZKER M, KESSARIS N D and LAUGHLIN J S 1959 Absorbed dose and linear energy transfer in radiation experiments. *Radiology* **72** 51–61

Dudouet J, Cussol D, Durand D and Labalme M 2013 Benchmarking GEANT4 nuclear models for carbon-therapy at 95 MeV / A *Benchmarking*

Ebner D K and Kamada T 2016 The Emerging Role of Carbon-Ion Radiotherapy. *Front. Oncol.* **6** 140

Enghardt W, Debus J, Haberer T, Hasch B G, Hinz R, Jgkel O, Krgmer M, Lauckner K, Pawelke J and Phnisch F 1999 *Positron emission tomography for quality assurance of cancer therapy with light ion beams* vol 654

Fano U 1963 Penetration of Protons, Alpha Particles, and Mesons *Annu. Rev. Nucl. Sci.* **13** 1–66

Ferrero V, Fiorina E, Morrocchi M, Pennazio F, Baroni G, Battistoni G, Belcari N, Ciocca M, Del Guerra A, Donetti M, Giordanengo S, Giraudo G, Patera V, Peroni C, Rivetti A, Dionisio da Rocha Rolo M, Rossi S, Rosso V, Sportelli G, Tampellini S, Valvo F, Wheadon R, Cerello

P, Giuseppina Bisogni M, di Roma S, Veronica Ferrero I, Camarlinghi N N, Ciocca M, Del Guerra A, Donetti M, Giordanengo S, Giraudo G, Patera V, Peroni C, Rivetti A, Rolo M D da R, Rossi S, Rosso V, Sportelli G, Tampellini S, Valvo F, Wheadon R, Cerello P and Bisogni M G 2018 Online proton therapy monitoring: clinical test of a Silicon-photodetector-based in-beam PET *Sci. Rep.* **8** 4100

Le Foulher F, Bajard M, Chevallier M, Dauvergne D, Freud N, Henriquet P, Karkar S, Letang J M, Lestand L, Plescak R, Ray C, Schardt D, Testa E and Testa M 2010 Monte Carlo Simulations of Prompt-Gamma *IEEE Trans. Nucl. Sci.* **57** 2768–72

Geant4 Collaboration 2017 *Guide for physics list*

Hendry J H 2005 Protective Effects on Microorganisms in Radiation Sterilised Tissues *Sterilisation of Tissues Using Ionising Radiations* (Elsevier Inc.) pp 331–8

Highland V L 1975 Some practical remarks on multiple scattering *Nucl. Instruments Methods* **129** 497–9

Jakel O 2006 Heavy Ion Radiotherapy *New Technologies in Radiation Oncology* pp 365–77

Jongen Y and Stichelbaut F 2003 39th PTCOG meeting San Francisco, California, USA *Verification of the proton beam position in the patient by the prompt gamma rays emission.* (San Franscico)

Kanai T, Endo M, Minohara S, Miyahara N, Koyama-Ito H, Tomura H, Matsufuji N, Futami Y, Fukumura A, Hiraoka T, Furusawa Y, Ando K, Suzuki M, Soga F and Kawachi K 1999 *BIOPHYSICAL CHARACTERISTICS OF HIMAC CLINICAL IRRADIATION SYSTEM FOR HEAVY-ION RADIATION THERAPY*

Kanazawa M, Kitagawa A, Kouda S, Nishio T, Torikoshi M, Noda K, Murakami T, Suda M, Tomitani T, Kanai T, Futami Y, Shinbo M, Urakabe E and Iseki Y 2002 Application of an

RI-beam for cancer therapy: In-vivo verification of the ion-beam range by means of positron imaging *Nucl. Phys. A*

Karger C P, Jäkel O, Palmans H and Kanai T 2010 Dosimetry for ion beam radiotherapy *Phys. Med. Biol.* **55** R193–234

Kitagawa A, Furusawa Y, Kanai T, Kanazawa M, Mizuno H, Muramatsu M, Sato S, Suda M, Tomitani T, Urakabe E, Yoshimoto M, Li Q, Wei Z, Hanawa K, Iseki Y and Sato K 2006 Medical application of radioactive nuclear beams at HIMAC *Rev. Sci. Instrum.* **77**

Kraan A C 2015 Range Verification Methods in Particle Therapy: Underlying Physics and Monte Carlo Modeling. *Front. Oncol.* **5** 150

Krimmer J, Dauvergne D, Létang J M M and Testa É 2018 Prompt-gamma monitoring in hadrontherapy: A review *Nucl. Instruments Methods Phys. Res. Sect. A Accel. Spectrometers, Detect. Assoc. Equip.* **878** 58–73

Maccabee H D, Madhvanath U and Raju M R 1969 Tissue activation studies with alpha-particle beams. *Phys. Med. Biol.* **14** 213–24

Mackin D, Peterson S, Beddar S and Polf J C 2012 Evaluation of a stochastic reconstruction algorithm for use in Compton camera imaging and beam range verification from secondary gamma emission during proton therapy *Phys. Med. Biol.* **57** 3537–3353

Marion J B 1974 THE EFFECTS OF NUCLEAR RADIATIONS *Energy in Perspective* (Elsevier) pp 140–69

Min C H, Kim C H, Youn M Y and Kim J W 2006 Prompt gamma measurements for locating the dose falloff region in the proton therapy *Appl. Phys. Lett.* **89**

Minhoara S, Fukuda S, Kanematsu N, Takei Y, Furukawa T, Inaniwa T, Matsufuji N, Mori S and Noda K 2010 Recent Innovations in Carbon-Ion Radiotherapy *J. Radiat. Res.* **51** 385–92

Minohara S, Fukuda S, Kanematsu N, Takei Y, Furukawa T, Inaniwa T, Matsufuji N, Mori S and Noda K 2010 Recent Innovations in Carbon-Ion Radiotherapy *J. Radiat. Res* **51** 385–92

Mohamad O, Makishima H and Kamada T 2018 Evolution of Carbon Ion Radiotherapy at the National Institute of Radiological Sciences in Japan. *Cancers (Basel).* **10**

Mohamad O, Sishc B J, Saha J, Pompos A, Rahimi A, Story M D, Davis A J and Kim D W N 2017 Carbon ion radiotherapy: A review of clinical experiences and preclinical research, with an emphasis on DNA damage/repair *Cancers (Basel).* **9** 1–30

Mohammadi A, Tashima H, Iwao Y, Takyu S, Akamatsu G, Nishikido F, Yoshida E, Kitagawa A, Parodi K and Yamaya T 2019 Range verification of radioactive ion beams of ^{11}C and ^{15}O using in-beam PET imaging *Phys. Med. Biol.* **64** 145014

Moore. C S, Wood. T J, Avery G, Balcam S, Needler L, Smith A, Saunderson J R and Beavis A W 2015 Investigating the use of an anti-scatter grid in digital CR chest radiography *Hull East York Hosp. NHS Trust* **86** 1–7

Newhauser W D and Zhang R 2015 The physics of proton therapy. *Phys. Med. Biol.* **60** R155--209

Nie W, Jones K C, Petro S, Kassaee A, Sehgal C M and Avery S 2018 Proton range verification in homogeneous materials through acoustic measurements *Phys. Med. Biol.* **63**

Paganetti H 2012 Range uncertainties in proton therapy and the role of Monte Carlo simulations. *Phys. Med. Biol.* **57** R99--117

Palta J R 2014 53rd PTCOG meeting Shanghai, China *Understanding the Uncertainties in Proton Therapy* (Shanghai)

Park J H, Kim S H, Ku Y, Kim C H, Lee H R, Jeong J H, Lee S B and Shin D H 2019 Multi-slit prompt-gamma camera for locating of distal dose falloff in proton therapy *Nucl. Eng.*

Technol. **51** 1406–16

Park S H and Kang J O 2011 Basics of particle therapy I: physics *Radiat. Oncol. J.* **29** 135

Parodi K 2016 On- and off-line monitoring of ion beam treatment *Nucl. Instruments Methods Phys. Res. Sect. A Accel. Spectrometers, Detect. Assoc. Equip.* **809** 113–9

Parodi K, Bortfeld T, Enghardt W, Fiedler F, Knopf A, Paganetti H, Pawelke J, Shakirin G and Shih H 2008 PET imaging for treatment verification of ion therapy: Implementation and experience at GSI Darmstadt and MGH Boston *Nucl. Instruments Methods Phys. Res. Sect. A Accel. Spectrometers, Detect. Assoc. Equip.* **591** 282–6

Parodi K, Paganetti H, Shih H A, Michaud S, Loeffler J S, DeLaney T F, Liebsch N J, Munzenrider J E, Fischman A J, Knopf A and Bortfeld T 2007 Patient study of in vivo verification of beam delivery and range, using positron emission tomography and computed tomography imaging after proton therapy. *Int. J. Radiat. Oncol. Biol. Phys.* **68** 920–34

Parodi K and Polf J C 2018 In vivo range verification in particle therapy *Med. Phys.* **45** e1036–50

Phillips G W 1995 Gamma-ray imaging with Compton cameras *Nucl. Inst. Methods Phys. Res. B* **99** 674–7

Pinto M, Bajard M, Brons S, Chevallier M, Dauvergne D, Dedes G, De Rydt M, Freud N, Krimmer J, La Tessa C, Lï¿½tang J M, Parodi K, Pleskač R, Prieels D, Ray C, Rinaldi I, Roellinghoff F, Schardt D, Testa E and Testa M 2015 Absolute prompt-gamma yield measurements for ion beam therapy monitoring *Phys. Med. Biol.* **60** 565–94

Pinto M, Dauvergne D, Freud N, Krimmer J, Letang J M, Ray C, Roellinghoff F and Testa E 2014 Design optimisation of a TOF-based collimated camera prototype for online hadrontherapy monitoring *Phys. Med. Biol.* **59** 7653–74

Pshenichnov I, Larionov A and Mishustin I 2006 Distributions of positron-emitting nuclei in

proton and carbon-ion therapy studied with GEANT4 Related content PET monitoring with 3He beams *Phys. Med. Biol.*

PTCOG 2020 PTCOG - Facilities in Operation Online: https://www.ptcog.ch/index.php/facilities-in-operation

Richter C, Pausch G, Barczyk S, Priegnitz M, Keitz I, Thiele J, Smeets J, Stappen F Vander, Bombelli L, Fiorini C, Hotoiu L, Perali I, Prieels D, Enghardt W and Baumann M 2016 First clinical application of a prompt gamma based in vivo proton range verification system *Radiother. Oncol.*

Roellinghoff F, Benilov A, Dauvergne D, Dedes G, Freud N, Janssens G, Krimmer J, Létang J M, Pinto M, Prieels D, Ray C, Smeets J, Stichelbaut F and Testa E 2014 Real-time proton beam range monitoring by means of prompt-gamma detection with a collimated camera *Phys. Med. Biol.* **59** 1327–38

Schardt D, Elsässer T and Schulz-Ertner D 2010 Heavy-ion tumor therapy: Physical and radiobiological benefits

Smeets J, Roellinghoff F, Prieels D, Stichelbaut F, Benilov A, Busca P, Fiorini C, Peloso R, Basilavecchia M, Frizzi T, Dehaes J C and Dubus A 2012 Prompt gamma imaging with a slit camera for real-time range control in proton therapy *Phys. Med. Biol.* **57** 3371–405

Solevi P, Muñoz E, Solaz C, Trovato M, Dendooven P, Gillam J E, Lacasta C, Oliver J F, Rafecas M, Torres-Espallardo I and Llosá G 2016 Performance of MACACO Compton telescope for ion-beam therapy monitoring: First test with proton beams *Phys. Med. Biol.*

Testa E, Bajard M, Chevallier M, Dauvergne D, Le Foulher F, Freud N, Létang J M M, Poizat J C C, Ray C, Testa M, Dauvergne D, Bajard M, Poizat J C C, Chevallier M, Létang J M M, Testa E, Le Foulher F, Ray C, Bajard M, Chevallier M, Dauvergne D, Le Foulher F, Freud N,

Létang J M M, Poizat J C C, Ray C and Testa M 2009 Dose profile monitoring with carbon ions by means of prompt-gamma measurements *Nucl. Instruments Methods Phys. Res. Sect. B Beam Interact. with Mater. Atoms* **267** 993–6

Testa E, Bajard M, Chevallier M, Dauvergne D, Le Foulher F, Freud N, Ĺtang J M, Poizat J C, Ray C and Testa M 2008 Monitoring the Bragg peak location of 73 MeVu carbon ions by means of prompt γ -ray measurements *Appl. Phys. Lett.*

Testa M 2010 *Physical measurements for ion range verification in charged particle therapy* (Lyon: DE L'UNIVERSITE DE LYON)

Tobias C A, Benton E V., Capp M P, Chatarjee A, Cruty M R and Henke R P 1977 PARTICLE RADIOGRAPHY AND AUTOACTIVATION *Int. J. Radiat. Oncol. Biol. Phys.* **3** 35–44

Tsuboi K 2020 Early History of Biology and Clinical Application of Proton Beam Therapy *Proton Beam Radiotherapy* (Springer Singapore) pp 9–21

Tsujii H and Kamada T 2012 A Review of Update Clinical Results of Carbon Ion Radiotherapy *Jpn. J. Clin. Oncol.* **42**

Urakabe E, Kanai T, Kanazawa M, Kitagawa A, Noda K, Tomitani T, Suda M, Iseki Y, Hanawa K, Sato K, Shimbo M, Mizuno H, HIRATA Y, Futami Y, Iwashita Y and Noda A 2001 Spot Scanning Using Radioactive 11 C Beams for Heavy-Ion Radiotherapy *Jpn. J. Appl. Phys* **40** 2540–8

Wilson R R 1946 Radiological use of fast protons. *Radiology* **47** 487–91

Xie Y, Bentefour E H, Janssens G, Smeets J, Vander Stappen F, Hotoiu L, Yin L, Dolney D, Avery S, O'Grady F, Prieels D, McDonough J, Solberg T D, Lustig R A, Lin A and Teo B-K K 2017 Prompt Gamma Imaging for In Vivo Range Verification of Pencil Beam Scanning Proton Therapy *Int. J. Radiat. Oncol.* **99** 210–8

Yan Y-L, Liu X-G, Dai Z-Y, Ma Y-Y, He P-B, Shen G-S, Ji T-F, Zhang H and Li Q 2017 Spot-scanning beam delivery with laterally- and longitudinally-mixed spot size pencil beams in heavy ion radiotherapy *Chinese Phys. C* **41** 98201

Zarifi M, Guatelli S, Qi Y, Bolst D, Prokopovich D and Rosenfeld A 2019 Characterization of prompt gamma ray emission for in vivo range verification in particle therapy: A simulation study *Phys. Medica* **62** 20–32

Zheng Y, Kang Y, Zeidan O and Schreuder N 2016 An end-to-end assessment of range uncertainty in proton therapy using animal tissues *Phys. Med. Biol.* **61** 8010–24

Zhu X, España S, Daartz J, Liebsch N, Ouyang J, Paganetti H, Bortfeld T R and El Fakhri G 2011 Monitoring proton radiation therapy with in-room PET imaging *Phys. Med. Biol.* **56** 4041–57

Ziegler J F, Ziegler M D and Biersack J P 2010 SRIM - The stopping and range of ions in matter (2010) *Nucl. Instruments Methods Phys. Res. Sect. B Beam Interact. with Mater. Atoms* **268** 1818–23

Chapter 2: Carbon-11 and Carbon-12 Beam Range Verifications through Prompt Gamma and Annihilation Gamma Measurements: Monte Carlo Simulations

Ananta Raj Chalise[1], Yujie Chi[1], Youfang Lai[1], Yiping Shao[2], Mingwu Jin[1]

1 Physics, University of Texas at Arlington, Arlington, TX 76051, USA

2 Radiation Oncology, University of Texas Southwestern Medical Center, Dallas, TX 75390, USA

E-mail: mingwu@uta.edu

(Submitted in Biomedical Physics & Engineering Express)

Abstract

Range uncertainty remains a big concern in particle therapy, as it may cause target dose degradation and normal tissue overdosing. Positron Emission Tomography (PET) and prompt gamma imaging (PGI) are two promising modalities for range verification. However, the relatively long acquisition time of PET and the relatively low yield of PGI pose challenges for real-time range verification. In this paper, we explore using Carbon-11 (C-11) ion beams to enhance the gamma yield to improve PET and PGI by using Monte Carlo simulations of water and PMMA phantoms at four incident energies (95, 200, 300, and 430 MeV/u). Prompt gammas (PGs) and annihilation gammas (AGs) were recorded for post-processing to mimic PGI and PET imaging, respectively. We used both time-of-flight (TOF) and energy selections for PGI, which boosted the ratio of PGs to background neutrons to 2.44, up from 0.87 without the selections. The ion inelastic process channel produced more PGs than the other channels, with a sharp drop in PG counts near the Bragg peak. At the lowest incident energy (100 MeV), PG yield from C-11 was 0.82 times of that from C-12, while AG yield from C-11 was 6~11 folds higher than from C-12 in PMMA. At higher energies, PG differences between C-11 and C-12 were much smaller, while AG yield from C-11 was 30%~90% higher than from C-12 using minute-acquisition. With minute-acquisition time, the AG depth distribution of C-11 showed a sharp peak coincident with the Bragg peak due to the decay of the primary C-11 ions, but that of C-12 had no such one. The high AG yield and distinct peaks could lead to more precise range verification of C-11 than C-12. These results demonstrate that using C-11 ion beams for potentially combined PGI and PET has great potential to improve online range verification accuracy and precision.

2.1. INTRODUCTION

Over the past twenty years, hadron therapy, also known as particle therapy, has advanced greatly and demonstrated therapeutic efficacy in clinic (Le Foulher *et al* 2010, Testa *et al* 2009, Mohamad *et al* 2018). Hadron therapy has the advantages of a sharper energy deposition at the Bragg peak and a higher relative biological effectiveness (RBE) than conventional radiotherapy using X-ray or electron beams, so it can spare the normal tissue better and potentially improve treatment outcomes for deep-seated and radio-resistant tumors (Ebner and Kamada 2016, Le Foulher *et al* 2010, Testa *et al* 2009). Yet, in current clinical practice, multiple factors can reduce the precision of the actual dose delivered to the patients, thus causing treatment beam range uncertainty that can diminish the physical and biological advantages of hadron therapy (Parodi and Polf 2018). The uncertainty can arise from dose computation for treatment planning, pre-treatment patient setup, or during-treatment tumor motion, among other sources (Paganetti 2012, Palta 2014, Zheng *et al* 2016). The total magnitude of the uncertainty can be 2.5~3.5% of the beam range (Paganetti 2012, Krimmer *et al* 2018). Consequently, the target may not receive as high a dose as was prescribed, thus reducing the probability of tumor control (Paganetti 2012). In addition, the surrounding normal tissues may be exposed to substantial over-dose of particle irradiation, which can result in excessive radiation-induced toxicity.

In recent years, great efforts have been taken to address the beam range uncertainty issue. Based on the physical principles involved, three main directions of technology development have emerged: prompt gamma imaging (PGI), positron emission tomography (PET) and acoustic wave measurement (Enghardt *et al* 1999, Min *et al* 2006, Nie *et al* 2018). PGI- and PET-based range verifications have been developed based on secondary electromagnetic radiations. Specifically, in the PGI-based method, the longitudinal distribution of the prompt gammas emitted from the

nuclear interaction between the incident particle and the target correlates highly with depth dose profile (Jongen and Stichelbaut 2003). In the PET-based method, the positron decay of the positron emission nuclei (PEN) generated from the beam-target collision is also found to have a good relationship with the depth dose distribution (Maccabee *et al* 1969). The acoustic wave-based measurement utilizes the mechanical waves from hadron-atom interactions for range verification (Nie *et al* 2018).

The acoustic wave-based method is still in early stages of development and has yet to be applied clinically, but the PGI- and PET-based methods have been implemented in the clinic (Richter *et al* 2016, Ferrero *et al* 2018, Nie *et al* 2018). To date, there have been multiple experimental studies of PGI in proton and carbon ion therapies (Min *et al* 2006, Testa *et al* 2008, Pinto *et al* 2015). Recently, a prototype PGI system was studied in a clinical trial for proton therapy (Richter *et al* 2016, Xie *et al* 2017). Yet, because of the low absolute yield, for example, with $(16 \pm 0.07_{stat} \pm 1_{sys}) \times 10^{-6}$ $ion^{-1}\,mm^{-1}\,sr^{-1}$ for 160 MeV protons in a PMMA phantom (Pinto *et al* 2015), the precision for the PGI image is relatively low. As Xie *et al* (2017) found, without lateral spot aggregation, the precision in shift retrieval better than 2 mm was only 1% of the analyzed spots (59 out of 5801 spots). Even with a 7 mm aggregation, that percentage was still as low as 46%. This low precision of PGI due to the low yield is a great obstacle for more advanced beam range verification, such as a single treatment spot-based verification. The PET based-method has recently been used in clinic for proton therapy (Ferrero *et al* 2018, Zhu *et al* 2011, Parodi *et al* 2007) and carbon therapy (Bauer *et al* 2013, Parodi *et al* 2008, Enghardt *et al* 1999) but because of the intrinsic property of the PEN decay process, the acquisition time of PET signal can be long if a high quality PET is desired. Ferrero *et al* (2018) revealed that achieving a beam range agreement around 1 mm would require an acquisition and reconstruction time for PET imaging of

about 2~3 minutes. It would be very challenging, therefore, to obtain range verification using PET in a real-time format.

A potential way to overcome the challenge of the relatively long acquisition time when using PET for range verification is to utilize radioactive ion beams. It is more challenging to produce and transport radioactive ion beams than stable isotope beams. However, there have been efforts worldwide to achieve this possibility. Lawrence Berkeley National Laboratory in the US pioneered this study four decades ago (Chatterjee *et al* 1981) and was followed by the National Institute of Radiological Sciences (NRIS) in Japan (Urakabe *et al* 2001, Kanazawa *et al* 2002, Kitagawa *et al* 2006, Mohammadi *et al* 2019). Recent progress at the NRIS enabled radioactive beam based range verification before irradiating with stable C-12 ions for treatment (Kitagawa *et al* 2006, Mohammadi *et al* 2019). At the same time, recent advancements in C-11 production provide further opportunities to replace C-12 ion beam with radioactive C-11 ion beams for hadron therapy (Augusto *et al* 2016).

In addition to using radioactive ions, using the combined modalities of PET and PGI has also been proposed to exploit the advantages of both modalities. Parodi (2016) outlined the possibility of combining these modalities in such a way that PGI and PET could be synchronized with the microstructure of the beam delivery to collect PGI data during the beam-on burst and PET data during the beam-off part of the treatment. Although the combination may compromise the performance of PET or PGI individually, the complementary information from two modalities could outweigh slight decreases in individual performance and pave new avenues for real-time ion beam verification and monitoring.

In this work, we used Monte Carlo simulation to analyze prompt gammas (PG) for PGI and annihilation gammas (AG) for PET using C-11 and C-12 at a single-spot level with a single

ion-beam pulse. This work will provide preliminary evidence to support the feasibility of using C-11 ions to improve range verification with both PGI and PET. The paper is organized as follows: Section 2 describes methods and materials for all test cases to quantify the PG yield and the AG yield from C-11 and C-12 with respect to the basic detector responses. Then, Section 3 presents the simulation results. Finally, Section 4 provides discussion and conclusions.

2.2. METHODS AND MATERIALS

We used the Geant4 Monte Carlo simulation package (Agostinelli *et al* 2003) to comprehensively investigate the PG and AG yields of C-11 and C-12 ion beams. The quantities of interest are the dose distribution, the gamma intensity and distributions (for both PGI and PET) and the neutron background. We also investigated the collimator effects and the detector responses with different approaches.

2.2.1. Simulation Setup

2.2.1.1 Physics lists used in GEANT4

To accurately compare the two species of carbon ions, we chose the Quark Gluon String Pre-compound (QGSP) Binary Ion Cascade (BIC) High Precision (HP) model from Geant4 version 10.3.p02 as suggested by Zarifi *et al* (2019). In this model, QGSP defines the hadronic models for nucleons, BIC defines the inelastic models for ions, and the HP Neutron model particularly emphasizes neutrons. BIC is one of the nuclear models recommended to perform simulations for hadron therapy (Dudouet *et al* 2013). This model uses Gaussian wave functions to describe the participating particles and, thus, is a hybrid model of the classical cascade code and the quantum molecular dynamics (QMD) description. In addition, the standard electromagnetic model (“opt4”) was used. The other physics lists included G4DecayPhysics,

G4RadioactiveDecayPhysics, G4IonBinaryCascadePhysics, G4EmExtraPhysics, G4HadronElasticPhysicsHP and G4StoppingPhysics.

2.2.1.2 Beam conditions

In this study, we simulated pencil beam scanning (PBS). PBS is preferable to passive scattering, because it has the advantage of achieving both distal and proximal dose conformality (Chuong *et al* 2018). The size of the pencil beam followed a Gaussian distribution of 0 ± 2 mm (mean ± standard deviation), which is consistent with the literature (Yan *et al* 2017). We also considered a specific time structure of the pulsed beam delivery in the simulation: the ions were assumed to be delivered within a single pulse of a normal distribution with 1 nano-second full-width half-maximum (FWHM) (Pinto *et al* 2015).

For the energy of the simulated ions, we considered four representative energy levels covering the entire therapeutic energy range of carbon ions: 95, 200, 300 and 430 MeV/u for C-12 ion beam (Kanai *et al* 1999, Mohamad *et al* 2018, Tsujii and Kamada 2012). The energies for the corresponding C-11 ion beams were then obtained via Monte Carlo simulation with the criteria of matching the Bragg peak location of C-12 ions within 0.4 mm.

2.2.1.3 Experimental configuration

The geometrical setup was as follows. A homogenous phantom made of water or PMMA with a size of 50×50×500 (x-y-z)) mm^3 and a voxel size of 1 mm^3 was used as the target. Therapeutic C-11 and C-12 beams were delivered 3 mm away from the phantom along the z direction of the phantom. Inside the phantom, dose deposition events were recorded in the voxelized geometry. The gamma and neutron events generated from the beam-phantom interaction were recorded with their positions, motion directions, energies, yielding channels and time within the phantom detector and stored in the phase space file (PSF). These gammas and neutrons were

recorded until they travel outside the phantom detector, so that scattering and other effects during the particle transport inside the phantom after their creation were recorded in our simulation. A history of 10^7 incident particles were simulated ten times in all study cases, unless otherwise stated. PG and AG detection and data processing are detailed in the next two sections.

2.2.2 PG detection and data processing

2.2.2.1 PG data processing to mimic ideal collimated detection

Because most published experimental data are based on mechanically collimated cameras, we developed a processing algorithm to mimic the behavior of a slit collimator behavior (Figure 1a), which was used in the GANIL experiment (Pinto *et al* 2015). Specifically, the ring-shaped collimator with a 2 mm slit opening, 20 cm long, and a full-ring angular coverage, was applied perpendicularly to the beam direction, that is, the z-axis plane in our processing algorithm. For a particular collimator position along the z-axis, gammas from the PSF were first transferred to the inner cylindrical surface representing the bottom of the collimator (Figure 1b) with its position calculated based on the line cylindrical surface interaction (Chi *et al* 2016). After this step, only those gamma photons between the collimator openings were kept. The selected gammas were then further transferred to the outer cylindrical surface defining the top of the collimator (Figure 1b). Again, only those that stayed inside the collimator opening were selected. Gammas that passed through these two steps were considered the ones that reached the detector and, thus, were recorded. The collimator was shifted subsequently in 2-mm steps along the z-axis to record a completed PG depth profile along the entire beam line. Although this ideal analytic method omits interactions between gammas and the collimator and the detector, it provides a good approximation

and greatly reduces computational time. The accuracy of this method is further studied in Section 2.2.2.2.

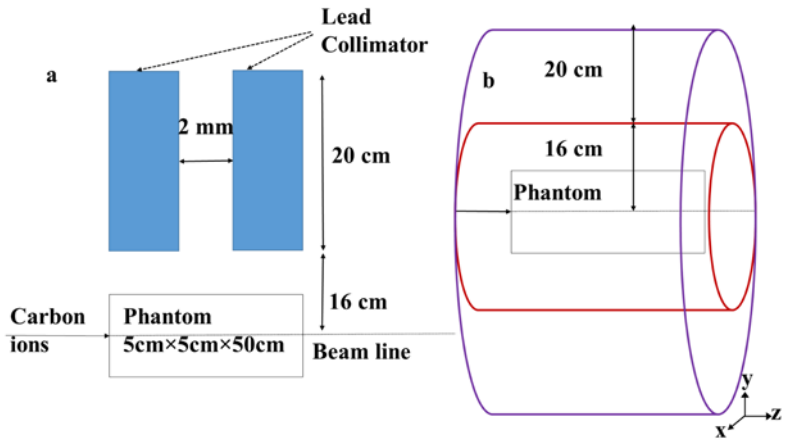

Figure 2.1: Illustration of experimental setup: (a) a single slit collimator for PGI; (b) two cylindrical surfaces used to calculate photons passing through the slit collimator.

In addition to the collimator selection, time-of-flight (TOF) and energy criteria were also applied to select gammas. A combination of TOF and energy selection methods (Testa *et al* 2008) enables the discrimination of PG signals from neutrons and neutron-associated components and improves the signal-to-background ratio (SBR) (Pinto *et al* 2015). The recorded PG TOF is defined as the time interval between the origin of primary particles (3 mm from the phantom) and the position where the PG is recorded just before leaving the phantom. The PGs within the energy range of 2 MeV to 7 MeV and with TOFs inside the TOF window of peak time $\pm 2\sigma$ (standard deviation) were selected to improve the SBR.

2.2.2.2 MC simulation of collimated PG detection with an ideal detector

To investigate how much the scatter caused by the collimator would influence the gamma detection compared to the post-processing method described in section 2.2.2.1, we also conducted

a simulation with an ideal ring detector (Figure 2.2). In this simulation, we used two cylindrical lead rings 2 mm apart from each other (red and navy blue in Figure 2.2b) as a collimator around the phantom and placed an ideal ring detector (green) around the collimator. The dimensions of the phantom, collimator and detector are tabulated in Figure 2.2c. We simulated delivering two million C-12 ions per run with energy of 95 MeV/u to the water phantom. We simulated ten runs each for two cases, one in vacuum and the other in air. The same TOF and energy cutoffs as in 2.2.1 were applied to the gamma photons detected by the ideal detector.

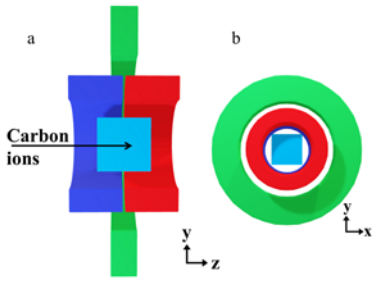

c Dimensions for the ideal detector setup

Parts	Details
Phantom	$5\times5\times50$ cm^3 (x-y-z)
Collimator 1 & 2	50-250 mm (radial), 30 mm (z)
Detector	600-800 mm (radial), 20 mm (z)

Figure 2.2 : Ideal detector setup for collimated PGI. a) Side view with the phantom (sky blue) at the center surrounded by the cylindrical collimator (red and blue) and the cylindrical detector (green). b) Transverse view of the phantom (sky blue) at the center surrounded by the cylindrical collimator (red) and the cylindrical detector (green) (figures are not drawn to scale). c) Dimensions for the ideal detector setup.

2.2.3 AG detection and processing

2.2.3.1 Processing to obtain AG signal without detector response

The gammas with the generation type of annihilation and energy of 511 keV were first selected from the PSFs (see 2.2.1.3). The selected gammas were then sorted with their TOF and paired with a 1 nano-second time interval. The directions of the paired gammas were then checked

to choose coincident AGs. Afterwards, these AGs were traced back to the beam line to obtain the 1D AG profile. This is equivalent to an ideal PET imaging without detector response.

2.2.3.2. Simulation and processing of AGs with detector response

To take the PET detector response into consideration, we further transported, recorded and paired PSFs containing AGs inside a PET system by using GATE8.0 to get coincident pairs. Specifically, a cylindrical PET system was simulated with its z-axis aligned with the ion beam direction and 30 panels uniformly distributed around the phantom (in the x-y plane) (Figure 2.3a). The inner and outer surfaces of the detector panels were 50 mm and 70 mm away, respectively, from the central beam line. Each panel was made of a parallel LSO crystal array with an array size of 10x300 (tangential × z) and a crystal size of 20 mm (radial) × 1 mm (tangential) × 1 mm (z-axis). There were no gaps between crystals. After the hit events, directly resulting from gamma energy deposition were obtained inside the crystals, the energy resolution of 19% at 511 keV and the energy window of 350-700 keV were used to form singles from hit events. The singles were then processed by the coincidence sorter, with a window and offset of 1 and 0 ns, respectively. After coincident pairs were generated from the sorting process, the PET image was then reconstructed via a crystal index-based method, where the event positions were assumed to be detectable only at the resolution of the single crystal. Thus, the central position of the inner surface of the crystal was used to represent the positions of those events belonging to that crystal, and they were retraced back to the beam line.

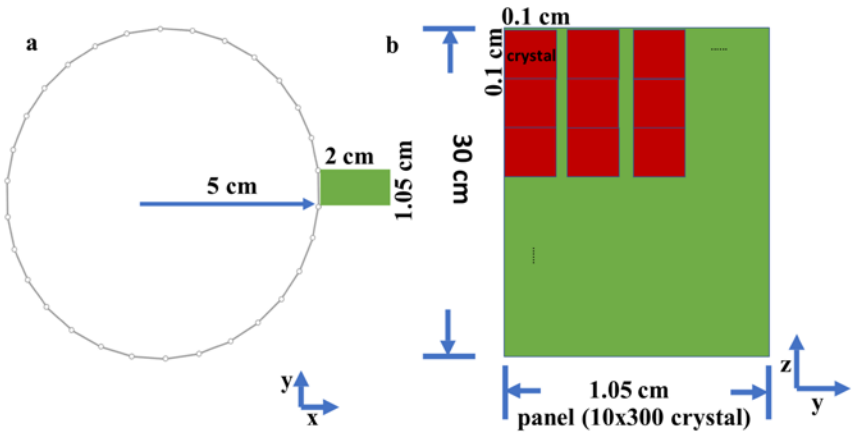

Figure 2.3 Illustration of PET with detector response: (a) PET setup and (b) detector panel/crystals. Thirty panels around the phantom were used with inner and outer diameters of 10 cm and 14 cm, respectively.

In the both procedures described in Sections 2.2.3.1 and 2.2.3.2, we also investigated the effect of different acquisition times on PET signal quality. Here, the AG acquisition time was defined as the time starting at the origination of the primary particles. PET signal reconstructions using the acquisition times of 1, 3, 5 seconds and 1, 3, 5 minutes were performed in both cases.

2.3 RESULTS

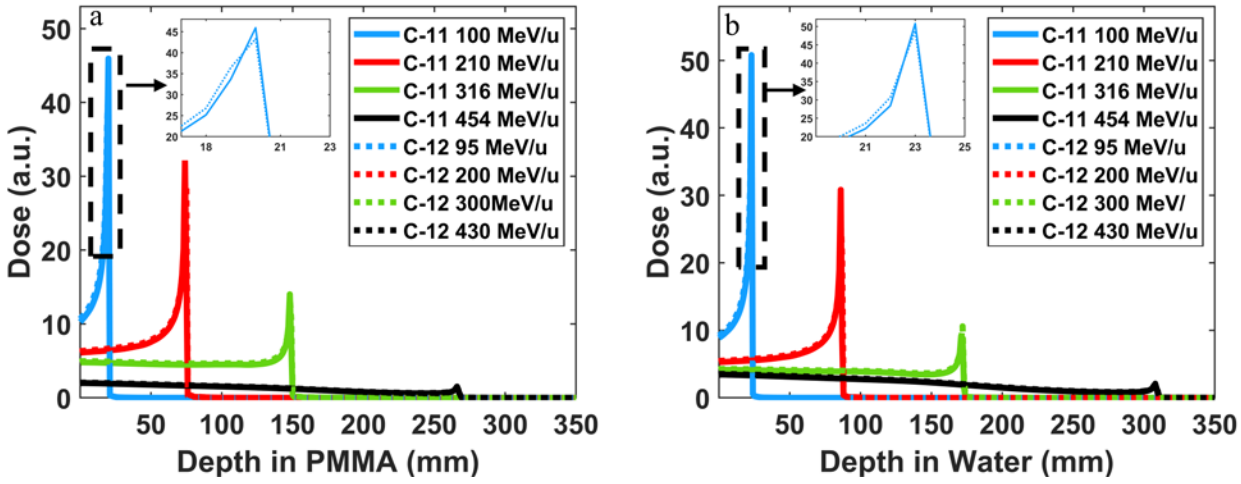

Figure 2.4 Depth dose profile of C-11 and C-12 at different energies in a) PMMA phantom and in b) water phantom

2.3.1. Results for ideally collimated PG detection

The energy tuning results for the C-11 beam with regard to depth dose distribution for the Water and PMMA phantoms are shown in Figure 2.4. As can be seen, the dose profiles from paired C-12 and C-11 beams are similar to each other. The Bragg peak positions from the two ion species were matched with each other within 0.4 mm. The incident energies for the C-11 ions were 100, 210, 316 and 454 MeV/u in both water and PMMA phantoms, which corresponded to the incident energies for C-12 ions at 95, 200, 300 and 430 MeV/u, respectively.

The results of the TOF windows for both C-11 and C-12 beams are shown in Table 2.1 (2nd column). The TOF window was similar for C-11 and C-12 at the same energy level for the same material. The TOF window was 0.03-0.24 ns narrower for the PMMA phantom than for the

water phantom at different incident ion energies. It was 1.03-1.30 ns broader at the highest (430/454 MeV/u) than at the lowest (95/100 MeV/u) energy because of the longer traveling distance.

After applying the TOF window to select PGs, we applied the same TOF window to the corresponding neutrons to obtain the neutron background for the highest incident ion energy (Figure 2.5a). The TOF profiles of PGs and neutrons mostly overlapped when the energy cutoff was not applied. After the energy cutoff (2-7 MeV) was applied to both PGs and neutrons, the profiles of neutrons were skewed to the right, which suppressed the neutron background in the TOF windows (Figure 2.5b). With both TOF and energy cutoffs, the ratio of PGs to neutrons increased to 2.44, up from 0.87 without these cutoffs (for C-12 430 MeV/u). We observed similar behavior for other incident ion energies.

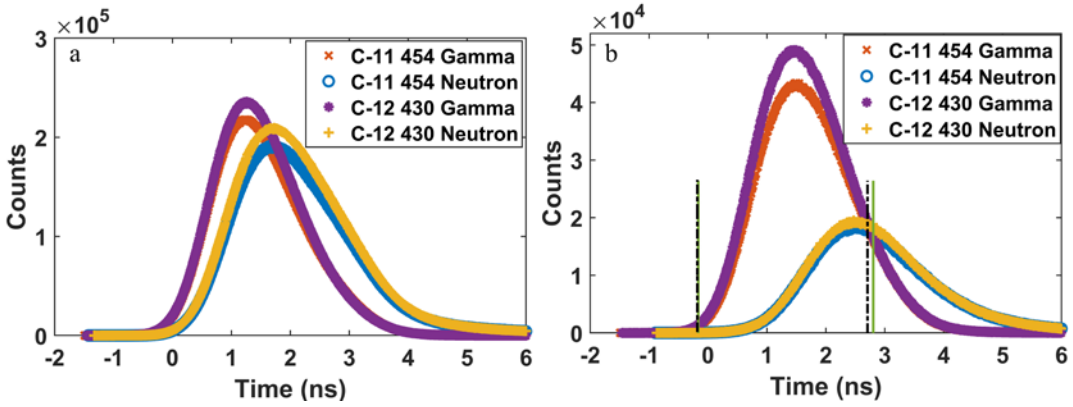

Figure 2.5 Time-of-flight (TOF) profiles for gammas and neutrons in PMMA for C-11 and C-12 at high incident energy (430/454 MeV/u) before energy cut-off (a) and after energy cut-off (b) (green vertical lines represent TOF window for C-12 430 MeV/u, and black lines represent TOF window for C-11 454 MeV/u).

The absolute yields of PGs generated from 10^7 C-11 and C-12 ions for the lowest energy and highest energy cases in Water are shown in Figure . Although the PG yield of C-11 was slightly lower than that of C-12, both C-11 and C-12 demonstrated a clear fall-off close to the Bragg peak that could be utilized for range verification. The PG counts at the peak and the ratio between C-11 and C-12 are listed in the 3^{rd} and 4^{th} columns of Table 1, respectively. A few hundred counts were detected in a 2-mm bin. The counts at the peak also decreased as the energy increased, because ions traveled a longer distance at higher energies for a broader PG distribution. The ratios of PG yield between C-11 and C-12 were generally higher than 80% for both water and PMMA phantoms; the only exception was for the lowest energy in water.

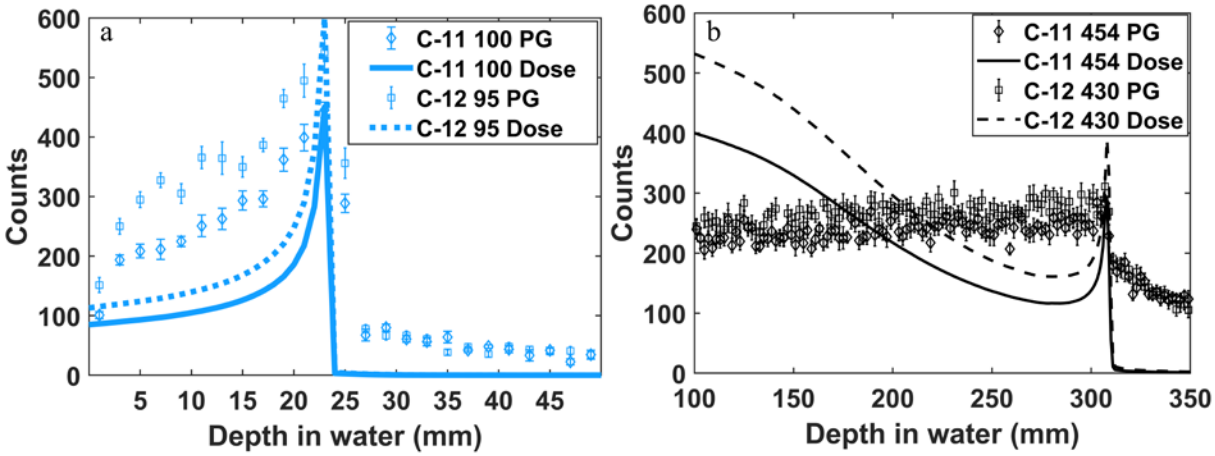

Figure 2.6: Depth profiles of prompt gammas (PGs) generated in Water along with depth dose profiles (in arbitrary scale for reference) for C-11 100 MeV/u and C-12 95 MeV/u (a) and C-11 454 MeV/u and C-12 430 MeV/u (b). Error bars were calculated as standard deviation from 10 runs of 10 million particles

Table 2.1: Time-of-Flight (TOF) windows for both Water and PMMA phantoms for **C-11** (**bold**) and C-12 at different energies and the numbers of prompt gammas (PGs) at the gamma photon peak.

E_{C-11}/ E_{C-12} (MeV/u)	TOF Window (ns)		PG counts at γ peak (N/2mm)		N_{C-11}/N_{C-12}	
	Water	PMMA	Water	PMMA	Water	PMMA
100/ 95	**1.83**/ 1.83	**1.83**/ 1.83	**414±22.77**/ 543.6±17.44	**483.2±21.59**/ 585.6±22.16	0.76	0.82
210/ 200	**2.12/** 2.20	**2.09/** 2.16	**445.9±20.76/** 546.5±23.51	**452.7±23.6/** 536.4±18.95	0.81	0.84
316/ 300	**2.51/** 2.60	**2.44/** 2.51	**382.2±14.55/** 456±24.63	**407±20.95/** 448.9±14.73	0.84	0.90
454/ 430	**3.13/** 3.13	**2.89/** 2.97	**284.40±21.23/** 311±15.15	**323.20±11.15/** 353.4±24.04	0.91	0.92

The PG energy spectra obtained for the lowest and highest incident ion energies for both ion species are shown in Figure 2.7. The spectra were similar for both ion species at the same energy level. The characteristic gamma peaks could be seen at 2.3, 3.2, 4.4, 6.1 and 6.9 MeV because of excited carbon and oxygen nuclei.

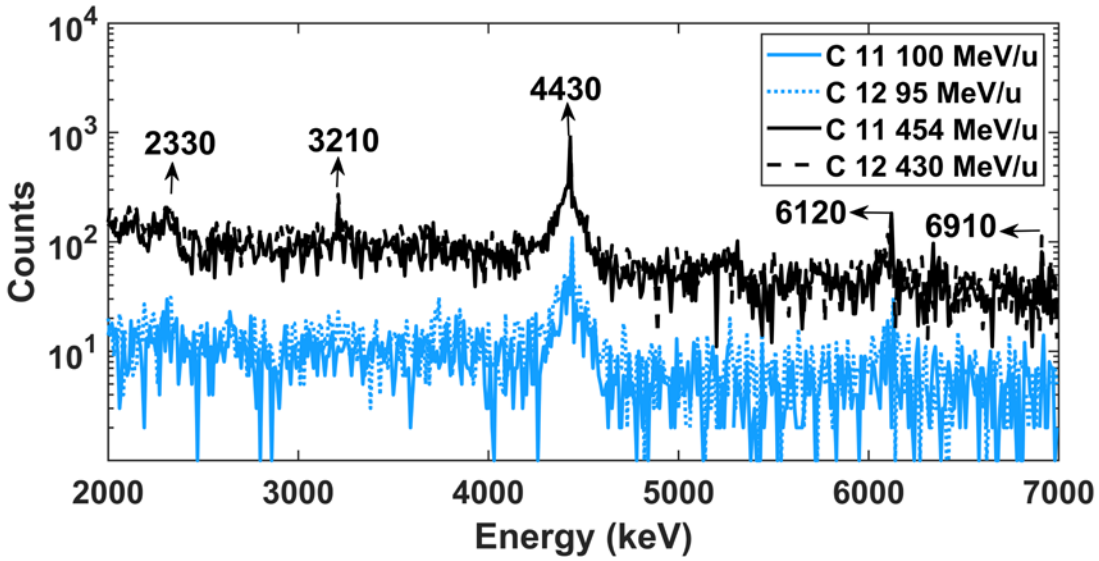

Figure 2.7: Energy spectra for both carbon ion species at lowest and highest incident ion energies in the PMMA phantom.

The different channels that produce PGs are summarized in Figure 2.8. The ion inelastic ("ionInelastic") channel was the dominant generator of PGs (88.35% for C-12 at 95 MeV/u and 82.85% for C-11 at 100 MeV/u) in all cases. However, as the energy of the ion beam increased, the gammas produced by protonInelastic, neutronInelastic and alphaInelastic significantly increased. For C-12 at 430 MeV/u and C-11 at 454 MeV/u in PMMA, the total number of PGs generated by ionInelastic dropped to 42.62% and 35.26%, respectively. Among all the physics channels creating PGs, only ionInelastic demonstrated the sharp drop in PG count near the Bragg peak region, which means this process is an active factor in PGI-based range verification.

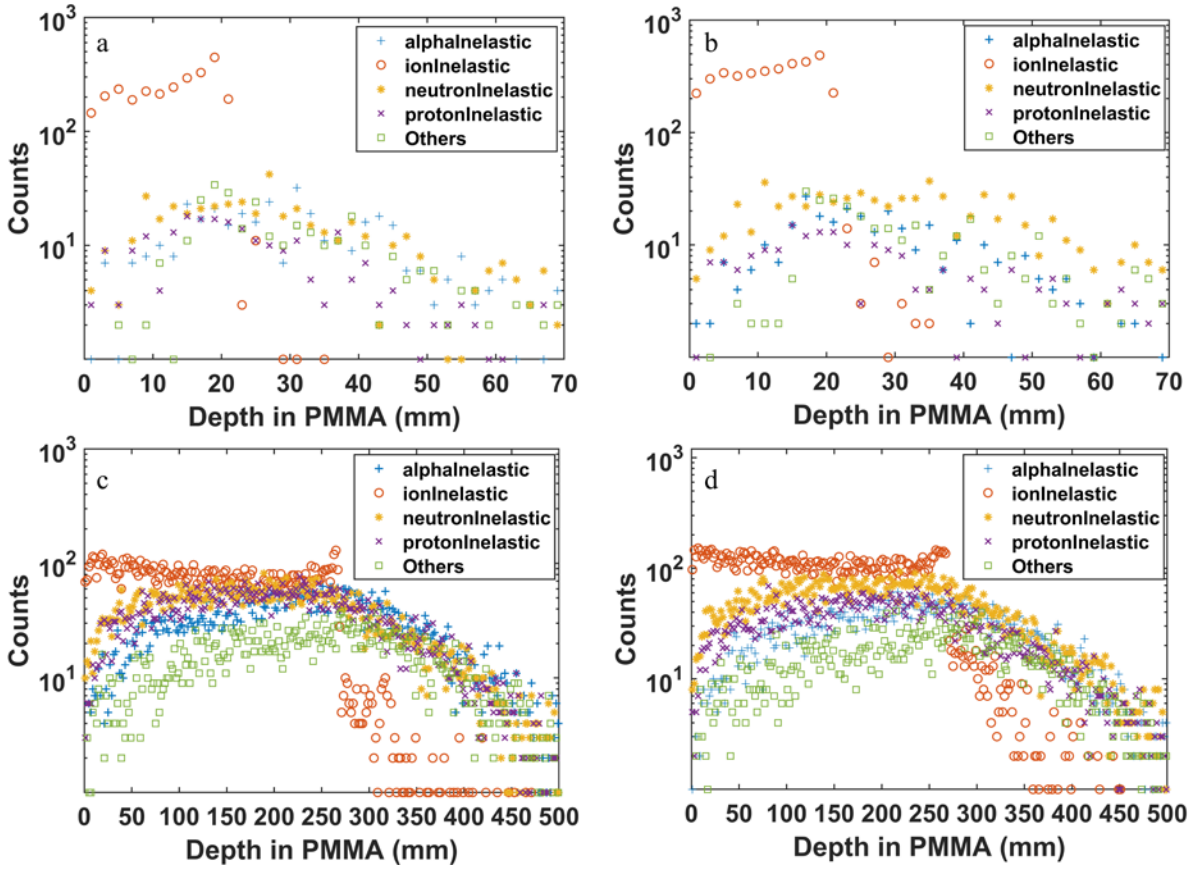

Figure 2.8 Different channels generating prompt gamma (PG) for C-11 at 100 MeV/u (a), C-12 at 95 MeV/u (b), C-11 at 454 MeV/u (c) and C-12 at 430 MeV/u (d) in the PMMA phantom.

2.3.2 Results of MC simulation of more realistic collimated PG detection

To investigate the influence of scatter photons due to the collimator, we performed an MC simulation using a ring collimator as described in Section 2.2.2.2. We simulated two different cases, one in vacuum and the other in air, and the gamma counts at the peak (2-mm bin) are listed in the Table 2.2. For the same case, whether in vacuum or in air, the ideal analytic collimated detection had lower gamma counts ("Ideal") than were detected by the MC simulation ("D"). Note that some of these gammas actually originated outside of the phantom, so the discrepancy between

the ideal ones and the gammas counts from the phantom ("DWP") was smaller. The MC simulation produced more detected gammas than the ideal case because of the penetration and scatter. Therefore, about 70% contamination (in air) may need to be addressed to improve PGI range verification. Because the ideal analytic method uses the PSF to obtain the PGs passing through the collimator (2.2.2.2 and 2.3.1), only one simulation recording the photon history inside the phantom is needed to get a beamline PG profile from post-processing, but a simulation with a realistic collimator needs to simulate PGs at each slit location along the beamline. Thus, the ideal analytic method saves a significant amount of computation time over an MC simulation with a realistic collimator.

Table 2.2: Collimated prompt gamma (PG) counts at the photon peak location (2-mm bin) for the ideal analytical method and the Monte Carlo (MC) simulation method.

Runs	In vacuum			In air		
	D	DWP	Ideal	D	DWP	Ideal
1	160	150	110	177	127	104
2	145	138	108	182	141	98
3	157	150	128	189	145	110
4	157	144	118	175	130	98
5	172	155	116	193	147	107
6	183	166	129	169	134	99
7	156	144	112	164	134	106
8	162	150	107	181	138	109
9	157	147	127	177	142	110
10	147	137	109	147	115	90
Mean	159.6	148.1	116.4	175.4	135.3	103.1
Std. Dev.	11.1	8.4	8.7	13.1	9.6	6.6

Note: D is the number of gammas detected in the detector satisfying the time-of-flight and energy cutoffs based on MC simulation. DWP is the number of gammas that originated inside the phantom. Ideal is the number of gammas obtained from the analytic collimated detection.

2.3.3 AGs for PET without detector response

The coincident pairs of AGs without detector response for the water phantom are listed in Table 3. The number of AG pairs produced by C-11 was 5 times for 1-minute acquisitions and 8 times for 5-minute acquisitions that produced by C-12 at the lowest energy level (95/100 MeV/u).

However, the AG pair ratio between C-11 and C-12 decreased with higher energies and dropped to 1.34 for 1-minute and 1.27 for 5-minute acquisitions at 430/454 MeV/u. For the acquisition time in seconds, the number of AG pairs produced by C-11 was 1.5 to 2.65 times that produced by C-12 for the lowest incident ion energy in water. Similar to the acquisition in minutes, the AG pair ratio between C-11 and C-12 in seconds fell as the incident energy increased and dropped down to 1.09 to 1.23 for the highest incident ion energy in water. For the PMMA phantom, these ratios were even higher (Table 2.4). For the acquisition in minutes, C-11 produced 10.9 (5-minutes) and 6.12 (1-minute) times the number of AG pairs produced by C-12 at the lowest incident ion energy, and the ratios dropped to 1.36 (5-minutes) and 1.39 (1-minute) at the highest energy.

Table 2.3: Comparison of yields of coincident annihilation gamma (AG) pairs for **C-11 (bold)** and C-12 at different energies using different acquisition times in water

E_{C-11}	Number of coincident AG pairs produced in Water ($\times 10^4$)					
E_{C-12}	Time (minutes)			Time (seconds)		
(MeV/u)	5	3	1	5	3	1
100	**82.64 ±0.10**	**54.81 ±0.08**	**22.69 ±0.06**	**3.16 ±0.01**	**2.22 ±0.01**	**1.22 ±0.01**
95	10.01 ±0.03	8.08 ±0.03	4.38 ±0.02	1.19 ±0.01	1.02 ±0.01	0.82 ±0.01
210	**93.98 ±0.060**	**68.93 ±0.04**	**34.91 ±0.04**	**6.91 ±0.02**	**5.37 ±0.02**	**3.70 ±0.02**
200	35.54 ±0.05	28.502 ±0.04	15.16 ±0.03	4.09 ±0.02	3.55 ±0.01	2.96 ±0.01
316	**114.51 ±0.74**	**88.76 ±0.05**	**48.07 ±0.08**	**10.72 ±0.03**	**8.62 ±0.03**	**6.35 ±0.02**
300	67.58 ±0.080	54.12 ±0.08	28.47 ±0.05	7.47 ±0.03	6.45 ±0.03	5.39 ±0.02
454	**139.45 ±0.15**	**111.44 ±0.12**	**61.12 ±0.01**	**14.56 ±0.05**	**12.03 ±0.04**	**9.33 ±0.04**
430	109.41 ±0.08	87.64 ±0.08	45.57 ±0.07	11.80 ±0.03	10.21 ±0.03	8.52 ±0.03

Table 2.4: Comparison of yields of coincident annihilation gamma (AG) pairs for **C-11 (bold)** and C-12 at different energies using different acquisition times in PMMA

E_{C-11}	Number of coincident AG pairs produced in PMMA ($\times 10^4$)					
E_{C-12}	Time (minutes)			Time (seconds)		
(MeV/u)	5	3	1	5	3	1
100	**72.49 ±0.09**	**47.60 ±0.06**	**19.83 ±0.04**	**2.95 ±0.01**	**2.14 ±0.01**	**1.29 ±0.01**
95	6.60 ±0.02	5.32 ±0.02	3.24 ±0.01	1.18 ±0.009	1.06 ±0.008	0.92 ±0.007
210	**74.55 ±0.08**	**54.13 ±0.06**	**28.83 ±0.05**	**6.81 ±0.03**	**5.50 ±0.03**	**4.07 ±0.02**
200	23.10 ±0.02	18.71 ±0.02	11.56 ±0.02	4.31 ±0.01	3.88 ±0.01	3.399 ±0.02
316	**83.69 ±0.07**	**64.61 ±0.05**	**37.95 ±0.04**	**10.45 ±0.04**	**8.72 ±0.04**	**6.82 ±0.04**
300	43.31 ±0.07	34.88 ±0.07	21.07 ±0.05	7.62 ±0.03	6.839 ±0.03	5.95 ±0.03
454	**95.94 ±0.06**	**76.61 ±0.05**	**46.54 ±0.05**	**14.01 ±0.03**	**12.00 ±0.03**	**9.74 ±0.04**
430	70.08 ±0.07	56.17 ±0.06	33.30 ±0.04	11.60 ±0.03	10.37 ±0.03	9.01 ±0.03

The depth distributions of AGs for two representative incident energies for both ion species with different acquisition times in seconds and minutes are shown in Figure 9. The depth distributions of AGs for C-11 showed distinct peaks, which were narrower than those for C-12. Comparing the low incident energy cases (a-d) to the high incident energy cases (e-h), the peaks at low energy were higher and sharper than those at high energy, especially for C-11. Furthermore, the peaks were generally narrower for the acquisitions in minutes than for those in seconds.

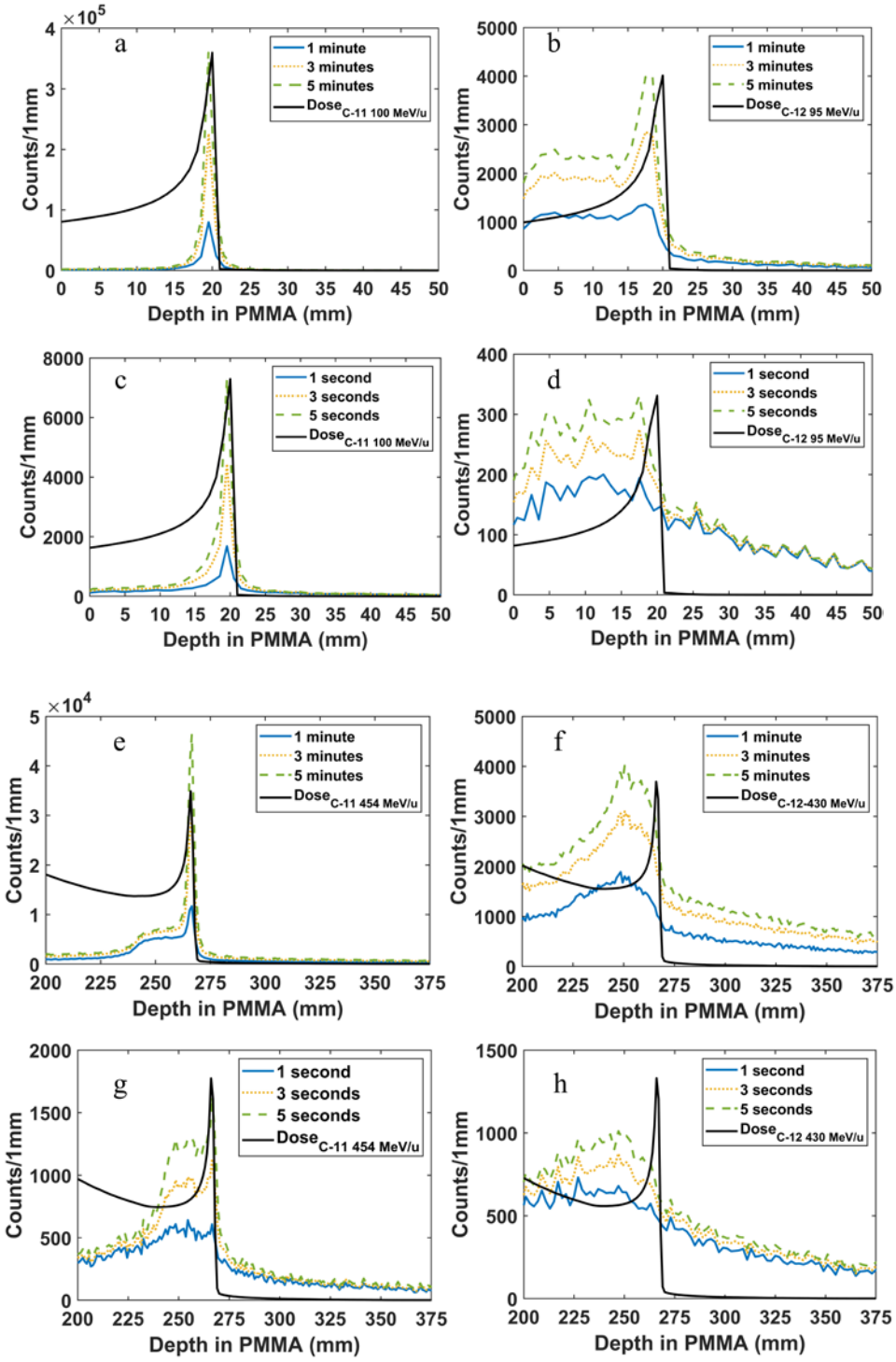

Figure 2.9 Depth distribution of coincident annihilation gamma (AG) pairs without detector response (traced back to the beam line) in PMMA for low incident ion energy (a-d) and for high incident ion energy (e-h).

2.3.4 AGs for PET with detector response

When detector response was taken into account, the number of AG pairs significantly dropped for both carbon ion species at the lowest energy level in PMMA, as can be seen by comparing Table 2.5 with Table 2.4. For 5-minute acquisitions, the number of AG pairs for C-11 was 6.64 times that for C-12. The depth distributions reconstructed by the crystal index-based method for lower energy levels of both ion species are shown in Figure 2.10. The peaks observed with detector response were similar to those without detector response (Figure 2.9).

The FWHM values of the AG distribution peaks with detector response for C-11 are presented for two representative incident energies in Table 2.6. Generally, the higher the count statistics (i.e., longer acquisition times), the smaller the FWHM values. In addition, the FWHM was much smaller for the low energy case than for the high energy case, which is consistent with Figure 2.9. The FWHM values for the 454 MeV/u case using acquisitions in seconds were not calculated, because there were no distinct peaks.

Table 5: The number of coincident annihilation gamma (AG) pairs with detector response at the lowest energy in PMMA.

	5 min	3 min	1 min	5 sec	3 sec	1 sec
C-11 100 MeV/u	**31101.3**	**26379.4**	**15219.9**	**1851.3**	**1168.7**	**449.6**
	±163.03	**±112.96**	**±77.98**	**±42.44**	**±33.18**	**±22.07**
C-12 95 MeV/u	4681.5	3651.87	1986.25	311.87	210.75	97.625
	±52.24	±27.79	±10.59	±14.62	±12.51	±7.77

2.4 DISCUSSION AND CONCLUSION

The major challenge in this study has been the computational time required for each simulation. As detailed in Section 2.2, we used some approximation methods for collimation effects in PGI to alleviate the computational burden. In the literature, C-12 95 MeV/u for the same setup (GANIL) yields 3.2×10^{-7} gammas/ion at the gamma peak for experimental PMMA data (Le Foulher *et al* 2010), which is equivalent to 1.3×10^{-5} gammas/ion when accounting for an annular detector. Similarly, they reported for their simulation 1.3×10^{-6} gammas/ion which is equivalent to 5.4×10^{-5} gammas/ion for an annular detector. In our simulation, we had a count of 5.6×10^{-5} gammas/ion at the gamma peak. Our simulation at 95 MeV/u was similar to their simulation result, which overestimates by a factor of 4.3 compared to the experimental gamma yield by Le Foulher *et al* (2010). More importantly, our simulation reveals the decreasing PG peak yield as the carbon ion incident energy increases, which is consistent with Pinto *et al* (2015). Furthermore, the PG relationship between C-11 and C-12 should not change much if more detailed models of detector response are taken into account in future studies. We plan to study PGI and PET imaging with C-11 further by using realistic detector simulation and advanced image reconstruction methods, which will provide guidance for developing real online range verification PGI and PET systems.

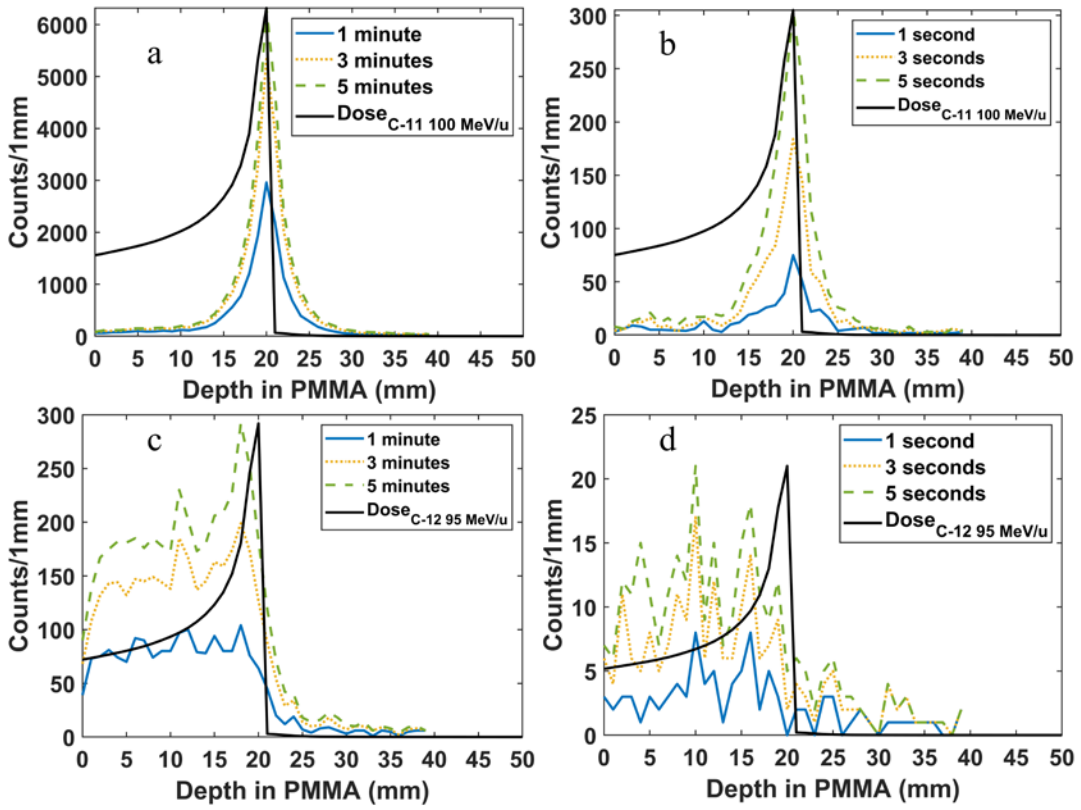

Figure 2.10 : Depth distribution of coincident annihilation gamma (AG) pairs with detector response for (a and b) C-11 100 MeV/u and (c and d) C-12 95 MeV/u for acquisitions in minutes (a and c) and in seconds (b and d) using the crystal index-based reconstruction method.

Table 2.6: Full-width half-maximum values (in mm) of the annihilation gamma (AG) distribution peaks for high and low energies of C-11 at different time ranges.

	5 min	1 min	5 sec	1 sec
C-11 100 MeV/u	3.08	3.25	3.63	3.86
C-11 454 MeV/u	4.64	7.42	-	-

In this study, we comprehensively compared PG yields for C-11 and C-12 ion beams by using Monte Carlo simulation. Our results show that C-11 ion beam can provide 0.75 times the

PG yield of C-12 ion beams in the worst-case scenario, and the PG yield difference between ion species becomes negligible at higher energies. The ion inelastic ("ionInelastic") process is the dominant channel to create PGs and follows a trend similar to the dose profile. Meanwhile, the neutron background increases for both ion-species as the incident energy increases. However, use of TOF and energy filtering substantially reduces the neutron background for PGI. Similar depth distributions of PG yields from C-11 and C-12 are also observed. It is hence reasonable to estimate that similar accuracy level of the PG-based beam range verification can be obtained for C-11 and C-12 beams.

A recent study by Mohammadi *et al* (2019) has showed that the dose peak and the positron peak coincide for mono-energetic C-11 ion beams with an incident energy of 170 MeV/u. Our simulation results are consistent with their findings for C-11 at different energy levels using the simple ray tracing reconstruction without and with detector response (Figures 2.9 and 2.10) within 0.5 mm discrepancy. This small discrepancy (Figure 2.9a and 2.9c) was caused by binning uncertainties in the ray tracing reconstruction process. We further quantitatively investigated the contribution from different AG yielding sources (i.e. PENs) to the peak-to-peak coincidence. Specifically, 100K incident C-11 ions at each energy level were simulated to record the PENs for the positron generation. The positrons generated from the decay of primary C-11 ions at the low incident energy level (100 MeV/u) were ~5.02 folds more than that from the secondary PENs within 5 minutes along the entire beam path, while those at the high energy level (454 MeV/u) were ~4.23 folds less. The significantly reduced contribution from the primary C-11 decay to the positron generation at high incident beam energy was due to the dramatically increased interactions between high energy C-11 ions and the target material. Within one FWHM around the AG peak, the ratios between the positrons generated from decay of primary C-11 and that from secondary

PENs were 20.61 and 6.12 for the 100 MeV/u and 454 MeV/u C-11 beams, respectively. It indicates that the AG peak coincidence with the dose peak in Figures 2.9 and 2.10 was mainly caused by the primary C-11 decay process.

Due to the unique peak distribution and high yielding rate of positrons around the Bragg peak for C-11 beam, we would expect better precision for the AG-based beam range verification using C-11 beams than using C-12 beams. To verify it, we measured the 50% drop-off positions of the AG depth profiles for 5-minute acquisition for both carbon species using 10 runs and computed the standard deviation (STD) of the drop-off positions. The ratio of STD between C-12 and C-11 beams were found to be 5.86 (0.41 mm vs. 0.07 mm) and 12.0 (0.60 mm vs. 0.05 mm) for the lowest and highest energy levels, respectively. It is worth noting that although the absolute value of STD could not be used to directly represent the beam range verification uncertainties, the former is linearly correlated to the latter. Therefore, these ratios indicate that an enhanced precision of 5.86~12 folds using the AG-based beam range verification could be achieved for C-11 beam compared to C-12 beam.

Finally, if simultaneous PGI and PET can be achieved in the future, the slight loss in PGI from using C-11 can be compensated by the large boost in PET. Therefore, using C-11 ions for combined PGI and PET for the ion-range verification in carbon ion therapy is a promising direction.

Acknowledgement

We are grateful to Dr. William (Joe) Allen from Texas Accelerated Computational Center (TACC) for computational resource and technical support. We highly appreciate Dr. Deepak Shrestha from UT Southwestern, for discussions during the initial phase of this study. We are also

thankful to Dr. George Dedes from LMU Munich for his input regarding beam time structure. This work was supported in part by the UT Southwestern Medical Center under a Particle Therapy Seed Grant and by the U.S. National Institutes of Health under Grant No. NIH/NCI R15CA199020-01A1. We thank Dr. Jonathan Feinberg at UT Southwestern for editing the manuscript.

References

Agostinelli S, Allison J, Amako K, Apostolakis J, Araujo H, Arce P, Asai M, Axen D, Banerjee S, Barrand G, Behner F, Bellagamba L, Boudreau J, Broglia L, Brunengo A, Burkhardt H, Chauvie S, Chuma J, Chytracek R, Cooperman G, Cosmo G, Degtyarenko P, Dell'Acqua A, Depaola G, Dietrich D, Enami R, Feliciello A, Ferguson C, Fesefeldt H, Folger G, Foppiano F, Forti A, Garelli S, Giani S, Giannitrapani R, Gibin D, Gómez Cadenas J J J, González I, Gracia Abril G, Greeniaus G, Greiner W, Grichine V, Grossheim A, Guatelli S, Gumplinger P, Hamatsu R, Hashimoto K, Hasui H, Heikkinen A, Howard A, Ivanchenko V, Johnson A, Jones F W W, Kallenbach J, Kanaya N, Kawabata M, Kawabata Y, Kawaguti M, Kelner S, Kent P, Kimura A, Kodama T, Kokoulin R, Kossov M, Kurashige H, Lamanna E, Lampén T, Lara V, Lefebure V, Lei F, Liendl M, Lockman W, Longo F, Magni S, Maire M, Medernach E, Minamimoto K, Mora de Freitas P, Morita Y, Murakami K, Nagamatu M, Nartallo R, Nieminen P, Nishimura T, Ohtsubo K, Okamura M, O'Neale S, Oohata Y, Paech K, Perl J, Pfeiffer A, Pia M G G, Ranjard F, Rybin A, Sadilov S, Di Salvo E, Santin G, Sasaki T, et al 2003 Geant4—a simulation toolkit *Nucl. Instruments Methods Phys. Res. A* **506** 250–303

Allen C, Borak T B, Tsujii H and Nickoloff J A 2011 Heavy charged particle radiobiology: Using

enhanced biological effectiveness and improved beam focusing to advance cancer therapy *Mutat. Res. - Fundam. Mol. Mech. Mutagen.* **711** 150–7

Anon 2012 *Transforming Geant4 for the Future Report from the Workshop on Transforming Geant4 for the Future*

Augusto R S, Mendonca T M, Wenander F, Penescu L, Orecchia R, Parodi K, Ferrari A and Stora T 2016 New developments of 11C post-accelerated beams for hadron therapy and imaging *Nucl. Instruments Methods Phys. Res. B* **376** 374–8

Battistoni G, Mattei I and Muraro S 2016 Nuclear physics and particle therapy **1** 661–86

Bauer J, Unholtz D, Sommerer F, Kurz C, Haberer T, Herfarth K, Welzel T, Combs S E, Debus J and Parodi K 2013 Implementation and initial clinical experience of offline PET/CT-based verification of scanned carbon ion treatment *Radiother. Oncol.* **107** 218–26

Bethe H 1930 Zur Theorie des Durchgangs schneller Korpuskularstrahlen durch Materie *Ann. Phys.* **397** 325–400

Bloch F 1933 Bremsvermögen von Atomen mit mehreren Elektronen *Zeitschrift für Phys.* **81** 363–76

Bom V, Joulaeizadeh L and Beekman F 2012 Real-time prompt gamma monitoring in spot-scanning proton therapy using imaging through a knife-edge-shaped slit *Phys. Med. Biol.* **57** 297–308

Chang D S, Lasley F D, Das I J, Mendonca M S, Dynlacht J R, Chang D S, Lasley F D, Das I J, Mendonca M S and Dynlacht J R 2014 Oxygen Effect, Relative Biological Effectiveness and Linear Energy Transfer *Basic Radiotherapy Physics and Biology* (Springer International Publishing) pp 235–40

Chatterjee A, Alpen E L, Tobias C A, Llacer J and Alonso J 1981 HIGH ENERGY BEAMS OF

RADIOACTIVE NUCLEI AND THEIR BIOMEDICAL APPLICATIONS *Int. J. Radiat. Oncol. Biol. Phys.* **7** 503–7

Chi Y, Tian Z and Jia X 2016 Modeling parameterized geometry in GPU-based Monte Carlo particle transport simulation for radiotherapy *Phys. Med. Biol.* **61** 5851–67

Chuong M, Badiyan S N, Yam M, Li Z, Langen K, Regine W, Morris C, Snider J, Mehta M, Huh S, Rutenberg M, Nichols R C and Nichols R C 2018 Pencil beam scanning versus passively scattered proton therapy for unresectable pancreatic cancer. *J. Gastrointest. Oncol.* **9** 687–93

Cirrone G A P, Cuttone G, Di Rosa F, Mazzaglia S E, Romano F, Attili A, Bourhaleb F, Russo G, Kataniemi P, Heikkinen A, Marchetto F and Jungwook S 2009 Hadrontherapy: An open source, Geant4-based application for proton-ion therapy studies *IEEE Nuclear Science Symposium Conference Record* pp 4186–9

Connell P P and Hellman S 2009 Advances in radiotherapy and implications for the next century: A historical perspective *Cancer Res.* **69** 383–92

DANZKER M, KESSARIS N D and LAUGHLIN J S 1959 Absorbed dose and linear energy transfer in radiation experiments. *Radiology* **72** 51–61

Dudouet J, Cussol D, Durand D and Labalme M 2013 Benchmarking GEANT4 nuclear models for carbon-therapy at 95 MeV / A *Benchmarking*

Ebner D K and Kamada T 2016 The Emerging Role of Carbon-Ion Radiotherapy. *Front. Oncol.* **6** 140

Enghardt W, Debus J, Haberer T, Hasch B G, Hinz R, Jgkel O, Krgmer M, Lauckner K, Pawelke J and Phnisch F 1999 *Positron emission tomography for quality assurance of cancer therapy with light ion beams* vol 654

Fano U 1963 Penetration of Protons, Alpha Particles, and Mesons *Annu. Rev. Nucl. Sci.* **13** 1–66

Ferrero V, Fiorina E, Morrocchi M, Pennazio F, Baroni G, Battistoni G, Belcari N, Ciocca M, Del Guerra A, Donetti M, Giordanengo S, Giraudo G, Patera V, Peroni C, Rivetti A, Dionisio da Rocha Rolo M, Rossi S, Rosso V, Sportelli G, Tampellini S, Valvo F, Wheadon R, Cerello P, Giuseppina Bisogni M, di Roma S, Veronica Ferrero I, Camarlinghi N N, Ciocca M, Del Guerra A, Donetti M, Giordanengo S, Giraudo G, Patera V, Peroni C, Rivetti A, Rolo M D da R, Rossi S, Rosso V, Sportelli G, Tampellini S, Valvo F, Wheadon R, Cerello P and Bisogni M G 2018 Online proton therapy monitoring: clinical test of a Silicon-photodetector-based in-beam PET *Sci. Rep.* **8** 4100

Le Foulher F, Bajard M, Chevallier M, Dauvergne D, Freud N, Henriquet P, Karkar S, Letang J M, Lestand L, Plescak R, Ray C, Schardt D, Testa E and Testa M 2010 Monte Carlo Simulations of Prompt-Gamma *IEEE Trans. Nucl. Sci.* **57** 2768–72

Geant4 Collaboration 2017 *Guide for physics list*

Hendry J H 2005 Protective Effects on Microorganisms in Radiation Sterilised Tissues *Sterilisation of Tissues Using Ionising Radiations* (Elsevier Inc.) pp 331–8

Highland V L 1975 Some practical remarks on multiple scattering *Nucl. Instruments Methods* **129** 497–9

Jakel O 2006 Heavy Ion Radiotherapy *New Technologies in Radiation Oncology* pp 365–77

Jongen Y and Stichelbaut F 2003 39th PTCOG meeting San Francisco, California, USA *Verification of the proton beam position in the patient by the prompt gamma rays emission.* (San Franscico)

Kanai T, Endo M, Minohara S, Miyahara N, Koyama-Ito H, Tomura H, Matsufuji N, Futami Y, Fukumura A, Hiraoka T, Furusawa Y, Ando K, Suzuki M, Soga F and Kawachi K 1999 *BIOPHYSICAL CHARACTERISTICS OF HIMAC CLINICAL IRRADIATION SYSTEM FOR*

HEAVY-ION RADIATION THERAPY

Kanazawa M, Kitagawa A, Kouda S, Nishio T, Torikoshi M, Noda K, Murakami T, Suda M, Tomitani T, Kanai T, Futami Y, Shinbo M, Urakabe E and Iseki Y 2002 Application of an RI-beam for cancer therapy: In-vivo verification of the ion-beam range by means of positron imaging *Nucl. Phys. A*

Karger C P, Jäkel O, Palmans H and Kanai T 2010 Dosimetry for ion beam radiotherapy *Phys. Med. Biol.* **55** R193–234

Kitagawa A, Furusawa Y, Kanai T, Kanazawa M, Mizuno H, Muramatsu M, Sato S, Suda M, Tomitani T, Urakabe E, Yoshimoto M, Li Q, Wei Z, Hanawa K, Iseki Y and Sato K 2006 Medical application of radioactive nuclear beams at HIMAC *Rev. Sci. Instrum.* **77**

Kraan A C 2015 Range Verification Methods in Particle Therapy: Underlying Physics and Monte Carlo Modeling. *Front. Oncol.* **5** 150

Krimmer J, Dauvergne D, Létang J M M and Testa É 2018 Prompt-gamma monitoring in hadrontherapy: A review *Nucl. Instruments Methods Phys. Res. Sect. A Accel. Spectrometers, Detect. Assoc. Equip.* **878** 58–73

Maccabee H D, Madhvanath U and Raju M R 1969 Tissue activation studies with alpha-particle beams. *Phys. Med. Biol.* **14** 213–24

Mackin D, Peterson S, Beddar S and Polf J C 2012 Evaluation of a stochastic reconstruction algorithm for use in Compton camera imaging and beam range verification from secondary gamma emission during proton therapy *Phys. Med. Biol.* **57** 3537–3353

Marion J B 1974 THE EFFECTS OF NUCLEAR RADIATIONS *Energy in Perspective* (Elsevier) pp 140–69

Min C H, Kim C H, Youn M Y and Kim J W 2006 Prompt gamma measurements for locating the

dose falloff region in the proton therapy *Appl. Phys. Lett.* **89**

Minhoara S, Fukuda S, Kanematsu N, Takei Y, Furukawa T, Inaniwa T, Matsufuji N, Mori S and Noda K 2010 Recent Innovations in Carbon-Ion Radiotherapy *J. Radiat. Res.* **51** 385–92

Minohara S, Fukuda S, Kanematsu N, Takei Y, Furukawa T, Inaniwa T, Matsufuji N, Mori S and Noda K 2010 Recent Innovations in Carbon-Ion Radiotherapy *J. Radiat. Res* **51** 385–92

Mohamad O, Makishima H and Kamada T 2018 Evolution of Carbon Ion Radiotherapy at the National Institute of Radiological Sciences in Japan. *Cancers (Basel).* **10**

Mohamad O, Sishc B J, Saha J, Pompos A, Rahimi A, Story M D, Davis A J and Kim D W N 2017 Carbon ion radiotherapy: A review of clinical experiences and preclinical research, with an emphasis on DNA damage/repair *Cancers (Basel).* **9** 1–30

Mohammadi A, Tashima H, Iwao Y, Takyu S, Akamatsu G, Nishikido F, Yoshida E, Kitagawa A, Parodi K and Yamaya T 2019 Range verification of radioactive ion beams of ^{11}C and ^{15}O using in-beam PET imaging *Phys. Med. Biol.* **64** 145014

Moore. C S, Wood. T J, Avery G, Balcam S, Needler L, Smith A, Saunderson J R and Beavis A W 2015 Investigating the use of an anti-scatter grid in digital CR chest radiography *Hull East York Hosp. NHS Trust* **86** 1–7

Newhauser W D and Zhang R 2015 The physics of proton therapy. *Phys. Med. Biol.* **60** R155--209

Nie W, Jones K C, Petro S, Kassaee A, Sehgal C M and Avery S 2018 Proton range verification in homogeneous materials through acoustic measurements *Phys. Med. Biol.* **63**

Paganetti H 2012 Range uncertainties in proton therapy and the role of Monte Carlo simulations. *Phys. Med. Biol.* **57** R99--117

Palta J R 2014 53rd PTCOG meeting Shanghai, China *Understanding the Uncertainties in Proton*

Therapy (Shanghai)

Park J H, Kim S H, Ku Y, Kim C H, Lee H R, Jeong J H, Lee S B and Shin D H 2019 Multi-slit prompt-gamma camera for locating of distal dose falloff in proton therapy *Nucl. Eng. Technol.* **51** 1406–16

Park S H and Kang J O 2011 Basics of particle therapy I: physics *Radiat. Oncol. J.* **29** 135

Parodi K 2016 On- and off-line monitoring of ion beam treatment *Nucl. Instruments Methods Phys. Res. Sect. A Accel. Spectrometers, Detect. Assoc. Equip.* **809** 113–9

Parodi K, Bortfeld T, Enghardt W, Fiedler F, Knopf A, Paganetti H, Pawelke J, Shakirin G and Shih H 2008 PET imaging for treatment verification of ion therapy: Implementation and experience at GSI Darmstadt and MGH Boston *Nucl. Instruments Methods Phys. Res. Sect. A Accel. Spectrometers, Detect. Assoc. Equip.* **591** 282–6

Parodi K, Paganetti H, Shih H A, Michaud S, Loeffler J S, DeLaney T F, Liebsch N J, Munzenrider J E, Fischman A J, Knopf A and Bortfeld T 2007 Patient study of in vivo verification of beam delivery and range, using positron emission tomography and computed tomography imaging after proton therapy. *Int. J. Radiat. Oncol. Biol. Phys.* **68** 920–34

Parodi K and Polf J C 2018 In vivo range verification in particle therapy *Med. Phys.* **45** e1036–50

Phillips G W 1995 Gamma-ray imaging with Compton cameras *Nucl. Inst. Methods Phys. Res. B* **99** 674–7

Pinto M, Bajard M, Brons S, Chevallier M, Dauvergne D, Dedes G, De Rydt M, Freud N, Krimmer J, La Tessa C, Lï¿½tang J M, Parodi K, Pleskač R, Prieels D, Ray C, Rinaldi I, Roellinghoff F, Schardt D, Testa E and Testa M 2015 Absolute prompt-gamma yield measurements for ion beam therapy monitoring *Phys. Med. Biol.* **60** 565–94

Pinto M, Dauvergne D, Freud N, Krimmer J, Letang J M, Ray C, Roellinghoff F and Testa E 2014

Design optimisation of a TOF-based collimated camera prototype for online hadrontherapy monitoring *Phys. Med. Biol.* **59** 7653–74

Pshenichnov I, Larionov A and Mishustin I 2006 Distributions of positron-emitting nuclei in proton and carbon-ion therapy studied with GEANT4 Related content PET monitoring with 3He beams *Phys. Med. Biol.*

PTCOG 2020 PTCOG - Facilities in Operation Online: https://www.ptcog.ch/index.php/facilities-in-operation

Richter C, Pausch G, Barczyk S, Priegnitz M, Keitz I, Thiele J, Smeets J, Stappen F Vander, Bombelli L, Fiorini C, Hotoiu L, Perali I, Prieels D, Enghardt W and Baumann M 2016 First clinical application of a prompt gamma based in vivo proton range verification system *Radiother. Oncol.*

Roellinghoff F, Benilov A, Dauvergne D, Dedes G, Freud N, Janssens G, Krimmer J, Létang J M, Pinto M, Prieels D, Ray C, Smeets J, Stichelbaut F and Testa E 2014 Real-time proton beam range monitoring by means of prompt-gamma detection with a collimated camera *Phys. Med. Biol.* **59** 1327–38

Schardt D, Elsässer T and Schulz-Ertner D 2010 Heavy-ion tumor therapy: Physical and radiobiological benefits

Smeets J, Roellinghoff F, Prieels D, Stichelbaut F, Benilov A, Busca P, Fiorini C, Peloso R, Basilavecchia M, Frizzi T, Dehaes J C and Dubus A 2012 Prompt gamma imaging with a slit camera for real-time range control in proton therapy *Phys. Med. Biol.* **57** 3371–405

Solevi P, Muñoz E, Solaz C, Trovato M, Dendooven P, Gillam J E, Lacasta C, Oliver J F, Rafecas M, Torres-Espallardo I and Llosá G 2016 Performance of MACACO Compton telescope for ion-beam therapy monitoring: First test with proton beams *Phys. Med. Biol.*

Testa E, Bajard M, Chevallier M, Dauvergne D, Le Foulher F, Freud N, Létang J M M, Poizat J C C, Ray C, Testa M, Dauvergne D, Bajard M, Poizat J C C, Chevallier M, Létang J M M, Testa E, Le Foulher F, Ray C, Bajard M, Chevallier M, Dauvergne D, Le Foulher F, Freud N, Létang J M M, Poizat J C C, Ray C and Testa M 2009 Dose profile monitoring with carbon ions by means of prompt-gamma measurements *Nucl. Instruments Methods Phys. Res. Sect. B Beam Interact. with Mater. Atoms* **267** 993–6

Testa E, Bajard M, Chevallier M, Dauvergne D, Le Foulher F, Freud N, Ĺtang J M, Poizat J C, Ray C and Testa M 2008 Monitoring the Bragg peak location of 73 MeVu carbon ions by means of prompt γ -ray measurements *Appl. Phys. Lett.*

Testa M 2010 *Physical measurements for ion range verification in charged particle therapy* (Lyon: DE L'UNIVERSITE DE LYON)

Tobias C A, Benton E V., Capp M P, Chatarjee A, Cruty M R and Henke R P 1977 PARTICLE RADIOGRAPHY AND AUTOACTIVATION *Int. J. Radiat. Oncol. Biol. Phys.* **3** 35–44

Tsuboi K 2020 Early History of Biology and Clinical Application of Proton Beam Therapy *Proton Beam Radiotherapy* (Springer Singapore) pp 9–21

Tsujii H and Kamada T 2012 A Review of Update Clinical Results of Carbon Ion Radiotherapy *Jpn. J. Clin. Oncol.* **42**

Urakabe E, Kanai T, Kanazawa M, Kitagawa A, Noda K, Tomitani T, Suda M, Iseki Y, Hanawa K, Sato K, Shimbo M, Mizuno H, HIRATA Y, Futami Y, Iwashita Y and Noda A 2001 Spot Scanning Using Radioactive 11 C Beams for Heavy-Ion Radiotherapy *Jpn. J. Appl. Phys* **40** 2540–8

Wilson R R 1946 Radiological use of fast protons. *Radiology* **47** 487–91

Xie Y, Bentefour E H, Janssens G, Smeets J, Vander Stappen F, Hotoiu L, Yin L, Dolney D, Avery

S, O'Grady F, Prieels D, McDonough J, Solberg T D, Lustig R A, Lin A and Teo B-K K 2017 Prompt Gamma Imaging for In Vivo Range Verification of Pencil Beam Scanning Proton Therapy *Int. J. Radiat. Oncol.* **99** 210–8

Yan Y-L, Liu X-G, Dai Z-Y, Ma Y-Y, He P-B, Shen G-S, Ji T-F, Zhang H and Li Q 2017 Spot-scanning beam delivery with laterally- and longitudinally-mixed spot size pencil beams in heavy ion radiotherapy *Chinese Phys. C* **41** 98201

Zarifi M, Guatelli S, Qi Y, Bolst D, Prokopovich D and Rosenfeld A 2019 Characterization of prompt gamma ray emission for in vivo range verification in particle therapy: A simulation study *Phys. Medica* **62** 20–32

Zheng Y, Kang Y, Zeidan O and Schreuder N 2016 An end-to-end assessment of range uncertainty in proton therapy using animal tissues *Phys. Med. Biol.* **61** 8010–24

Zhu X, España S, Daartz J, Liebsch N, Ouyang J, Paganetti H, Bortfeld T R and El Fakhri G 2011 Monitoring proton radiation therapy with in-room PET imaging *Phys. Med. Biol.* **56** 4041–57

Ziegler J F, Ziegler M D and Biersack J P 2010 SRIM - The stopping and range of ions in matter (2010) *Nucl. Instruments Methods Phys. Res. Sect. B Beam Interact. with Mater. Atoms* **268** 1818–23

CHAPTER 3: PROMPT GAMMA IMAGING THROUGH MECHANICAL MULTI SLIT COLLIMATOR FOR CARBON ION THERAPY

Ananta Raj Chalise[1], Yujie Chi[1], Yiping Shao[2], Mingwu Jin[1]

1 Physics, University of Texas at Arlington, Arlington, TX 76051, USA

2 Radiation Oncology, University of Texas Southwestern Medical Center, Dallas, TX 75390, USA

E-mail: mingwu@uta.edu

(Manuscript to be submitted in Physics in Medicine and Biology)

Abstract

Despite its high dose conformity, particle therapy has not been fully exploited owing to limitations in dose verification technique. Secondary radiation generated during the treatment which were found to have correlation with the beam range have currently been used to verify the range. For online and real-time verification, prompt gammas that are generated due to deexcitation of excited nuclei during the nuclear interaction are one of the best candidates. Multi-slit camera which relies on the mechanical collimation of the gamma has advantage of large field of view to cover the beam profile as much as possible. Five parameters, height of collimator, slit and slab width, distance of collimator and detector from beam axis, have been optimized in terms different performance metrics, including signal to background ratio (SBR), spatial resolution, sensitivity, peak to secondary peak and slab to slit peak ratio. No common optimal setup was found for all metrics and hence there must be some trade-off between them depending on the circumstance. If good SBR, sensitivity and slab to slit peak ratio are desired, the preferred configuration of multi-slit camera is large slit width, small slab width, 150 mm collimator height, and 0.5 m of distance from beam axis to detector. However, if peak to secondary peak ratio is to optimize, a better choice is small slit width and large slab width and slightly more than 0.5 of distance from beam axis to detector.

3.1 Introduction

Compared to conventional radiation therapy techniques, particle therapy provides high conformity of the dose along with higher radiobiological effectiveness (Schardt *et al* 2010). However, it has not been fully exploited due to the limitations in treatment delivery verification techniques (Solevi *et al* 2016). In order to use the full potential of particle therapy, we would need to be able to locate the stopping positions of ions in tissue, ideally in three-dimensional space, online and in real-time *in vivo* (Parodi 2016). In contrast to conventional therapy methods, the particles in particle therapy stop within the patient body, and hence transmittance information is not available for range verification purposes. Secondary gammas emitted due to nuclear reaction during the treatment have been explored as possible solutions to this problem. Currently positron emission tomography (PET) has been extensively investigated to track the annihilation gammas produced during the treatment for in-room or post-treatment range verification. Use of PET, however, has the limitation of half-lives of positron emitting nuclei and may be challenging for online and real time range verification. Lately, prompt gammas generated during the deexcitation of excited nuclei have been pursued as possible online and quasi real-time range monitoring (Parodi 2016). In this work, we will focus on prompt gamma imaging (PGI).

In regard to PGI, currently there are two main avenues being pursued, namely electronic collimation and passive/mechanical collimation (Pinto *et al* 2014). Both of these techniques detect these gammas in orthogonal to the beam direction aiming to maximize the correlation between gamma photons and the ion beam path. Compton cameras are based on electronic collimation (Phillips 1995, Mackin *et al* 2012), while knife-edged slit cameras (Bom *et al* 2012, Smeets *et al* 2012) and multi-slit cameras (Roellinghoff *et al* 2014, Bom *et al* 2012) are based on mechanical collimation. Although the knife-edged slit camera has been trialed in clinic, it has to trade-off

between the spatial resolution and field of view (FOV) (Park *et al* 2019). On the other hand, multi-slit cameras can cover a large FOV without sacrificing the spatial resolution, which is a good candidate for range verification by locating PG distal fall-off.

In this paper, we studied different parameters of multi-slit camera and evaluated their performance on signal-to-background ratio, spatial resolution using full width half maximum (FWHM), sensitivity, peak-to-second peak ratio, and slab-to-slit ratio. The camera parameters we explored include the height of the collimator, slab and slit width, distance of collimator from the beam line and distance of detector from the beamline. The comparison with a previous study (Pinto *et al* 2014) was also conducted.

3.2 Methods and Methodologies

We used the Geant4 Monte Carlo simulation package (Agostinelli *et al* 2003) to investigate the prompt gamma imaging (PGI) performance of mechanical collimation for carbon ion therapy. We implemented two different approaches for this purpose. First, we did simplistic approach to speed up the simulation, we used an isotropic gamma source limited to first and second quadrant and recorded gamma photons in the detector after passing through the collimator. This enabled us to perform the massive simulations quicker by skipping the computationally demanding simulations of heavy particle transport and interaction in matter. Second, we used carbon ions to generate the PG in the water phantom, and evaluate the best setups obtained by the isotropic source.

3.2.1 Isotropic gamma source

This experiment was designed in order to reduce the computational time for massive simulations with different camera settings. The experiment design is explained in the following sections.

3.2.1.1 Simulation setup

The setup for this simulation is shown in figure 3.3.1. We placed our gamma source in an air phantom of dimension 50 cm × 5 cm × 5 cm and constructed an ideal detector of same dimension. This detector was placed at variable distances from the source. And in between the air-phantom and the detector, there were multi-slit collimators with different parameters, including height and thickness.

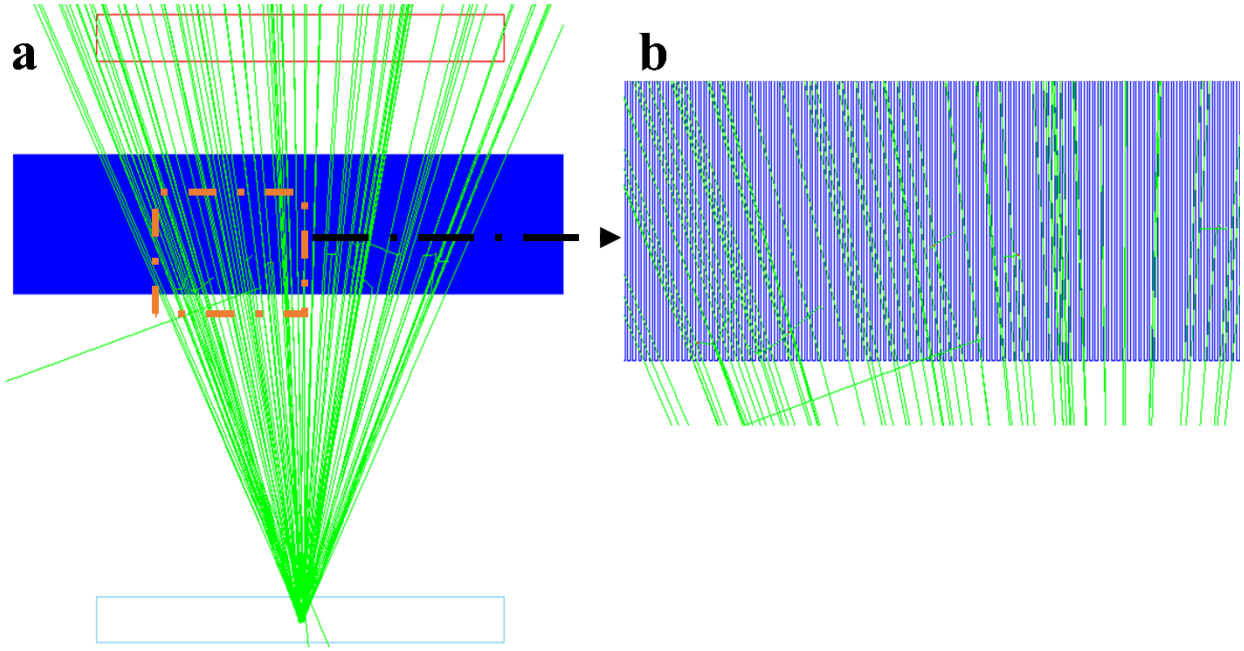

Figure 11.1 (a) Simulation setup showing the source containing air phantom (sky-blue), multi-slit collimator (dark blue) and detector (red) along with the distribution of gamma (green) (b) the magnified view of the orange block in figure (a) for detailed structure of the multi-slit collimator.

3.2.1.2 Source distribution

We simulated a gamma source distributed as a 4-mm radius semi-circle centered at positive 1 mm of x-axis. The energy of these gammas has a linear distribution ranging from 2 MeV to 7 MeV (figure 3.2a), which is typical for prompt gamma. The direction of them are limited to first

and second quadrant as shown in figure 3.2b in order to substantially improve the simulation efficiency.

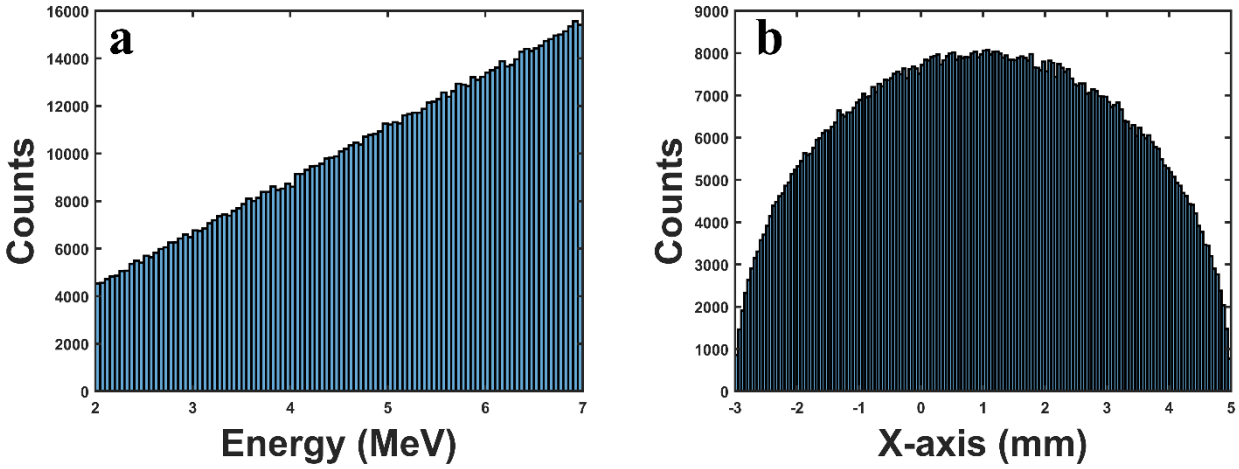

Figure 3.12: Energy distribution (a) and x- axis distribution (b) of gamma source defined for our simulations

3.2.1.3 Parameters explored and their ranges

Five different parameters of the multi-slit camera were explored in our simulation accounting for a total of 4752 simulations. They are slit and slab width, collimator height, distance from the beam axis (the source) to collimator front face and distance from the beam axis (the source) to detector front face. The definitions of these parameters are shown in figure 3.3.

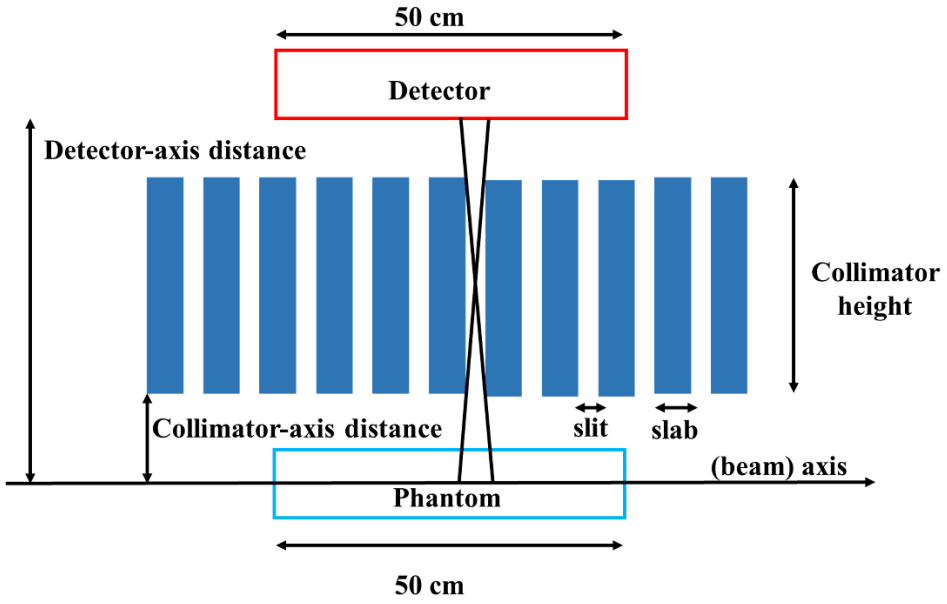

Figure 13: Five parameters of multi-slit collimator explored in our simulations (not to scale): slit and slab width, collimator height, distance from the beam axis to collimator front face and distance from the beam axis to detector front face.

The ranges of these parameters explored are tabulated in the table 3.1.

Table 3.2: Parameters and ranges considered for optimization

Geometrical Parameter	Ranges (mm)	Number of simulations
Slit width	1-6 (1 interval)	6
Slab width	1-6 (1 interval)	6
Collimator thickness/height	150-300 (50 interval)	4
Distance from beam axis to collimator front face	300-800 (50 mm interval)	11
Distance from beam axis to detector front face	500-650 (50 mm interval)	3
		4752

3.2.2 Simulation with carbon ion in Water phantom

After we ranked the collimator design based on their performance with respect to SBR, sensitivity, slab to slit ratio and peak to second peak, we performed simulation with carbon ions

irradiation in water phantom for all the top cases. For this experiment, we changed our phantom to Water from air phantom in Figure 3.1(a) and irradiated 95 MeV/u C-12 ions at 3 mm from the left surface of the phantom. Two million carbon ions were simulated for this case. Prompt gammas generated and passed through the multi-slit collimator was recorded in the detector.

3.2.3 Data processing

All the data were recorded in the ideal detector of 50 cm × 5 cm × 5 cm and then processed using MATLAB based on the camera configurations as detailed in the following subsection.

3.2.3.1 Processing of isotropic gamma source

We performed 4752 simulations. The gammas detected on the detector were binned by the opening in the slit to produce a plot with counts vs the positions in x-axis. Because of the large quantity of simulations, visually inspection of each individual simulation was very time consuming. Thus, we took several factors into account to compare all of our simulations. The five metrics, signal-to-background ratio (SBR), sensitivity, spatial resolution, peak-to-second-peak ratio and slab-to-slit ratio, are defined as follows. SBR is the ratio of counts at the center of the slit with the counts at the center of the slab. Spatial resolution is measured by full-width-half-maximum (FWHM) of gamma peak is measured by the width of the primary peak at its half maxima. Sensitivity (Sensit.) is measured by the ratio of counts of detector to the source count over five central slits. Peak-to-second-peak ratio (P2SPe) is the ratio between the highest peak in the gamma profile to the average of second highest peak on either side of central slits of detector. Finally, slab-to-slit ratio (Slb2Slt) is defined as ratio of counts of maximum slab to average of counts in slit on either side of the maximum count slab. It helps to quantify the transmission as

well as cross talk. For SBR, sensitivity and P2SPe, the larger the better. For FWHM and Slb2Slt, the smaller the better.

3.2.3.2 Processing of carbon ion in water phantom simulation

After analyzing the results using the isotropic gamma source, a more comprehensive simulation was performed to include the carbon ions impinging in the water phantom for all top cases. The gamma recorded were then processed like above method.

3.3 Results

3.3.1 Results for some optimal designs in a previous work

The multi-slit cameras were studied previously for proton therapy (Pinto *et al* 2014). We adapted their recommended optimal designs and evaluated their performance on five metrics as listed in Table 3.2. The major difference of two designs is the slit width. With larger slit width (Case 1), the SBR and sensitivity are good at the expense of FWHM, P2SP3, and Slb2Slt. In contrast, the smaller slit width leads to better spatial resolution at the lower sensitivity. The gamma profiles of two designs are shown in figure 3.4. The second design yields the shaper peak than the first design but suffers more noise.

Table 3.3: Details of Pinto's experiment along with SBR, full width half maximum, sensitivity, peak to secondary peak and slab to slit ratio (CollaxD: the distance from the beam axis to collimator front face, DetaxD: the distance from the beam axis to Detector front face)

Case	Slit	Slab	Thickness	CollaxD	DetaxD	SBR	FWHM	Sensit.	P2SPe	Slb2Slt
1	5.4	2.6	180.2	303.7	485.3	3.26	14	0.0056	1.71	0.70
3	3.0	2.1	190.9	322.3	516.5	2.22	8	0.0017	2.47	0.50

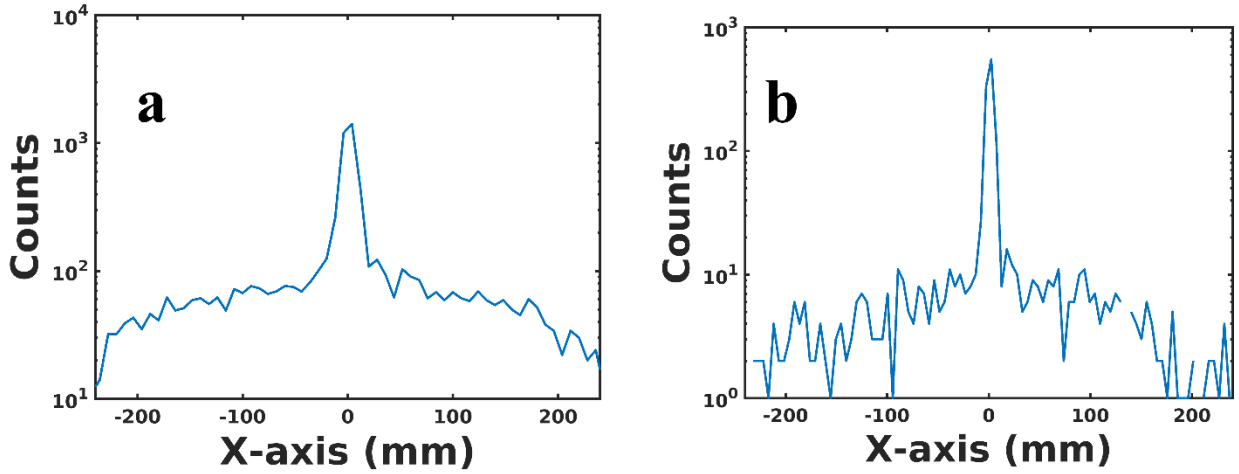

Figure 14 : Gamma distribution along the beam axis (x) based on configurations in (Pinto et al 2014): (a) Case I in Table 3.2 and (b) Case III

3.3.2 Optimized results for isotropic gamma source experiment

In the following subsections, we listed top 10 results for each metric and their corresponding values for the other metrics.

3.3.2.1 Signal to background ratio (SBR)

The top ten highest SBR cases are tabulated in table 3.3. The SBR seems to favor large slit width (4-6 mm) and small slab width (1 mm). The 6-mm slit width and 1-mm slab width yield SBR values more than 5 with the sensitivity at the order of 10^{-3}. However, the FWHM is generally greater than 12 mm. The corresponding gamma distributions for the top 4 ranked SBR configurations in x are shown in Figure 3.5.

Table 4 : Top ten results for highest SBR

Case	Slit	Slab	Thickness	CollaxD	DetaxD	SBR	FWHM	Sensit.	P2SPe	Slb2slt
I	6	1	150	350	550	5.64	18	0.0041	1.94	3.5
II	6	1	150	350	600	5.63	22	0.0037	2.12	3.05
III	6	1	150	400	600	5.53	16	0.0035	1.81	3.08
IV	6	1	200	350	600	5.32	12	0.0030	2.37	3.44
V	5	1	150	350	600	4.76	15	0.0029	1.78	4.49
VI	5	1	150	400	600	4.64	15	0.0029	1.61	4.19
VII	5	1	200	350	600	4.57	13	0.0023	2.00	0.47
VIII	5	1	150	350	550	4.57	14	0.0033	1.69	4.56
IX	4	1	150	350	600	4.31	12	0.0025	2.14	0.45
X	4	1	150	350	550	4.02	11	0.0027	2.008	0.54

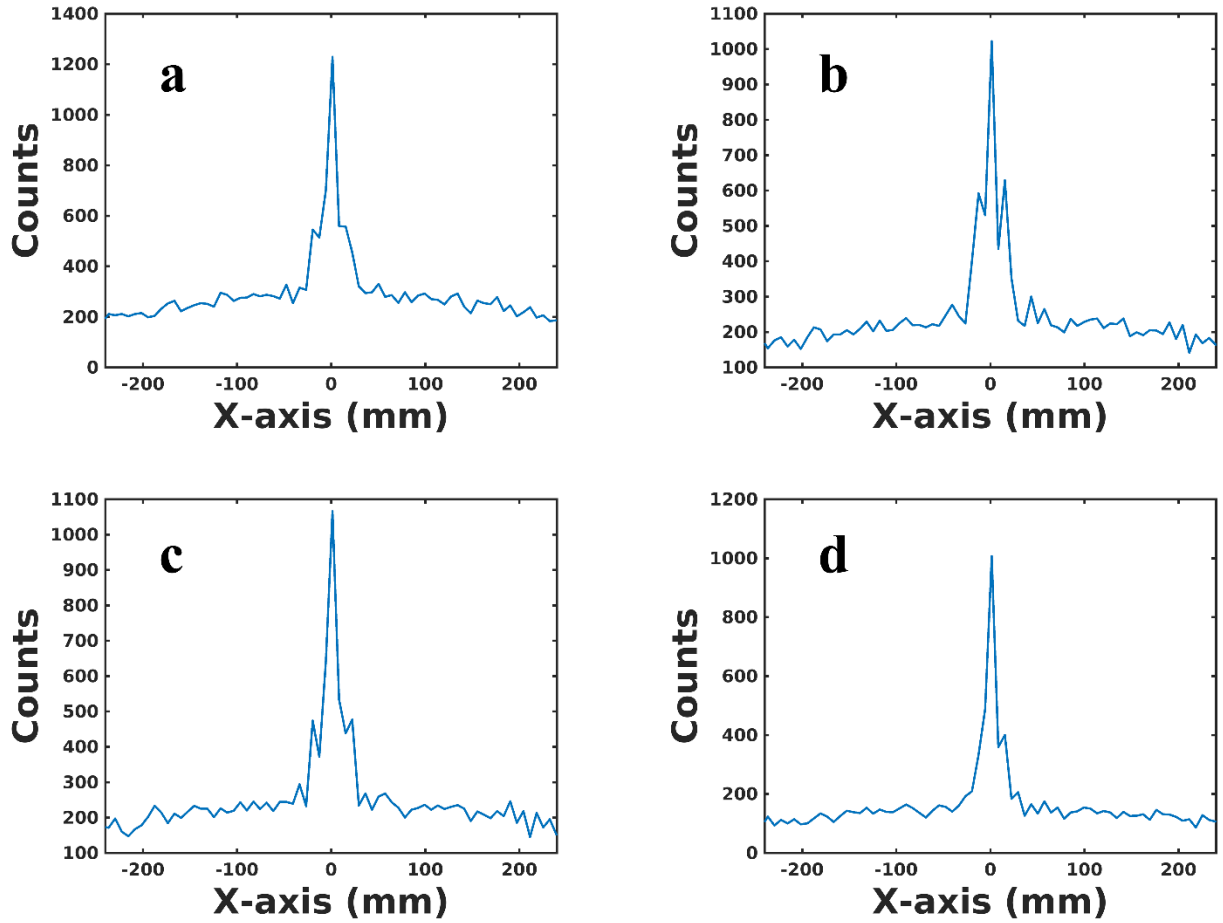

Figure 15 The gamma distribution for top 4 cases optimized for SBR (a) through (d) corresponding to cases I to IV in Table 3.3 respectively.

3.3.2.2 Sensitivity

The top ten highest sensitivity cases are tabulated in table 3.4, which are greater than $3x10^{-3}$. In order to get good sensitivity, the large slit width (9 6-mm slit widths and 1 5-mm slit width) is in need. The SBR seems to favor large slit width and small slab width. Note that Case XI is coincident with Case I for 6-mm slit and 1-mm slab. Again, the low spatial resolution is observed (FWHM > 14 mm). The corresponding gamma distributions for the top 4 ranked sensitivity configurations in x are shown in Figure 3.6.

Table 3.4: Top ten results for highest sensitivity

Case	Slit	Slab	Thickness	CollaxD	DetaxD	Sensit.	FWHM	SBR	P2SPe	Slb2slt
XI	6	1	150	350	550	0.0041	18	5.64	1.94	3.5
XII	6	2	150	350	550	0.0039	16	2.96	2.12	0.72
XIII	6	3	150	350	550	0.0037	15	1.97	3.08	1.46
XIV	6	1	150	350	600	0.0037	22	5.63	2.12	3.05
XV	6	2	150	350	600	0.0036	18	3.13	2.14	0.70
XVI	6	1	150	400	600	0.0035	16	5.53	1.81	3.08
XVII	6	2	150	400	600	0.0034	17	3.02	1.94	0.68
XVIII	6	3	150	350	600	0.0034	14	2.02	3.47	1.40
XIX	5	1	150	350	550	0.0033	14	4.57	1.69	4.56
XX	6	3	150	400	600	0.0031	16	1.85	2.67	1.25

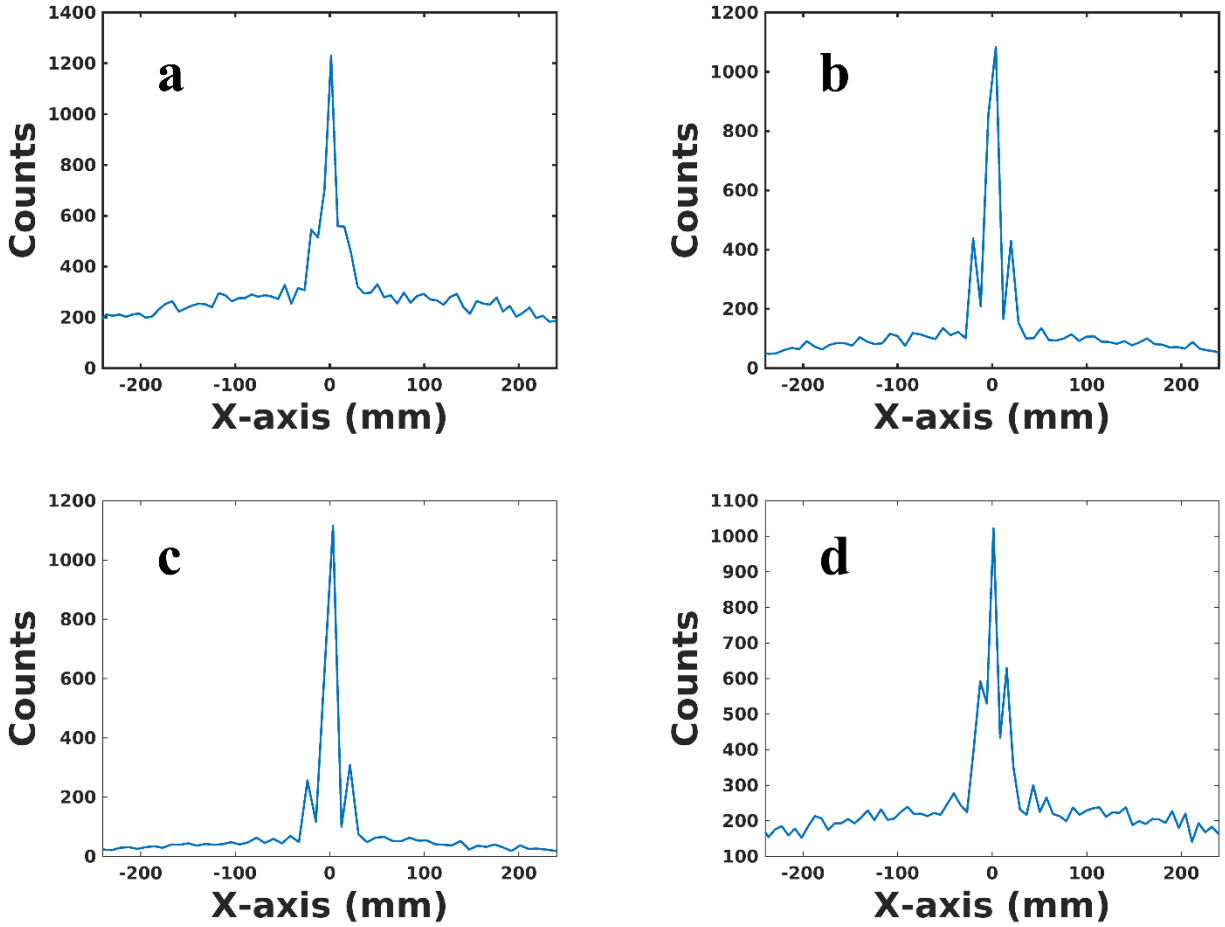

Figure 16: The gamma distribution for top 4 cases optimized for sensitivity. (a) through (d) corresponding to cases XI to XIV in Table 3.4

3.3.2.3 Peak-to-second peak ratio and FWHM

Since the peak-to-second peak ratio and FWHM reflect the similar performance of the multi-slit camera, i.e. the sharpness of the primary peak, we only ranked the peak-to-second peak ratio for conciseness. The top ten cases of highest peak-to-second peak ratios are tabulated in table 3.5, which range from tens to a couple of hundreds. The corresponding spatial resolution is considerably better than previous 20 cases with FWHM from 6 mm to 12 mm. However, the SBR and sensitivity suffer in these cases, where the former is usually less than 1 and the latter is in the order of 10^{-4}. The corresponding gamma distributions for the top 4 ranked peak-to-peak

configurations in x are shown in Figure 3.7. Compared to Figure 3.5 and 3.6, the primary peak is sharp, and the side lobes are gone.

Table 3.5: Top ten results for highest peak-to-secondary peak ratio

Case	Slit	Slab	Thickness	CollaxD	DetaxD	P2SPe	FWHM	SBR	Sensit.	Slb2slt
XXI	2	5	200	350	600	188	12	0.86	6.1e-4	0.78
XXII	2	5	150	350	600	126.67	7	0.56	6.3e-4	1.26
XXIII	2	5	150	350	550	60.5	7	0.68	8.1e-4	0.98
XXIV	4	1	200	350	600	29.33	10	0.70	0.0012	18
XXV	2	5	150	400	600	23.33	8	0.62	7.4e-4	0.79
XXVI	3	4	150	600	350	22.05	8	0.73	0.001	8.89
XXVII	3	4	200	350	600	21.42	8	1.17	9.6e-4	0.53
XXVIII	1	4	150	350	550	16	6	0.49	4.5e-4	1
XXIX	3	1	200	350	600	14.51	9	0.55	9.5e-4	1.69
XXX	5	5	200	350	600	13.80	11	1.15	0.0014	6.21

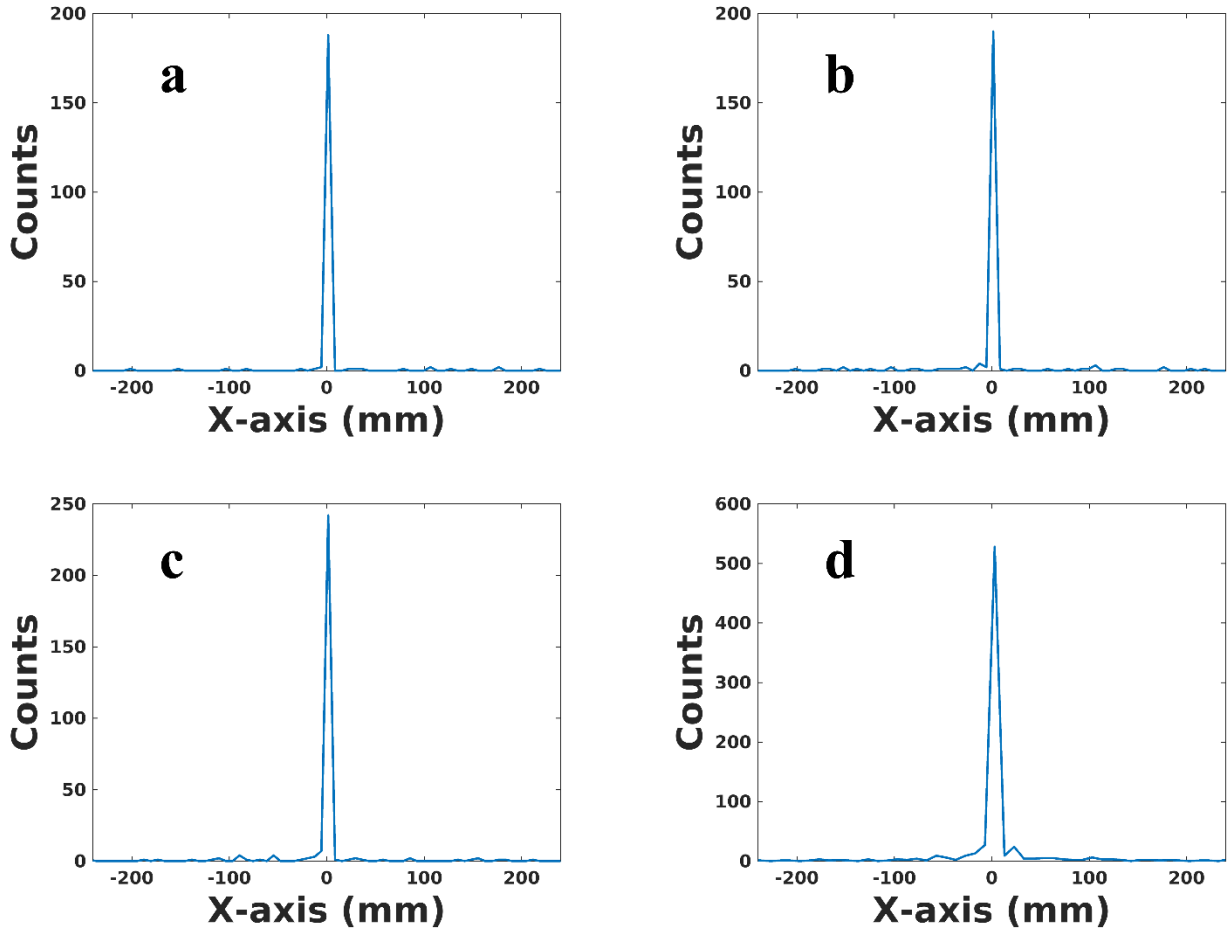

Figure 17: The gamma distribution for top 4 cases optimized for peak-to-secondary peak ratio. (a) through (d) representing cases XXI to XXIV in table 3.5.

3.3.2.4 Slab-to-slit ratio (Slb2Sli)

The top ten cases for smallest slab-to-slit ratio are tabulated in table 6. which range 0.45~0.64. The medium slit width (2-5 mm) and the small slab width (1 mm) seem to be preferred for this metric. The spatial resolution is also in the middle range (8-13 mm FWHM). The SBR is generally good and the sensitivity at the lower end of 10^{-3} level. The corresponding gamma distributions for the top 4 ranked Slb2Sli configurations in x are shown in Figure 3.8, which has a mixed presentation of Figure 3.5-3.7.

Table 3.6: Top ten results for smallest slab-to-slit ratio

Case	Slit	Slab	Thickness	CollaxD	DetaxD	Slb2Slt	FWHM	SBR	Sensit.	P2SPe
XXXI	4	1	150	350	600	0.45	12	4.31	0.0025	0.78
XXXII	5	1	200	350	600	0.47	13	4.57	0.0023	1.26
XXXIII	3	4	200	350	660	0.53	8	1.17	9.6e-4	0.98
XXXIV	4	1	150	350	550	0.54	11	4.02	0.0027	18
XXXV	3	1	150	350	600	0.55	11	3.08	0.0017	0.79
XXXVI	2	1	150	350	600	0.56	10	1.92	9.0e-4	8.89
XXXVII	4	1	150	400	600	0.58	10	3.97	0.0023	0.53
XXXVIII	3	1	150	350	550	0.61	9	2.95	0.0018	1
XXXIX	4	1	200	350	600	0.63	9	3.87	0.0019	1.69
XL	3	1	150	400	600	0.64	9	2.93	0.0016	6.21

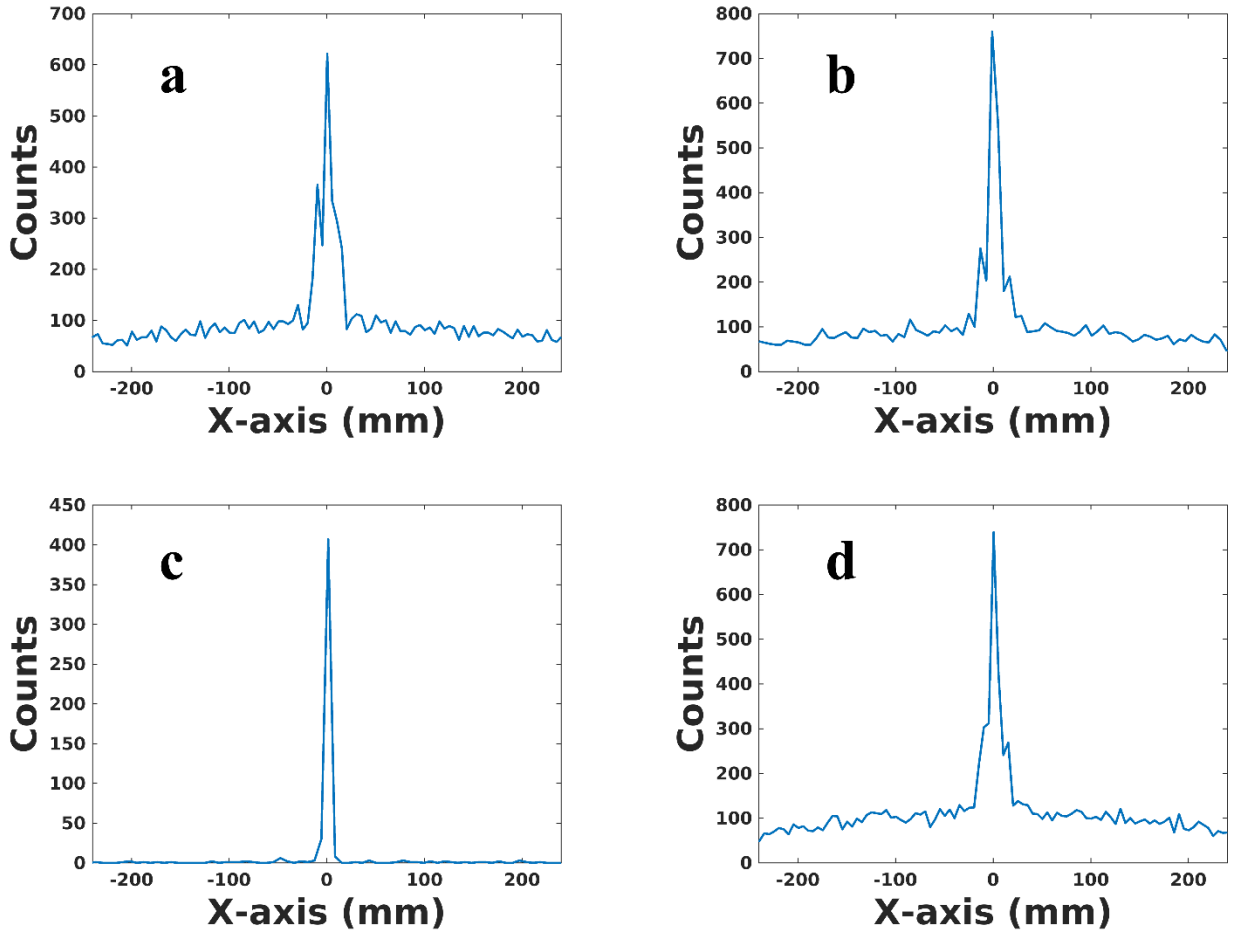

Figure 18: The gamma distribution for top 4 cases optimized for slab-to-slit ratio. (a) through (d) corresponding to cases XXXI to XXXIV in table 3.6

3.3.3 Results from carbon ions in water

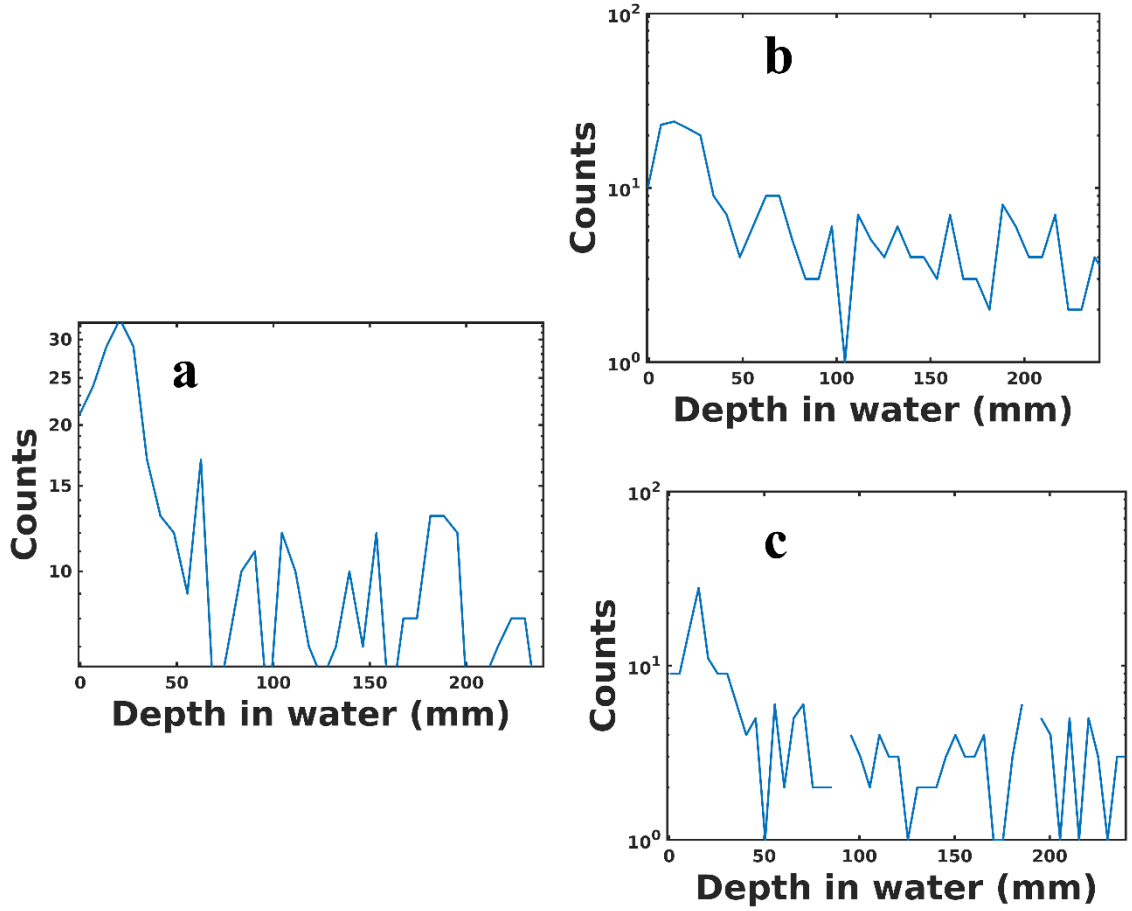

Figure 19: Prompt gamma distribution along the beam line using case I/ XI (a), XXI (b) and XXXI (c) configurations in tables 3.3-3.6 for 95 MeV/u C-12 ions irradiation on water phantom.

We selected the top one configuration for each metric and conducted PGI simulation for 95 MeV/u C-12 ions irradiation on a water phantom. The results of the longitudinal PG distribution are shown in figure 3.9. The sharp drop-off is easily observable for cases I/XI, whereas random fluctuations dominate in cases XXI and XXXI. From this observation, it seems that SBR and sensitivity are more important than other metrics for PGI for range verification.

3.4 Discussion and conclusion

The use of the isotropic gamma source greatly expedited the simulation process. We were able to accomplish 4,752 multi-slit collimator configurations in a short amount of time. Among these results, we saw some overlaps between the SBR and sensitivity and between peak-to-second peak ratio and FWHM, whereas the disparity largely exists in other metrics. In general, we would have to tradeoff these metrics. If higher SBR, sensitivity and lower slab-to-slit ratio are desired, the big slit width (5-6 mm) along with the small slab width (1-2 mm), 150 mm collimator height and 0.5 m distance of the beam line to detector are a good choice. For good spatial resolution, the small slit width is needed at the expense of low SBR and sensitivity. The follow-up carbon irradiation experiment indicated that the SBR/sensitivity seem to outweigh the other metrics to enable PGI-based range verification. Further studies will be needed to confirm these findings.

Reference

Agostinelli S, Allison J, Amako K, Apostolakis J, Araujo H, Arce P, Asai M, Axen D, Banerjee S, Barrand G, Behner F, Bellagamba L, Boudreau J, Broglia L, Brunengo A, Burkhardt H, Chauvie S, Chuma J, Chytracek R, Cooperman G, Cosmo G, Degtyarenko P, Dell'Acqua A, Depaola G, Dietrich D, Enami R, Feliciello A, Ferguson C, Fesefeldt H, Folger G, Foppiano F, Forti A, Garelli S, Giani S, Giannitrapani R, Gibin D, Gómez Cadenas J J J, González I, Gracia Abril G, Greeniaus G, Greiner W, Grichine V, Grossheim A, Guatelli S, Gumplinger P, Hamatsu R, Hashimoto K, Hasui H, Heikkinen A, Howard A, Ivanchenko V, Johnson A, Jones F W W, Kallenbach J, Kanaya N, Kawabata M, Kawabata Y, Kawaguti M, Kelner S, Kent P, Kimura A, Kodama T, Kokoulin R, Kossov M, Kurashige H, Lamanna E, Lampén T, Lara V, Lefebure V, Lei F, Liendl M, Lockman W, Longo F, Magni S, Maire M,

Medernach E, Minamimoto K, Mora de Freitas P, Morita Y, Murakami K, Nagamatu M, Nartallo R, Nieminen P, Nishimura T, Ohtsubo K, Okamura M, O'Neale S, Oohata Y, Paech K, Perl J, Pfeiffer A, Pia M G G, Ranjard F, Rybin A, Sadilov S, Di Salvo E, Santin G, Sasaki T, et al 2003 Geant4—a simulation toolkit *Nucl. Instruments Methods Phys. Res. A* **506** 250–303

Allen C, Borak T B, Tsujii H and Nickoloff J A 2011 Heavy charged particle radiobiology: Using enhanced biological effectiveness and improved beam focusing to advance cancer therapy *Mutat. Res. - Fundam. Mol. Mech. Mutagen.* **711** 150–7

Anon 2012 *Transforming Geant4 for the Future Report from the Workshop on Transforming Geant4 for the Future*

Augusto R S, Mendonca T M, Wenander F, Penescu L, Orecchia R, Parodi K, Ferrari A and Stora T 2016 New developments of 11C post-accelerated beams for hadron therapy and imaging *Nucl. Instruments Methods Phys. Res. B* **376** 374–8

Battistoni G, Mattei I and Muraro S 2016 Nuclear physics and particle therapy **1** 661–86

Bauer J, Unholtz D, Sommerer F, Kurz C, Haberer T, Herfarth K, Welzel T, Combs S E, Debus J and Parodi K 2013 Implementation and initial clinical experience of offline PET/CT-based verification of scanned carbon ion treatment *Radiother. Oncol.* **107** 218–26

Bethe H 1930 Zur Theorie des Durchgangs schneller Korpuskularstrahlen durch Materie *Ann. Phys.* **397** 325–400

Bloch F 1933 Bremsvermögen von Atomen mit mehreren Elektronen *Zeitschrift für Phys.* **81** 363–76

Bom V, Joulaeizadeh L and Beekman F 2012 Real-time prompt gamma monitoring in spot-scanning proton therapy using imaging through a knife-edge-shaped slit *Phys. Med. Biol.* **57**

297–308

Chang D S, Lasley F D, Das I J, Mendonca M S, Dynlacht J R, Chang D S, Lasley F D, Das I J, Mendonca M S and Dynlacht J R 2014 Oxygen Effect, Relative Biological Effectiveness and Linear Energy Transfer *Basic Radiotherapy Physics and Biology* (Springer International Publishing) pp 235–40

Chatterjee A, Alpen E L, Tobias C A, Llacer J and Alonso J 1981 HIGH ENERGY BEAMS OF RADIOACTIVE NUCLEI AND THEIR BIOMEDICAL APPLICATIONS *Int. J. Radiat. Oncol. Biol. Phys.* **7** 503–7

Chi Y, Tian Z and Jia X 2016 Modeling parameterized geometry in GPU-based Monte Carlo particle transport simulation for radiotherapy *Phys. Med. Biol.* **61** 5851–67

Chuong M, Badiyan S N, Yam M, Li Z, Langen K, Regine W, Morris C, Snider J, Mehta M, Huh S, Rutenberg M, Nichols R C and Nichols R C 2018 Pencil beam scanning versus passively scattered proton therapy for unresectable pancreatic cancer. *J. Gastrointest. Oncol.* **9** 687–93

Cirrone G A P, Cuttone G, Di Rosa F, Mazzaglia S E, Romano F, Attili A, Bourhaleb F, Russo G, Kataniemi P, Heikkinen A, Marchetto F and Jungwook S 2009 Hadrontherapy: An open source, Geant4-based application for proton-ion therapy studies *IEEE Nuclear Science Symposium Conference Record* pp 4186–9

Connell P P and Hellman S 2009 Advances in radiotherapy and implications for the next century: A historical perspective *Cancer Res.* **69** 383–92

DANZKER M, KESSARIS N D and LAUGHLIN J S 1959 Absorbed dose and linear energy transfer in radiation experiments. *Radiology* **72** 51–61

Dudouet J, Cussol D, Durand D and Labalme M 2013 Benchmarking GEANT4 nuclear models for carbon-therapy at 95 MeV / A *Benchmarking*

Ebner D K and Kamada T 2016 The Emerging Role of Carbon-Ion Radiotherapy. *Front. Oncol.* **6** 140

Enghardt W, Debus J, Haberer T, Hasch B G, Hinz R, Jgkel O, Krgmer M, Lauckner K, Pawelke J and Phnisch F 1999 *Positron emission tomography for quality assurance of cancer therapy with light ion beams* vol 654

Fano U 1963 Penetration of Protons, Alpha Particles, and Mesons *Annu. Rev. Nucl. Sci.* **13** 1–66

Ferrero V, Fiorina E, Morrocchi M, Pennazio F, Baroni G, Battistoni G, Belcari N, Ciocca M, Del Guerra A, Donetti M, Giordanengo S, Giraudo G, Patera V, Peroni C, Rivetti A, Dionisio da Rocha Rolo M, Rossi S, Rosso V, Sportelli G, Tampellini S, Valvo F, Wheadon R, Cerello P, Giuseppina Bisogni M, di Roma S, Veronica Ferrero I, Camarlinghi N N, Ciocca M, Del Guerra A, Donetti M, Giordanengo S, Giraudo G, Patera V, Peroni C, Rivetti A, Rolo M D da R, Rossi S, Rosso V, Sportelli G, Tampellini S, Valvo F, Wheadon R, Cerello P and Bisogni M G 2018 Online proton therapy monitoring: clinical test of a Silicon-photodetector-based in-beam PET *Sci. Rep.* **8** 4100

Le Foulher F, Bajard M, Chevallier M, Dauvergne D, Freud N, Henriquet P, Karkar S, Letang J M, Lestand L, Plescak R, Ray C, Schardt D, Testa E and Testa M 2010 Monte Carlo Simulations of Prompt-Gamma *IEEE Trans. Nucl. Sci.* **57** 2768–72

Geant4 Collaboration 2017 *Guide for physics list*

Hendry J H 2005 Protective Effects on Microorganisms in Radiation Sterilised Tissues *Sterilisation of Tissues Using Ionising Radiations* (Elsevier Inc.) pp 331–8

Highland V L 1975 Some practical remarks on multiple scattering *Nucl. Instruments Methods* **129** 497–9

Jakel O 2006 Heavy Ion Radiotherapy *New Technologies in Radiation Oncology* pp 365–77

Jongen Y and Stichelbaut F 2003 39th PTCOG meeting San Francisco, California, USA *Verification of the proton beam position in the patient by the prompt gamma rays emission.* (San Franscico)

Kanai T, Endo M, Minohara S, Miyahara N, Koyama-Ito H, Tomura H, Matsufuji N, Futami Y, Fukumura A, Hiraoka T, Furusawa Y, Ando K, Suzuki M, Soga F and Kawachi K 1999 *BIOPHYSICAL CHARACTERISTICS OF HIMAC CLINICAL IRRADIATION SYSTEM FOR HEAVY-ION RADIATION THERAPY*

Kanazawa M, Kitagawa A, Kouda S, Nishio T, Torikoshi M, Noda K, Murakami T, Suda M, Tomitani T, Kanai T, Futami Y, Shinbo M, Urakabe E and Iseki Y 2002 Application of an RI-beam for cancer therapy: In-vivo verification of the ion-beam range by means of positron imaging *Nucl. Phys. A*

Karger C P, Jäkel O, Palmans H and Kanai T 2010 Dosimetry for ion beam radiotherapy *Phys. Med. Biol.* **55** R193–234

Kitagawa A, Furusawa Y, Kanai T, Kanazawa M, Mizuno H, Muramatsu M, Sato S, Suda M, Tomitani T, Urakabe E, Yoshimoto M, Li Q, Wei Z, Hanawa K, Iseki Y and Sato K 2006 Medical application of radioactive nuclear beams at HIMAC *Rev. Sci. Instrum.* **77**

Kraan A C 2015 Range Verification Methods in Particle Therapy: Underlying Physics and Monte Carlo Modeling. *Front. Oncol.* **5** 150

Krimmer J, Dauvergne D, Létang J M M and Testa É 2018 Prompt-gamma monitoring in hadrontherapy: A review *Nucl. Instruments Methods Phys. Res. Sect. A Accel. Spectrometers, Detect. Assoc. Equip.* **878** 58–73

Maccabee H D, Madhvanath U and Raju M R 1969 Tissue activation studies with alpha-particle beams. *Phys. Med. Biol.* **14** 213–24

Mackin D, Peterson S, Beddar S and Polf J C 2012 Evaluation of a stochastic reconstruction algorithm for use in Compton camera imaging and beam range verification from secondary gamma emission during proton therapy *Phys. Med. Biol.* **57** 3537–3353

Marion J B 1974 THE EFFECTS OF NUCLEAR RADIATIONS *Energy in Perspective* (Elsevier) pp 140–69

Min C H, Kim C H, Youn M Y and Kim J W 2006 Prompt gamma measurements for locating the dose falloff region in the proton therapy *Appl. Phys. Lett.* **89**

Minhoara S, Fukuda S, Kanematsu N, Takei Y, Furukawa T, Inaniwa T, Matsufuji N, Mori S and Noda K 2010 Recent Innovations in Carbon-Ion Radiotherapy *J. Radiat. Res.* **51** 385–92

Minohara S, Fukuda S, Kanematsu N, Takei Y, Furukawa T, Inaniwa T, Matsufuji N, Mori S and Noda K 2010 Recent Innovations in Carbon-Ion Radiotherapy *J. Radiat. Res* **51** 385–92

Mohamad O, Makishima H and Kamada T 2018 Evolution of Carbon Ion Radiotherapy at the National Institute of Radiological Sciences in Japan. *Cancers (Basel).* **10**

Mohamad O, Sishc B J, Saha J, Pompos A, Rahimi A, Story M D, Davis A J and Kim D W N 2017 Carbon ion radiotherapy: A review of clinical experiences and preclinical research, with an emphasis on DNA damage/repair *Cancers (Basel).* **9** 1–30

Mohammadi A, Tashima H, Iwao Y, Takyu S, Akamatsu G, Nishikido F, Yoshida E, Kitagawa A, Parodi K and Yamaya T 2019 Range verification of radioactive ion beams of ^{11}C and ^{15}O using in-beam PET imaging *Phys. Med. Biol.* **64** 145014

Moore. C S, Wood. T J, Avery G, Balcam S, Needler L, Smith A, Saunderson J R and Beavis A W 2015 Investigating the use of an anti-scatter grid in digital CR chest radiography *Hull East York Hosp. NHS Trust* **86** 1–7

Newhauser W D and Zhang R 2015 The physics of proton therapy. *Phys. Med. Biol.* **60** R155--

209

Nie W, Jones K C, Petro S, Kassaee A, Sehgal C M and Avery S 2018 Proton range verification in homogeneous materials through acoustic measurements *Phys. Med. Biol.* **63**

Paganetti H 2012 Range uncertainties in proton therapy and the role of Monte Carlo simulations. *Phys. Med. Biol.* **57** R99--117

Palta J R 2014 53rd PTCOG meeting Shanghai, China *Understanding the Uncertainties in Proton Therapy* (Shanghai)

Park J H, Kim S H, Ku Y, Kim C H, Lee H R, Jeong J H, Lee S B and Shin D H 2019 Multi-slit prompt-gamma camera for locating of distal dose falloff in proton therapy *Nucl. Eng. Technol.* **51** 1406–16

Park S H and Kang J O 2011 Basics of particle therapy I: physics *Radiat. Oncol. J.* **29** 135

Parodi K 2016 On- and off-line monitoring of ion beam treatment *Nucl. Instruments Methods Phys. Res. Sect. A Accel. Spectrometers, Detect. Assoc. Equip.* **809** 113–9

Parodi K, Bortfeld T, Enghardt W, Fiedler F, Knopf A, Paganetti H, Pawelke J, Shakirin G and Shih H 2008 PET imaging for treatment verification of ion therapy: Implementation and experience at GSI Darmstadt and MGH Boston *Nucl. Instruments Methods Phys. Res. Sect. A Accel. Spectrometers, Detect. Assoc. Equip.* **591** 282–6

Parodi K, Paganetti H, Shih H A, Michaud S, Loeffler J S, DeLaney T F, Liebsch N J, Munzenrider J E, Fischman A J, Knopf A and Bortfeld T 2007 Patient study of in vivo verification of beam delivery and range, using positron emission tomography and computed tomography imaging after proton therapy. *Int. J. Radiat. Oncol. Biol. Phys.* **68** 920–34

Parodi K and Polf J C 2018 In vivo range verification in particle therapy *Med. Phys.* **45** e1036–50

Phillips G W 1995 Gamma-ray imaging with Compton cameras *Nucl. Inst. Methods Phys. Res. B*

99 674–7

Pinto M, Bajard M, Brons S, Chevallier M, Dauvergne D, Dedes G, De Rydt M, Freud N, Krimmer J, La Tessa C, Lï¿½tang J M, Parodi K, Pleskač R, Prieels D, Ray C, Rinaldi I, Roellinghoff F, Schardt D, Testa E and Testa M 2015 Absolute prompt-gamma yield measurements for ion beam therapy monitoring *Phys. Med. Biol.* **60** 565–94

Pinto M, Dauvergne D, Freud N, Krimmer J, Letang J M, Ray C, Roellinghoff F and Testa E 2014 Design optimisation of a TOF-based collimated camera prototype for online hadrontherapy monitoring *Phys. Med. Biol.* **59** 7653–74

Pshenichnov I, Larionov A and Mishustin I 2006 Distributions of positron-emitting nuclei in proton and carbon-ion therapy studied with GEANT4 Related content PET monitoring with 3He beams *Phys. Med. Biol.*

PTCOG 2020 PTCOG - Facilities in Operation Online: https://www.ptcog.ch/index.php/facilities-in-operation

Richter C, Pausch G, Barczyk S, Priegnitz M, Keitz I, Thiele J, Smeets J, Stappen F Vander, Bombelli L, Fiorini C, Hotoiu L, Perali I, Prieels D, Enghardt W and Baumann M 2016 First clinical application of a prompt gamma based in vivo proton range verification system *Radiother. Oncol.*

Roellinghoff F, Benilov A, Dauvergne D, Dedes G, Freud N, Janssens G, Krimmer J, Létang J M, Pinto M, Prieels D, Ray C, Smeets J, Stichelbaut F and Testa E 2014 Real-time proton beam range monitoring by means of prompt-gamma detection with a collimated camera *Phys. Med. Biol.* **59** 1327–38

Schardt D, Elsässer T and Schulz-Ertner D 2010 Heavy-ion tumor therapy: Physical and radiobiological benefits

Smeets J, Roellinghoff F, Prieels D, Stichelbaut F, Benilov A, Busca P, Fiorini C, Peloso R, Basilavecchia M, Frizzi T, Dehaes J C and Dubus A 2012 Prompt gamma imaging with a slit camera for real-time range control in proton therapy *Phys. Med. Biol.* **57** 3371–405

Solevi P, Muñoz E, Solaz C, Trovato M, Dendooven P, Gillam J E, Lacasta C, Oliver J F, Rafecas M, Torres-Espallardo I and Llosá G 2016 Performance of MACACO Compton telescope for ion-beam therapy monitoring: First test with proton beams *Phys. Med. Biol.*

Testa E, Bajard M, Chevallier M, Dauvergne D, Le Foulher F, Freud N, Létang J M M, Poizat J C C, Ray C, Testa M, Dauvergne D, Bajard M, Poizat J C C, Chevallier M, Létang J M M, Testa E, Le Foulher F, Ray C, Bajard M, Chevallier M, Dauvergne D, Le Foulher F, Freud N, Létang J M M, Poizat J C C, Ray C and Testa M 2009 Dose profile monitoring with carbon ions by means of prompt-gamma measurements *Nucl. Instruments Methods Phys. Res. Sect. B Beam Interact. with Mater. Atoms* **267** 993–6

Testa E, Bajard M, Chevallier M, Dauvergne D, Le Foulher F, Freud N, Ĺtang J M, Poizat J C, Ray C and Testa M 2008 Monitoring the Bragg peak location of 73 MeVu carbon ions by means of prompt γ -ray measurements *Appl. Phys. Lett.*

Testa M 2010 *Physical measurements for ion range verification in charged particle therapy* (Lyon: DE L'UNIVERSITE DE LYON)

Tobias C A, Benton E V., Capp M P, Chatarjee A, Cruty M R and Henke R P 1977 PARTICLE RADIOGRAPHY AND AUTOACTIVATION *Int. J. Radiat. Oncol. Biol. Phys.* **3** 35–44

Tsuboi K 2020 Early History of Biology and Clinical Application of Proton Beam Therapy *Proton Beam Radiotherapy* (Springer Singapore) pp 9–21

Tsujii H and Kamada T 2012 A Review of Update Clinical Results of Carbon Ion Radiotherapy *Jpn. J. Clin. Oncol.* **42**

Urakabe E, Kanai T, Kanazawa M, Kitagawa A, Noda K, Tomitani T, Suda M, Iseki Y, Hanawa K, Sato K, Shimbo M, Mizuno H, HIRATA Y, Futami Y, Iwashita Y and Noda A 2001 Spot Scanning Using Radioactive 11 C Beams for Heavy-Ion Radiotherapy *Jpn. J. Appl. Phys* **40** 2540–8

Wilson R R 1946 Radiological use of fast protons. *Radiology* **47** 487–91

Xie Y, Bentefour E H, Janssens G, Smeets J, Vander Stappen F, Hotoiu L, Yin L, Dolney D, Avery S, O'Grady F, Prieels D, McDonough J, Solberg T D, Lustig R A, Lin A and Teo B-K K 2017 Prompt Gamma Imaging for In Vivo Range Verification of Pencil Beam Scanning Proton Therapy *Int. J. Radiat. Oncol.* **99** 210–8

Yan Y-L, Liu X-G, Dai Z-Y, Ma Y-Y, He P-B, Shen G-S, Ji T-F, Zhang H and Li Q 2017 Spot-scanning beam delivery with laterally- and longitudinally-mixed spot size pencil beams in heavy ion radiotherapy *Chinese Phys. C* **41** 98201

Zarifi M, Guatelli S, Qi Y, Bolst D, Prokopovich D and Rosenfeld A 2019 Characterization of prompt gamma ray emission for in vivo range verification in particle therapy: A simulation study *Phys. Medica* **62** 20–32

Zheng Y, Kang Y, Zeidan O and Schreuder N 2016 An end-to-end assessment of range uncertainty in proton therapy using animal tissues *Phys. Med. Biol.* **61** 8010–24

Zhu X, España S, Daartz J, Liebsch N, Ouyang J, Paganetti H, Bortfeld T R and El Fakhri G 2011 Monitoring proton radiation therapy with in-room PET imaging *Phys. Med. Biol.* **56** 4041–57

Ziegler J F, Ziegler M D and Biersack J P 2010 SRIM - The stopping and range of ions in matter (2010) *Nucl. Instruments Methods Phys. Res. Sect. B Beam Interact. with Mater. Atoms* **268** 1818–23

CHAPTER 4: SUMMARY AND FUTURE WORK

Particle therapy has great potential for cancer treatment owing to its unique dose confirmation, thanks to narrow Bragg-peak and high RBE. Because the particles used for therapy stop in the tissue at its Bragg-peak, it is difficult to verify the range and dose using the treatment particle beam. Due to the range uncertainties, the lack of range verification techniques in clinic has limited the scope of particle therapy, and hence sacrifices safety margins. Several groups are working in addressing this problem using different approaches. Secondary radiation emitted during the treatment due to nuclear interaction is found to correlate with the range of the particles, and hence are extensively explored as a possible solution for this problem.

In this dissertation, we investigated two range verification approaches, PET and prompt gamma imaging, using a Monte Carlo simulation package, Geant4. PET utilizes the annihilation gammas generated during the nuclear interaction. The positron emitting nuclei (PEN) are generated due to the interaction of carbon ions with the materials in the tissue (hydrogen, oxygen, and carbon etc.). The positrons hence emitted due to PEN decay annihilate with electrons in matter. This annihilation leads to generation of two photons of 511 KeV, which can be used for PET to verify the range of the carbon ions. On the other hand, during the nuclear interaction, the nuclei which are excited undergo deexcitation by emitting more energetic photons, namely prompt gamma (PG). PG provides the potential for online real time range verification.

The first part of this dissertation was devoted to the possibility of boosting range verification capability by combining PET and PGI. Because low signal and long acquisition time are shortcomings of PET, we investigated the effect of replacing regular C-12 ions with C-11 ions. We envision that this is a possible avenue to boost PET signal because the use of C-11 could result

in significant increase of AG yield. For low incident energies, there were around 6~11 folds more AGs generated by C-11 ions than that by C-12 ions. For the high energies, there were around 30%~60% higher AGs by C-11. In the worst scenario, PG yield from C-11 was 0.82 times of that from C-12. The PG yield difference between two carbon ion species became negligible as the energy increased. These results demonstrate that using C-11 ion beams for combined PGI and PET has great potential to improve online range verification accuracy and precision.

In the second part of this dissertation, we focused more on the PGI camera design. We were particularly interested in the optimization of the multi-slit camera as it has the potential of covering the whole beam path length using a simple mechanical collimation. For this study, we investigated five key parameters of the multi-slit camera, including the slit and slab width, the height of the collimator as well as the distance of the collimator and the detector to the beam axis. A total of 4,752 simulations were performed and analyzed to look for the best design based on signal to background ratio, sensitivity, peak to secondary peak ratio and also slab to slit ratio along with the spatial resolution. Although a perfect overlap among all evaluation criteria did not exist, we found that for higher signal to background ratio, sensitivity and slab to slit ratio, the camera design generally requires large slit width, small slab width, a collimator of height 150 mm and a detector being placed about half meter away from the beam axis. This setup was later verified using carbon ion impinging in water to show a sharp peak capable of identifying the Bragg-peak. These results suggested that signal-to-background ratio and sensitivity may be more important for capturing the distal fall-off of PG in a uniform phantom.

Even though we only explored one dimensional range verification for PET and PGI in this work. The simulation methods can be readily extended to investigate 3D PET and PGI, which is able to verify or monitor not only the longitudinal beam range, but also the lateral spread. Such a

simulation capability will be a critical step for the future design of fast PET imaging and effective 3D PGI methods. Another future direction is to include patient-specific anatomy into Monte Carlo simulation and to evaluate range verification performance in a more realistic setting. Our endeavor on real-time range verification for particle therapy will be built on this simulation framework and contribute significantly to cancer patient management.

APPENDIX A

We adapted code of the hadrontherapy example of Geant4 and listed the structures of sub-routines as well as the routines that need the user inputs for the simulation in Chapter 2. More details can be found in G. G. P. Cirrone *et al.*, "Hadrontherapy: An open source, Geant4-based application for proton-ion therapy studies," *2009 IEEE Nuclear Science Symposium Conference Record (NSS/MIC)*, Orlando, FL, 2009, pp. 4186-4189, doi: 10.1109/NSSMIC.2009.5402279.

1. Hadronthearpy overview

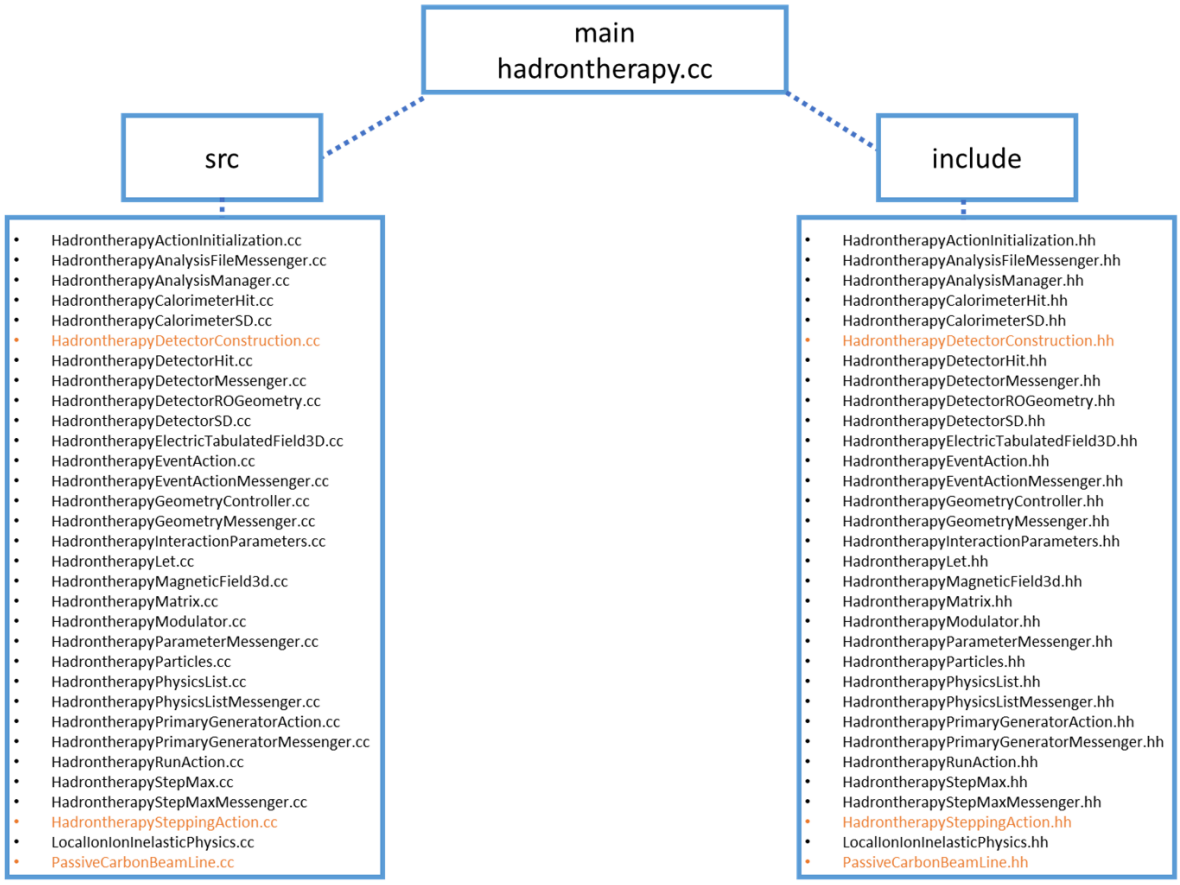

The main function hadrontherapy.cc initializes the detector construction, physics, analysis, run and action in the simulation. These source files then call in other files that govern sensitive detector,

field, primary generator, LET calculation, and step handler. The definitions for all the variables are defined in the header file like any C++ code. The source and header files modified for our simulations are highlighted in orange and detailed below.

2. HadrontherapySteppingaction.cc

HadrontherapySteppingAction.cc

```
#include "G4SteppingManager.hh"
#include "G4TrackVector.hh"
#include "HadrontherapySteppingAction.hh"
#include "G4ios.hh"
#include "G4SteppingManager.hh"
#include "G4Track.hh"
#include "G4Step.hh"
#include "G4StepPoint.hh"
#include "G4TrackStatus.hh"
#include "G4TrackVector.hh"
#include "G4ParticleDefinition.hh"
#include "G4ParticleTypes.hh"
#include "G4UserEventAction.hh"
#include "G4TransportationManager.hh"
#include "G4VSensitiveDetector.hh"
#include "HadrontherapyRunAction.hh"
#include "HadrontherapyAnalysisManager.hh"
#include "G4SystemOfUnits.hh"

////////////////////////////////////////////////////////////////////////////////
HadrontherapySteppingAction::HadrontherapySteppingAction( HadrontherapyRunAction *run)
{

////////////////////////////////////////////////////////////////////////////////
HadrontherapySteppingAction::~HadrontherapySteppingAction()
{

////////////////////////////////////////////////////////////////////////////////
void HadrontherapySteppingAction::UserSteppingAction(const G4Step* aStep)
{
G4StepPoint* PreStep = aStep->GetPreStepPoint();
G4StepPoint* PostStep = aStep->GetPostStepPoint();

G4double PreStepX =PreStep->GetPosition().x();
G4double PreStepY =PreStep->GetPosition().y();
G4double PreStepZ =PreStep->GetPosition().z();
G4double parentID =aStep->GetTrack()->GetParentID();
G4double trackID =aStep->GetTrack()->GetTrackID();

G4double PostStepX =PostStep->GetPosition().x();
G4double PostStepY =PostStep->GetPosition().y();
G4double PostStepZ  =PostStep->GetPosition().z();

// positions in the global coordinate system:
//G4ThreeVector posPreStep  = PreStep->GetPosition();
// G4ThreeVector posPostStep = PostStep->GetPosition();

G4TouchableHandle touchPreStep = PreStep->GetTouchableHandle();
G4TouchableHandle touchPostStep = PostStep->GetTouchableHandle();
//To get the current volume:
G4VPhysicalVolume* volumePre = touchPreStep->GetVolume();
```

```
G4VPhysicalVolume* volumePost =touchPostStep->GetVolume();

//To get its name:
G4String namePre = volumePre->GetName();
 G4String namePost;

if(volumePost){
 namePost = volumePost->GetName();
    }
G4int eventNum = G4RunManager::GetRunManager() -> GetCurrentEvent() -> GetEventID();
G4double eKin = aStep -> GetPreStepPoint() -> GetKineticEnergy();
G4double PosX = aStep->GetTrack()->GetPosition().x();
G4double PosY = aStep->GetTrack()->GetPosition().y();
G4double PosZ = aStep->GetTrack()->GetPosition().z();
G4double MomX = aStep->GetTrack()->GetMomentumDirection().x();
G4double MomY = aStep->GetTrack()->GetMomentumDirection().y();
G4double MomZ = aStep->GetTrack()->GetMomentumDirection().z();
G4double globalTime = aStep -> GetTrack()->GetGlobalTime()/ns;
G4String material= aStep -> GetTrack() -> GetMaterial() -> GetName();
G4String volume=  aStep->GetTrack()->GetVolume()->GetName();
G4Track* theTrack = aStep->GetTrack();
// Gamma defined is to write the process too
G4String process = aStep -> GetPostStepPoint() -> GetProcessDefinedStep() -> GetProcessName();
 if((namePre=="DetectorPhys" ) && aStep->GetTrack()->GetDefinition()->GetParticleName() == "gamma" && (PostStep->GetStepStatus() == fGeomBoundary))
    {
     if(eKin > .0 ){
    G4String CPName;
    if(aStep->GetTrack()->GetCreatorProcess()!=0){
          CPName = aStep->GetTrack()->GetCreatorProcess()->GetProcessName();
      //theTrack->SetTrackStatus(fStopAndKill);
      std::ofstream WriteDataIn("DetectorGamma.out", std::ios::app);
      WriteDataIn   <<    eKin                 << '\t' << "   "
            <<   PosX              << '\t' << "   "
            <<   PosY              << '\t' << "   "
            <<   PosZ              << '\t' << "   "
            <<   MomX              << '\t' << "   "
            <<   MomY              << '\t' << "   "
            <<   MomZ              << '\t' << "   "
            <<   globalTime              << '\t' << "   "
            <<   process           << '\t' << "   "
            <<   parentID              << '\t' << "   "
            <<   trackID             << '\t' << "   "
                <<   CPName          << '\t' << "   "
            <<   G4endl;}

}
}

if((aStep->GetTrack()->GetVolume()->GetName()=="DetectorPhys") && aStep->GetTrack()->GetDefinition()->GetParticleName() == "neutron" && (PostStep->GetStepStatus() == fGeomBoundary))
    {
     if(eKin > .0 ){
        G4String CPName;
        if(aStep->GetTrack()->GetCreatorProcess()!=0){
              CPName = aStep->GetTrack()->GetCreatorProcess()->GetProcessName();
          std::ofstream WriteDataIn("DetectorNeutron.out", std::ios::app);
          WriteDataIn   <<    eKin                 << '\t' << "   "
                <<   PosX              << '\t' << "   "
                <<   PosY              << '\t' << "   "
                <<   PosZ              << '\t' << "   "
                <<   MomX              << '\t' << "   "
                <<   MomY              << '\t' << "   "
                <<   MomZ              << '\t' << "   "
                <<   globalTime              << '\t' << "   "
                <<   process           << '\t' << "   "
                <<   parentID              << '\t' << "   "
                <<   trackID             << '\t' << "   "
                    <<   CPName          << '\t' << "   "
                <<   G4endl;}}
}
```

3. HadrontherapySteppingaction.hh

HadrontherapySteppingAction.hh

```
#ifndef HadrontherapySteppingAction_h
#define HadrontherapySteppingAction_h 1

#include "G4UserSteppingAction.hh"
#include "G4Event.hh"
#include "G4EventManager.hh"
#include "G4ios.hh"
#include "globals.hh"

class HadrontherapyRunAction;
class HadrontherapySteppingMessenger;


#ifndef G4NOHIST
class HepTupleManager;
class HepHistogram;
#endif

class HadrontherapySteppingAction : public G4UserSteppingAction
{
public:
  HadrontherapySteppingAction(HadrontherapyRunAction*);
  ~HadrontherapySteppingAction();

  void UserSteppingAction(const G4Step*);

private:
  HadrontherapyRunAction* runAction;
};
#endif

```

4. HadrontherapyDetectorConstruction.cc

HadrontherapyDetectorConstruction.cc

```
#include "G4UnitsTable.hh"
#include "G4SDManager.hh"
#include "G4RunManager.hh"
#include "G4GeometryManager.hh"
#include "G4SolidStore.hh"
#include "G4PhysicalVolumeStore.hh"
#include "G4LogicalVolumeStore.hh"
#include "G4Box.hh"
#include "G4LogicalVolume.hh"
#include "G4ThreeVector.hh"
#include "G4PVPlacement.hh"
#include "globals.hh"
#include "G4Transform3D.hh"
#include "G4RotationMatrix.hh"
#include "G4Colour.hh"
#include "G4UserLimits.hh"
#include "G4UnitsTable.hh"
#include "G4VisAttributes.hh"
#include "G4NistManager.hh"
#include "HadrontherapyDetectorConstruction.hh"
#include "HadrontherapyDetectorROGeometry.hh"
#include "HadrontherapyDetectorMessenger.hh"
#include "HadrontherapyDetectorSD.hh"
#include "HadrontherapyCalorimeterSD.hh"
#include "HadrontherapyMatrix.hh"
#include "HadrontherapySteppingAction.hh"
#include "HadrontherapyLet.hh"
//#include "PassiveProtonBeamLine.hh"
#include "PassiveCarbonBeamLine.hh"
#include "HadrontherapyAnalysisManager.hh"
#include "G4MultiFunctionalDetector.hh"
#include "G4SystemOfUnits.hh"
#include <cmath>
HadrontherapyDetectorConstruction* HadrontherapyDetectorConstruction::instance = 0;
/////////////////////////////////////////////////////////////////////////////
HadrontherapyDetectorConstruction::HadrontherapyDetectorConstruction(G4VPhysicalVolume* physicalTreatmentRoom
: motherPhys(physicalTreatmentRoom), // pointer to WORLD volume
detectorSD(0), detectorROGeometry(0), matrix(0),
phantom(0), detector(0),  calorimeter(0), calorimeterSD(0),
phantomLogicalVolume(0), detectorLogicalVolume(0), calorimeterLogicalVolume(0),
phantomPhysicalVolume(0), detectorPhysicalVolume(0), calorimeterPhysicalVolume(0),
aRegion(0)
{
    HadrontherapyAnalysisManager::GetInstance();
    detectorMessenger = new HadrontherapyDetectorMessenger(this);
    // Default detector voxels size
    // 200 slabs along the beam direction (X)
    sizeOfVoxelAlongX = 1.0 *mm;
    sizeOfVoxelAlongY = 1.0 *mm;
    sizeOfVoxelAlongZ = 1.0 *mm;
  sizeOfPixelAlongX = 0.1 * cm; //
```

```
52      sizeOfPixelAlongY = 0.1 * cm;
53      sizeOfPixelAlongZ = 0.1 * cm;
54        // Define here the material of the water phantom and of the detector
55      density_pmma = 1.19*g/cm3;
56      G4Element* elO = new G4Element ("Oxygen", "O", z= 8., a = 16.0 * g/mole );
57      G4Element* elH = new G4Element ("Hydrogen", "H", z=1, a = 1.01 * g/mole );
58      G4Element* elC = new G4Element ("Carbon", "C", z=6., a = 12.01 * g/mole );
59     G4Material* PMMA = new G4Material("PMMA",density_pmma , 3);
60     PMMA -> AddElement(elC, 5);
61     PMMA -> AddElement(elO, 2);
62     PMMA -> AddElement(elH, 8);
63        G4NistManager* man = G4NistManager::Instance();
64       G4Element* F = man->FindOrBuildElement("F");
65       //G4Element* Pb = man->FindOrBuildElement("Pb");
66       G4Element* Ba = man->FindOrBuildElement("Ba");
67        G4Material *Air = man->FindOrBuildMaterial("G4_AIR");
68        G4Material *BariumFluoride = man->FindOrBuildMaterial("G4_BARIUM_FLUORIDE");
69        SetPhantomMaterial("G4_WATER");
70        calorimeterMaterial = BariumFluoride;
71        pixelMaterial= BariumFluoride;
72        //collimatorlMaterial = Pb;
73        G4cout << G4endl << "The materials defined are : " << G4endl << G4endl;
74        G4cout << *(G4Material::GetMaterialTable()) << G4endl;
75        // Construct geometry (messenger commands)
76        SetCalorimeterSize(5.0*cm, 15.0*cm, 5.0*cm);
77        SetDetectorSize(50.0*cm, 5.*cm, 5.*cm);
78        SetPhantomSize(50.0 *cm, 5. *cm, 5. *cm);
79        SetCalorimeterPosition(G4ThreeVector(0. *cm, 68.0 *cm, 0. *cm));
80        SetPhantomPosition(G4ThreeVector(0. *cm, 0. *cm, 0. *cm));
81        SetDetectorToPhantomPosition(G4ThreeVector(0. *cm, 0. *cm, 0. *cm));
82        SetDetectorPosition();
83        UpdateGeometry();
84    }
85
86    ////////////////////////////////////////////////////////////////////////////
87    HadrontherapyDetectorConstruction::~HadrontherapyDetectorConstruction()
88    {
93
94    ////////////////////////////////////////////////////////////////////////////
95    HadrontherapyDetectorConstruction* HadrontherapyDetectorConstruction::GetInstance()
96    {
99    void HadrontherapyDetectorConstruction::ConstructPhantom()
100   {
149   void HadrontherapyDetectorConstruction::ConstructDetector()
150   {
190   void HadrontherapyDetectorConstruction::ConstructCalorimeter()
191   {
232   ////////////////////////////////////////////////////////////////////////////
```

```
233  void HadrontherapyDetectorConstruction::InitializeDetectorROGeometry(
237  {
253
254    ////////////////////////////////////////////////////////////////////////
255    void  HadrontherapyDetectorConstruction::ParametersCheck()
256    {
280
281
282    void HadrontherapyDetectorConstruction::SetVoxelMaterial(G4int j, G4String materialChoice)
283    {
295
296
297    void HadrontherapyDetectorConstruction::SetPixelMaterial(G4int j, G4String materialChoice)
298    {
310
311    ////////////////////////////////////////////////////////////////////////
312    G4bool HadrontherapyDetectorConstruction::SetPhantomMaterial(G4String material)
313    {
339    ////////////////////////////////////////////////////////////////////////////
340    void HadrontherapyDetectorConstruction::SetPhantomSize(G4double sizeX, G4double sizeY, G4double sizeZ)
341    {
346
347    ////////////////////////////////////////////////////////////////////////////
348    void HadrontherapyDetectorConstruction::SetDetectorSize(G4double sizeX, G4double sizeY, G4double sizeZ)
349    {
355
356    ////////////////////////////////////////////////////////////////////////////
357    void HadrontherapyDetectorConstruction::SetVoxelSize(G4double sizeX, G4double sizeY, G4double sizeZ)
358    {
363    void HadrontherapyDetectorConstruction::SetCalorimeterPosition(G4ThreeVector pos)
364    {
367    ////////////////////////////////////////////////////////////////////////////
368    void HadrontherapyDetectorConstruction::SetCalorimeterSize(G4double sizeX, G4double sizeY, G4double sizeZ)
369    {
375
376    // ////////////////////////////////////////////////////////////////////////////
377
378    void HadrontherapyDetectorConstruction::SetPixelSize(G4double sizeX, G4double sizeY, G4double sizeZ)
379    {
384    ////////////////////////////////////////////////////////////////////////
385    void HadrontherapyDetectorConstruction::SetPhantomPosition(G4ThreeVector pos)
386    {
389
390    ////////////////////////////////////////////////////////////////////////////
391    void HadrontherapyDetectorConstruction::SetDetectorToPhantomPosition(G4ThreeVector displ)
392    {
395
396    ////////////////////////////////////////////////////////////////////////////
397    void HadrontherapyDetectorConstruction::UpdateGeometry()
398    {
515
516
517    void HadrontherapyDetectorConstruction::PrintParameters()
518    {
545
546    void HadrontherapyDetectorConstruction::ConstructSDandField()
547    {
```

5. HadrontherapyDetectorConstruction.hh

HadrontherapyDetectorConstruction.hh

```
#ifndef HadrontherapyDetectorConstruction_H
#define HadrontherapyDetectorConstruction_H 1
#include "G4Box.hh"
#include "globals.hh"
#include "G4VisAttributes.hh"
#include "G4LogicalVolume.hh"
#include "G4UnitsTable.hh"
#include "HadrontherapyDetectorROGeometry.hh"
#include "PassiveCarbonBeamLine.hh"
#include <set>
class G4VPhysicalVolume;
class G4LogicalVolume;
class G4PVPlacement;
class HadrontherapyDetectorROGeometry;
class HadrontherapyCalorimeterROGeometry;
class HadrontherapyDetectorMessenger;
class HadrontherapyDetectorSD;
class HadrontherapyCalorimeterSD;
class HadrontherapyMatrix;
class HadrontherapyLet;
class HadrontherapySteppingAction;
const G4int MaxVoxel = 2000;                // 0 + 2000
const G4int MaxPixel = 1;                  // 0 + 2000
const G4int MaxPixelX = 1;                  // 0 + 2000
const G4int MaxPixelY = 1;
class HadrontherapyDetectorConstruction
{
public:
  typedef std::set<G4VPhysicalVolume*> ScoringPhysVolumes_detector_t;
  typedef std::set<G4VPhysicalVolume*> ScoringPhysVolumes_calorimeter_t;
  typedef std::set<G4VPhysicalVolume*> ScoringPhysVolumes_pixel_t;
  HadrontherapyDetectorConstruction(G4VPhysicalVolume*);

  ~HadrontherapyDetectorConstruction();

public:
static HadrontherapyDetectorConstruction* GetInstance();
  void InitializeDetectorROGeometry(HadrontherapyDetectorROGeometry*,
                    G4ThreeVector detectorToWorldPosition, G4ThreeVector calorimeterToWorldPosition);
  void InitializeCalorimeterROGeometry(HadrontherapyCalorimeterROGeometry*, G4ThreeVector calorimeterToWorldPosition);
  G4VPhysicalVolume* motherPhys;
  HadrontherapyDetectorSD*         detectorSD; // Pointer to sensitive detector
  HadrontherapyCalorimeterSD*         calorimeterSD; // Pointer to sensitive calorimeter
  void ConstructSDandField();
private:

  void ConstructPhantom();
  void ConstructDetector();
  void ConstructCalorimeter();
  void ParametersCheck();
  void CheckOverlaps();
```

```
52  public:
53  // Get detector position relative to WORLD
54  inline G4ThreeVector GetDetectorToWorldPosition()
55    {
58
59  // Get detector position relative to WORLD
60  inline G4ThreeVector GetCalorimeterToWorldPosition()
61    {
64
65  ////////////////////////////////////////////////////////////////////////////
66  // Get displacement between phantom and detector by detector position (center of), phantom (center of) and detector sizes
67  inline G4ThreeVector GetDetectorToPhantomPosition()
68  {
74
75  ////////////////////////////////////////////////////////////////////////////
76  // Calculate (and set) detector position by displacement, phantom and detector sizes
77  inline void SetDetectorPosition()
78    {
86  ////////////////////////////////////////////////////////////////////////////
87  // Check whether detector is inside phantom
88  inline bool IsInside(G4double detectorX,
89               G4double detectorY,
90               G4double detectorZ,
91               G4double phantomX,
92               G4double phantomY,
93               G4double phantomZ,
94               G4ThreeVector pos)
95  {
139 ////////////////////////////////////////////////////////////////////////////
140   G4bool  SetPhantomMaterial(G4String material);
141   void SetVoxelSize(G4double sizeX, G4double sizeY, G4double sizeZ);
142   void SetPixelSize(G4double sizeX, G4double sizeY, G4double sizeZ);
143   void SetDetectorSize(G4double sizeX, G4double sizeY, G4double sizeZ);
144   void SetPhantomSize(G4double sizeX, G4double sizeY, G4double sizeZ);
145   void SetPhantomPosition(G4ThreeVector);
146   void SetCalorimeterPosition(G4ThreeVector);
147   void SetDetectorToPhantomPosition(G4ThreeVector DetectorToPhantomPosition);
148   void UpdateGeometry();
149   void PrintParameters();
150   G4LogicalVolume* GetDetectorLogicalVolume(){ return detectorLogicalVolume;}
151   const G4VPhysicalVolume* GetCalorimeterPV() const;
152   void SetCalorimeterSize(G4double sizeX, G4double sizeY, G4double sizeZ);
153   void SetPixelMaterial (G4int, G4String);
154   void SetVoxelNumber   (G4int);
155   void SetVoxelMaterial (G4int, G4String);
156   G4double GetPixelSizeXY() const         {return sizeOfPixelAlongX;};
157   G4int GetNbOfPixels() const             {return NbOfPixels;}; //mandatory for XrayFluoSD
158   G4int GetNbOfPixelRows() const          {return numberOfVoxelsAlongY;};
159   G4int GetNbOfPixelColumns() const        {return numberOfVoxelsAlongX;};
160   const G4VPhysicalVolume* GetphysiPixel() const {return physiPixel;};
161   G4Material* GetPixelMaterial() const {return pixelMaterial;};
```

```
  G4Material* GetPixelMaterial() const {return pixelMaterial;};
  G4Material*        GetMaterial()   {return detectorMaterial;};

private:
  static HadrontherapyDetectorConstruction* instance;
  HadrontherapyDetectorMessenger* detectorMessenger;

  ScoringPhysVolumes_detector_t phys_scorers_detector;
  ScoringPhysVolumes_calorimeter_t phys_scorers_calorimeter;
  ScoringPhysVolumes_pixel_t phys_scorers_pixel;
  G4VisAttributes* skyBlue;
  G4VisAttributes* red;
  G4RotationMatrix* rotationMatrix;
  HadrontherapyDetectorROGeometry* detectorROGeometry; // Pointer to ROGeometry
  HadrontherapyCalorimeterROGeometry* calorimeterROGeometry; // Pointer to ROGeometry
  HadrontherapyMatrix*            matrix;
  HadrontherapyMatrix*            matrix_etaInt;
  HadrontherapyLet*               let;
  G4Box *phantom , *detector, *calorimeter, *collimator1;
  G4LogicalVolume *phantomLogicalVolume, *detectorLogicalVolume, *calorimeterLogicalVolume, *collimator1LogicalVolume;
  G4VPhysicalVolume *phantomPhysicalVolume, *detectorPhysicalVolume, *calorimeterPhysicalVolume, *collimator1PhysicalVolume;
  G4double phantomSizeX;
  G4double phantomSizeY;
  G4double phantomSizeZ;
  G4double detectorSizeX;
  G4double detectorSizeY;
  G4double detectorSizeZ;
  G4double calorimeterSizeX;
  G4double calorimeterSizeY;
  G4double calorimeterSizeZ;
  G4ThreeVector phantomPosition, detectorPosition, detectorToPhantomPosition; //  phantom center, detector center, detector to phantom relative position
  G4double sizeOfVoxelAlongX;
  G4double sizeOfVoxelAlongY;
  G4double sizeOfVoxelAlongZ;
  G4double a;
  G4double z;
  G4double sizeOfPixelAlongX;
  G4double sizeOfPixelAlongY;
  G4double sizeOfPixelAlongZ;
  G4int numberOfVoxelsAlongX;
  G4int numberOfVoxelsAlongY;
  G4int numberOfVoxelsAlongZ;
  G4int numberOfPixelsAlongX;
  G4int numberOfPixelsAlongY;
  G4int numberOfPixelsAlongZ;
  G4double volumeOfVoxel, massOfVoxel, volumeOfPixel, massOfPixel;
  G4Material *phantomMaterial, *detectorMaterial, *calorimeterMaterial;
  G4String Pb;
  G4Region* aRegion;
  G4double density_pmma;
  G4double density_air;
```

```
  G4ThreeVector calorimeterPosition;

  G4ThreeVector voxelPosition[MaxVoxel];
  //G4ThreeVector voxelPosition;
  G4LogicalVolume  *voxelLogicalVolume[MaxVoxel];
  //G4LogicalVolume* voxelLogicalVolume;
  G4Material*         voxelMaterial[MaxVoxel];
  G4double            voxelMass[MaxVoxel];
  G4int            voxelNumber;

  G4Box*             solidPixel;
  G4LogicalVolume*   logicPixel[MaxPixel];
  G4VPhysicalVolume* physiPixel;
  G4int              PixelCopyNb;
  G4int              NbOfPixels;
  G4int              NbOfPixelRows;
  G4int              NbOfPixelColumns;
  G4double           PixelThickness;
  G4double           PixelSizeXY;
  G4Material*        pixelMaterial;
};
inline const G4VPhysicalVolume* HadrontherapyDetectorConstruction::GetCalorimeterPV() const  {
#endif
```

6. carbon_beamline.mac

carbon_beamline.mac

```
#########################
# Set of the verboses
/control/verbose 0
/tracking/verbose 0
/run/verbose 0
/event/verbose 0
# Set of the physic models
/Physics/addPhysics HADRONTHERAPY_1
#########################
/geometrySetup/selectGeometry Carbon
#########################
# Initialisation procedure
/run/initialize
#########################
# Set here the cut and the step max for the tracking.
# Suggested values of cut and step:
# Set cuts OUTSIDE the detector
/run/setCut 0.1 mm
# Set cuts ONLY inside the detector
#
/run/setCutForRegion DetectorLog 0.05 mm
/Step/waterPhantomStepMax 0.1 mm
#                       PRIMARY PARTICLES
/gps/pos/centre -25.3 0. 0. cm
/gps/pos/radius 0. mm
/gps/particle ion
/gps/ion 6 12 6
/gps/pos/type Beam
# the incident surface is in the y-z plane
/gps/pos/rot1 0 1 0
/gps/pos/rot2 0 0 1
# the beam is travelling along the x-axis without any angular dispersion (angular despersion set to 0.0)
/gps/ang/rot1 0 0 1
/gps/ang/rot2 0 1 0
/gps/ang/type beamld
/gps/ang/sigma_r 0. deg
# the beam energy is in gaussian profile
/gps/ene/type Gauss
/gps/ene/mono 1140 MeV
#########################
# Display the event number
# during the run
/event/printEventNumber 20000
#########################
# Start of the run
#########################
/random/setSeeds 111 222
/run/beamOn 10000000
/control/shell rm ./*rndm*

```

APPENDIX B

We adapted the hadrontherapy example to simulate multi-slit collimators described in Chapter 3. Similar to Appendix A, the snapshot of the codes that were modified are shown below along with the Bash script for looping the collimator.

1. HadronthearpyDetectorConstruction.cc

HadrontherapyDetectorConstruction.cc

```
#include "G4UnitsTable.hh"
#include "G4SDManager.hh"
#include "G4RunManager.hh"
#include "G4GeometryManager.hh"
#include "G4SolidStore.hh"
#include "G4PhysicalVolumeStore.hh"
#include "G4LogicalVolumeStore.hh"
#include "G4Box.hh"
#include "G4LogicalVolume.hh"
#include "G4ThreeVector.hh"
#include "G4PVPlacement.hh"
#include "globals.hh"
#include "G4Transform3D.hh"
#include "G4RotationMatrix.hh"
#include "G4Colour.hh"
#include "G4UserLimits.hh"
#include "G4UnitsTable.hh"
#include "G4VisAttributes.hh"
#include "G4NistManager.hh"
#include "HadrontherapyDetectorConstruction.hh"
#include "HadrontherapyDetectorROGeometry.hh"
#include "HadrontherapyDetectorMessenger.hh"
#include "HadrontherapyDetectorSD.hh"
#include "HadrontherapyCalorimeterSD.hh"
#include "HadrontherapyMatrix.hh"
#include "HadrontherapySteppingAction.hh"
#include "HadrontherapyLet.hh"
//#include "PassiveProtonBeamLine.hh"
#include "PassiveCarbonBeamLine.hh"
#include "HadrontherapyAnalysisManager.hh"
#include "G4MultiFunctionalDetector.hh"
#include "G4SystemOfUnits.hh"
#include <cmath>
HadrontherapyDetectorConstruction* HadrontherapyDetectorConstruction::instance = 0;
/////////////////////////////////////////////////////////////////////////////
HadrontherapyDetectorConstruction::HadrontherapyDetectorConstruction(G4VPhysicalVolume* physicalTreatmentRoom)
: motherPhys(physicalTreatmentRoom), // pointer to WORLD volume
detectorSD(0), detectorROGeometry(0), matrix(0),
phantom(0), detector(0),  calorimeter(0), calorimeterSD(0),
phantomLogicalVolume(0), detectorLogicalVolume(0), calorimeterLogicalVolume(0),
phantomPhysicalVolume(0), detectorPhysicalVolume(0), calorimeterPhysicalVolume(0),
aRegion(0)
{
    HadrontherapyAnalysisManager::GetInstance();
    detectorMessenger = new HadrontherapyDetectorMessenger(this);
    sizeOfVoxelAlongX = 1.0 *mm;
    sizeOfVoxelAlongY = 1.0 *mm;
    sizeOfVoxelAlongZ = 1.0 *mm;
  sizeOfPixelAlongX = 0.1 * cm; //carbon bragg peak is much narrower so o get a betar spatial resolution use 50 micror
  sizeOfPixelAlongY = 0.1 * cm;
  sizeOfPixelAlongZ = 0.1 * cm;
```

```
52      // Define here the material of the water phantom and of the detector
53     density_pmma = 1.19*g/cm3;
54     G4Element* elO = new G4Element ("Oxygen", "O", z= 8., a = 16.0 * g/mole );
55     G4Element* elH = new G4Element ("Hydrogen", "H", z=1, a = 1.01 * g/mole );
56     G4Element* elC = new G4Element ("Carbon", "C", z=6., a = 12.01 * g/mole );
57    G4Material* PMMA = new G4Material("PMMA",density_pmma , 3);
58    PMMA -> AddElement(elC, 5);
59    PMMA -> AddElement(elO, 2);
60    PMMA -> AddElement(elH, 8);
61       G4NistManager* man = G4NistManager::Instance();
62    //define BGO
63       G4Element* Ge = man->FindOrBuildElement(32);
64       G4Element* Bi = man->FindOrBuildElement(83);
65       G4Material* BGO = new G4Material("BGO", 7.10*g/cm3, 3);
66       BGO->AddElement(elO , 12);
67       BGO->AddElement(Ge, 3);
68       BGO->AddElement(Bi, 4);
69      G4Element* F = man->FindOrBuildElement("F");
70      //G4Element* Pb = man->FindOrBuildElement("Pb");
71      G4Element* Ba = man->FindOrBuildElement("Ba");
72       G4Material *AIR = man->FindOrBuildMaterial("G4_AIR");
73       G4Material *BariumFluoride = man->FindOrBuildMaterial("G4_BARIUM_FLUORIDE");
74       SetPhantomMaterial("G4_AIR");
75       calorimeterMaterial = BGO;
76       pixelMaterial= BGO;
77       //collimatorlMaterial = Pb;
78       G4cout << G4endl << "The materials defined are : " << G4endl << G4endl;
79       G4cout << *(G4Material::GetMaterialTable()) << G4endl;
80       // Construct geometry (messenger commands)
81       SetCalorimeterSize(50.0*cm, 5.0*cm, 5.0*cm);
82       SetDetectorSize(50.0*cm, 5.*cm, 5.*cm);
83       SetPhantomSize(50.0 *cm, 5. *cm, 5. *cm);
84       SetCalorimeterPosition(G4ThreeVector(0.0 *cm,  675 *mm, 0. *cm));
85       SetPhantomPosition(G4ThreeVector(0.0 *cm, 0. *cm, 0. *cm));
86       SetDetectorToPhantomPosition(G4ThreeVector(0. *cm, 0. *cm, 0. *cm));
87       SetDetectorPosition();
88       UpdateGeometry();
89    }
90    ////////////////////////////////////////////////////////////////////////////
91    HadrontherapyDetectorConstruction::~HadrontherapyDetectorConstruction()
92    {
97
98    ////////////////////////////////////////////////////////////////////////////
99    HadrontherapyDetectorConstruction* HadrontherapyDetectorConstruction::GetInstance()
100   {
103
104   void HadrontherapyDetectorConstruction::ConstructPhantom()
105   {
154
155   void HadrontherapyDetectorConstruction::ConstructDetector()
156   {
```

```
196   void HadrontherapyDetectorConstruction::ConstructCalorimeter()
197   {
238   ////////////////////////////////////////////////////////////////////////////
239   void HadrontherapyDetectorConstruction::InitializeDetectorROGeometry(
240                                                                 HadrontherapyDetectorROGeometry* RO,
241                                                                 G4ThreeVector
242                                                                 detectorToWorldPosition, G4ThreeVector calorimeterToWorldPosition)
243   {
259
260   ////////////////////////////////////////////////////////////////////////////
261   void  HadrontherapyDetectorConstruction::ParametersCheck()
262   {
286
287
288   void HadrontherapyDetectorConstruction::SetVoxelMaterial(G4int j, G4String materialChoice)
289   {
301
302
303   void HadrontherapyDetectorConstruction::SetPixelMaterial(G4int j, G4String materialChoice)
304   {
316
317   ////////////////////////////////////////////////////////////////////////////
318   G4bool HadrontherapyDetectorConstruction::SetPhantomMaterial(G4String material)
319   {
345   ////////////////////////////////////////////////////////////////////////////
346   void HadrontherapyDetectorConstruction::SetPhantomSize(G4double sizeX, G4double sizeY, G4double sizeZ)
347   {
352
353   ////////////////////////////////////////////////////////////////////////////
354   void HadrontherapyDetectorConstruction::SetDetectorSize(G4double sizeX, G4double sizeY, G4double sizeZ)
355   {
361
362   ////////////////////////////////////////////////////////////////////////////
363   void HadrontherapyDetectorConstruction::SetVoxelSize(G4double sizeX, G4double sizeY, G4double sizeZ)
364   {
369   void HadrontherapyDetectorConstruction::SetCalorimeterPosition(G4ThreeVector pos)
370   {
373   ////////////////////////////////////////////////////////////////////////////
374   void HadrontherapyDetectorConstruction::SetCalorimeterSize(G4double sizeX, G4double sizeY, G4double sizeZ)
375   {
381
382   // ////////////////////////////////////////////////////////////////////////////
383
384   void HadrontherapyDetectorConstruction::SetPixelSize(G4double sizeX, G4double sizeY, G4double sizeZ)
385   {
390   ////////////////////////////////////////////////////////////////////////////
391   void HadrontherapyDetectorConstruction::SetPhantomPosition(G4ThreeVector pos)
392   {
395
396   ////////////////////////////////////////////////////////////////////////////
397   void HadrontherapyDetectorConstruction::SetDetectorToPhantomPosition(G4ThreeVector displ)
```

```
397   void HadrontherapyDetectorConstruction::SetDetectorToPhantomPosition(G4ThreeVector displ)
398   {
401
402   ////////////////////////////////////////////////////////////////////////////
403   void HadrontherapyDetectorConstruction::UpdateGeometry()
404   {
521
522
523   void HadrontherapyDetectorConstruction::PrintParameters()
524   {
551
552   void HadrontherapyDetectorConstruction::ConstructSDandField()
553   {
```

2. HadronthearpyDetectorConstruction.hh

HadrontherapyDetectorConstruction.hh

```
#ifndef HadrontherapyDetectorConstruction_H
#define HadrontherapyDetectorConstruction_H 1
#include "G4Box.hh"
#include "globals.hh"
#include "G4VisAttributes.hh"
#include "G4LogicalVolume.hh"
#include "G4UnitsTable.hh"
#include "HadrontherapyDetectorROGeometry.hh"
#include "PassiveCarbonBeamLine.hh"
#include <set>
class G4VPhysicalVolume;
class G4LogicalVolume;
class G4PVPlacement;
class HadrontherapyDetectorROGeometry;
class HadrontherapyCalorimeterROGeometry;
class HadrontherapyDetectorMessenger;
class HadrontherapyDetectorSD;
class HadrontherapyCalorimeterSD;
class HadrontherapyMatrix;
class HadrontherapyLet;
class HadrontherapySteppingAction;
const G4int MaxVoxel = 2000;                // 0 + 2000
const G4int MaxPixel = 1;                  // 0 + 2000
const G4int MaxPixelX = 1;                  // 0 + 2000
const G4int MaxPixelY = 1;
class HadrontherapyDetectorConstruction
{
public:
  typedef std::set<G4VPhysicalVolume*> ScoringPhysVolumes_detector_t;
  typedef std::set<G4VPhysicalVolume*> ScoringPhysVolumes_calorimeter_t;
  typedef std::set<G4VPhysicalVolume*> ScoringPhysVolumes_pixel_t;
  HadrontherapyDetectorConstruction(G4VPhysicalVolume*);

  ~HadrontherapyDetectorConstruction();

public:
static HadrontherapyDetectorConstruction* GetInstance();
  void InitializeDetectorROGeometry(HadrontherapyDetectorROGeometry*,
                    G4ThreeVector detectorToWorldPosition, G4ThreeVector calorimeterToWorldPosition);
  void InitializeCalorimeterROGeometry(HadrontherapyCalorimeterROGeometry*, G4ThreeVector calorimeterToWorldPosition);
  G4VPhysicalVolume* motherPhys;
  HadrontherapyDetectorSD*         detectorSD; // Pointer to sensitive detector
  HadrontherapyCalorimeterSD*         calorimeterSD; // Pointer to sensitive calorimeter
  void ConstructSDandField();
private:

  void ConstructPhantom();
  void ConstructDetector();
  void ConstructCalorimeter();
  void ParametersCheck();
  void CheckOverlaps();
```

```
52  public:
53  // Get detector position relative to WORLD
54  inline G4ThreeVector GetDetectorToWorldPosition()
55    {
56      return phantomPosition + detectorPosition;
57    }
58  // Get detector position relative to WORLD
59  inline G4ThreeVector GetCalorimeterToWorldPosition()
60    {...
63
64  ////////////////////////////////////////////////////////////////////////////
65  // Get displacement between phantom and detector by detector position (center of), phantom (center of) and detector sizes
66  inline G4ThreeVector GetDetectorToPhantomPosition()
67  {...
73
74  ////////////////////////////////////////////////////////////////////////////
75  // Calculate (and set) detector position by displacement, phantom and detector sizes
76  inline void SetDetectorPosition()
77    {...
85  ////////////////////////////////////////////////////////////////////////////
86  // Check whether detector is inside phantom
87  inline bool IsInside(G4double detectorX,
88               G4double detectorY,
89               G4double detectorZ,
90               G4double phantomX,
91               G4double phantomY,
92               G4double phantomZ,
93               G4ThreeVector pos)
94  {...
138 ////////////////////////////////////////////////////////////////////////////
139   G4bool  SetPhantomMaterial(G4String material);
140   void SetVoxelSize(G4double sizeX, G4double sizeY, G4double sizeZ);
141   void SetPixelSize(G4double sizeX, G4double sizeY, G4double sizeZ);
142   void SetDetectorSize(G4double sizeX, G4double sizeY, G4double sizeZ);
143   void SetPhantomSize(G4double sizeX, G4double sizeY, G4double sizeZ);
144   void SetPhantomPosition(G4ThreeVector);
145   void SetCalorimeterPosition(G4ThreeVector);
146   void SetDetectorToPhantomPosition(G4ThreeVector DetectorToPhantomPosition);
147   void UpdateGeometry();
148   void PrintParameters();
149   G4LogicalVolume* GetDetectorLogicalVolume(){ return detectorLogicalVolume;}
150   const G4VPhysicalVolume* GetCalorimeterPV() const;
151   void SetCalorimeterSize(G4double sizeX, G4double sizeY, G4double sizeZ);
152   void SetPixelMaterial (G4int, G4String);
153   void SetVoxelNumber   (G4int);
154   void SetVoxelMaterial (G4int, G4String);
155   G4double GetPixelSizeXY() const         {return sizeOfPixelAlongX;};
156   G4int GetNbOfPixels() const             {return NbOfPixels;}; //mandatory for XrayFluoSD
157   G4int GetNbOfPixelRows() const          {return numberOfVoxelsAlongY;};
158   G4int GetNbOfPixelColumns() const       {return numberOfVoxelsAlongX;};
159   const G4VPhysicalVolume* GetphysiPixel() const {return physiPixel;};
```

```
160     G4Material* GetPixelMaterial() const {return pixelMaterial;};
161     G4Material*        GetMaterial()   {return detectorMaterial;};
162   private:
163     static HadrontherapyDetectorConstruction* instance;
164     HadrontherapyDetectorMessenger* detectorMessenger;
165     ScoringPhysVolumes_detector_t phys_scorers_detector;
166     ScoringPhysVolumes_calorimeter_t phys_scorers_calorimeter;
167     ScoringPhysVolumes_pixel_t phys_scorers_pixel;
168     G4VisAttributes* skyBlue;
169     G4VisAttributes* red;
170     G4RotationMatrix* rotationMatrix;
171     HadrontherapyDetectorROGeometry* detectorROGeometry; // Pointer to ROGeometry
172     HadrontherapyCalorimeterROGeometry* calorimeterROGeometry; // Pointer to ROGeometry
173     HadrontherapyMatrix*             matrix;
174     HadrontherapyMatrix*             matrix_etaInt;
175     HadrontherapyLet*                let;
176     G4Box *phantom , *detector, *calorimeter, *collimator1;
177     G4LogicalVolume *phantomLogicalVolume, *detectorLogicalVolume, *calorimeterLogicalVolume, *collimator1LogicalVolume;
178     G4VPhysicalVolume *phantomPhysicalVolume, *detectorPhysicalVolume, *calorimeterPhysicalVolume, *collimator1PhysicalVolume
179     G4double phantomSizeX;
180     G4double phantomSizeY;
181     G4double phantomSizeZ;
182     G4double detectorSizeX;
183     G4double detectorSizeY;
184     G4double detectorSizeZ;
185     G4double calorimeterSizeX;
186     G4double calorimeterSizeY;
187     G4double calorimeterSizeZ;
188     G4ThreeVector phantomPosition, detectorPosition, detectorToPhantomPosition; //  phantom center, detector center, detector
189     G4double sizeOfVoxelAlongX;
190     G4double sizeOfVoxelAlongY;
191     G4double sizeOfVoxelAlongZ;
192     G4double a;
193     G4double z;
194     G4double sizeOfPixelAlongX;
195     G4double sizeOfPixelAlongY;
196     G4double sizeOfPixelAlongZ;
197     G4int numberOfVoxelsAlongX;
198     G4int numberOfVoxelsAlongY;
199     G4int numberOfVoxelsAlongZ;
200     G4int numberOfPixelsAlongX;
201     G4int numberOfPixelsAlongY;
202     G4int numberOfPixelsAlongZ;
203     G4double volumeOfVoxel, massOfVoxel, volumeOfPixel, massOfPixel;
204     G4Material *phantomMaterial, *detectorMaterial, *calorimeterMaterial;
205     G4String Pb;
206     G4Region* aRegion;
207     G4double density_pmma;
208     G4double density_air;
209     G4ThreeVector calorimeterPosition;
210     G4ThreeVector voxelPosition[MaxVoxel];
```

```
211     //G4ThreeVector voxelPosition;
212     G4LogicalVolume  *voxelLogicalVolume[MaxVoxel];
213     //G4LogicalVolume* voxelLogicalVolume;
214     G4Material*         voxelMaterial[MaxVoxel];
215     G4double            voxelMass[MaxVoxel];
216     G4int            voxelNumber;
217     G4Box*             solidPixel;
218     G4LogicalVolume*   logicPixel[MaxPixel];
219     G4VPhysicalVolume* physiPixel;
220     G4int              PixelCopyNb;
221     G4int              NbOfPixels;
222     G4int              NbOfPixelRows;
223     G4int              NbOfPixelColumns;
224     G4double           PixelThickness;
225     G4double           PixelSizeXY;
226     G4Material*        pixelMaterial;
227   };
228   inline const G4VPhysicalVolume* HadrontherapyDetectorConstruction::GetCalorimeterPV() const  {
231   #endif
```

3. HadronthearpySteppingAction.cc

HadrontherapySteppingAction.cc

```
#include "G4SteppingManager.hh"
#include "G4TrackVector.hh"
#include "HadrontherapySteppingAction.hh"
#include "G4ios.hh"
#include "G4SteppingManager.hh"
#include "G4Track.hh"
#include "G4Step.hh"
#include "G4StepPoint.hh"
#include "G4TrackStatus.hh"
#include "G4TrackVector.hh"
#include "G4ParticleDefinition.hh"
#include "G4ParticleTypes.hh"
#include "G4UserEventAction.hh"
#include "G4TransportationManager.hh"
#include "G4VSensitiveDetector.hh"
#include "HadrontherapyRunAction.hh"
#include "HadrontherapyAnalysisManager.hh"
#include "G4SystemOfUnits.hh"
////////////////////////////////////////////////////////////////////////////
HadrontherapySteppingAction::HadrontherapySteppingAction( HadrontherapyRunAction *run)
{
////////////////////////////////////////////////////////////////////////////
HadrontherapySteppingAction::~HadrontherapySteppingAction()
{
////////////////////////////////////////////////////////////////////////////
void HadrontherapySteppingAction::UserSteppingAction(const G4Step* aStep)
{
G4StepPoint* PreStep = aStep->GetPreStepPoint();
G4StepPoint* PostStep = aStep->GetPostStepPoint();

G4double PreStepX =PreStep->GetPosition().x();
G4double PreStepY =PreStep->GetPosition().y();
G4double PreStepZ =PreStep->GetPosition().z();
G4double parentID =aStep->GetTrack()->GetParentID();
G4double trackID =aStep->GetTrack()->GetTrackID();

G4double PostStepX =PostStep->GetPosition().x();
G4double PostStepY =PostStep->GetPosition().y();
G4double PostStepZ  =PostStep->GetPosition().z();
// positions in the global coordinate system:
//G4ThreeVector posPreStep  = PreStep->GetPosition();
// G4ThreeVector posPostStep = PostStep->GetPosition();
G4TouchableHandle touchPreStep = PreStep->GetTouchableHandle();
G4TouchableHandle touchPostStep = PostStep->GetTouchableHandle();
//To get the current volume:
G4VPhysicalVolume* volumePre = touchPreStep->GetVolume();
G4VPhysicalVolume* volumePost =touchPostStep->GetVolume();
//To get its name:
G4String namePre = volumePre->GetName();
 G4String namePost;

```

```
52  G4String namePre = volumePre->GetName();
53   G4String namePost;
54
55  if(volumePost){
56   namePost = volumePost->GetName();
57       }
58
59  G4int eventNum = G4RunManager::GetRunManager() -> GetCurrentEvent() -> GetEventID();
60  G4double eKin = aStep -> GetPreStepPoint() -> GetKineticEnergy();
61  G4double PosX = aStep->GetTrack()->GetPosition().x();
62  G4double PosY = aStep->GetTrack()->GetPosition().y();
63  G4double PosZ = aStep->GetTrack()->GetPosition().z();
64  G4double MomX = aStep->GetTrack()->GetMomentumDirection().x();
65  G4double MomY = aStep->GetTrack()->GetMomentumDirection().y();
66  G4double MomZ = aStep->GetTrack()->GetMomentumDirection().z();
67  G4double globalTime = aStep -> GetTrack()->GetGlobalTime()/ns;
68  G4String material= aStep -> GetTrack() -> GetMaterial() -> GetName();
69  G4String volume=  aStep->GetTrack()->GetVolume()->GetName();
70  G4Track* theTrack = aStep->GetTrack();
71  G4double VerX = theTrack->GetVertexPosition().x()/mm;
72  G4double VerY = theTrack->GetVertexPosition().y()/mm;
73  G4double VerZ = theTrack->GetVertexPosition().z()/mm;
74  // Jhanna defined it to write the process too
75  G4String process = aStep -> GetPostStepPoint() -> GetProcessDefinedStep() -> GetProcessName();
76  //G4String CPName = theTrack->GetCreatorProcess()->GetProcessName();
77   if((volume=="CalorimeterPhys") && aStep->GetTrack()->GetDefinition()->GetParticleName() == "gamma" && (PreStep->GetStepStatus() == fGeomBoundary)
78     {
79      //if(eKin > .0 ){
80     //G4String CPName;
81     //if(aStep->GetTrack()->GetCreatorProcess()!=0){
82            //CPName = aStep->GetTrack()->GetCreatorProcess()->GetProcessName();
83           //if(CPName == "annihil"){
84       //theTrack->SetTrackStatus(fStopAndKill);
85       std::ofstream WriteDataIn("CalorimeterGamma.txt", std::ios::app);
86       WriteDataIn   <<   eKin            << '\t' << "   "
87             <<   PosX             << '\t' << "   "
88             <<   PosY             << '\t' << "   "
89             <<   PosZ             << '\t' << "   "
90             <<   MomX             << '\t' << "   "
91             <<   MomY             << '\t' << "   "
92             <<   MomZ             << '\t' << "   "
93             <<   globalTime             << '\t' << "   "
94                <<   eventNum          << '\t' << "   "
95             //<<   namePre             << '\t' << "   "
96                //<<   CPName          << '\t' << "   "
97             << VerX << '\t' << "   "
98             << VerY << '\t' << "   "
99             << VerZ << '\t' << "   "
100            <<   G4endl;
101 theTrack->SetTrackStatus(fKillTrackAndSecondaries);}
102  }
```

4. HadrontherapySteppingAction.hh

HadrontherapySteppingAction.hh

```
#ifndef HadrontherapySteppingAction_h
#define HadrontherapySteppingAction_h 1

#include "G4UserSteppingAction.hh"
#include "G4Event.hh"
#include "G4EventManager.hh"
#include "G4ios.hh"
#include "globals.hh"

class HadrontherapyRunAction;
class HadrontherapySteppingMessenger;

#ifndef G4NOHIST
class HepTupleManager;
class HepHistogram;
#endif

class HadrontherapySteppingAction : public G4UserSteppingAction
{
public:
  HadrontherapySteppingAction(HadrontherapyRunAction*);
  ~HadrontherapySteppingAction();

  void UserSteppingAction(const G4Step*);

private:
  HadrontherapyRunAction* runAction;
};
#endif

```

5. PassiveCarbonBeamLine.cc

PassiveCarbonBeamLine.cc

```
#include "G4Box.hh"
#include "G4Tubs.hh"
#include "G4VisAttributes.hh"
#include "G4Colour.hh"
#include "globals.hh"
#include "G4RunManager.hh"
#include "G4LogicalVolume.hh"
#include "G4PVPlacement.hh"
#include "G4PVParameterised.hh"
#include "G4RotationMatrix.hh"
#include "G4NistManager.hh"
#include "G4NistElementBuilder.hh"
#include "HadrontherapyDetectorConstruction.hh"
#include "HadrontherapyDetectorROGeometry.hh"
#include "HadrontherapyModulator.hh"
#include "PassiveCarbonBeamLine.hh"
#include "HadrontherapyDetectorMessenger.hh"
#include "G4SystemOfUnits.hh"
#include "G4ios.hh"
//#include "FaradayCup.hh"
//G4bool PassiveCarbonBeamLine::doCalculation = false;
/////////////////////////////////////////////////////////////////////////////
PassiveCarbonBeamLine::PassiveCarbonBeamLine():
physicalTreatmentRoom(0), hadrontherapyDetectorConstruction(0),
physiBeamLineSupport(0), physiBeamLineCover(0), physiBeamLineCover2(0),
physiKaptonWindow(0),
physiFirstMonitorLayer1(0), physiFirstMonitorLayer2(0),
physiFirstMonitorLayer3(0), physiFirstMonitorLayer4(0),
physiNozzleSupport(0), physiHoleNozzleSupport(0),
physiSecondHoleNozzleSupport(0),
solidFinalCollimator(0),
physiFinalCollimator(0), physiCollimator1(0), solidCollimator1(0)
{
/////////////////////////////////////////////////////////////////////////////
PassiveCarbonBeamLine::~PassiveCarbonBeamLine()
{
    delete hadrontherapyDetectorConstruction;
}
/////////////////////////////////////////////////////////////////////////////
G4VPhysicalVolume* PassiveCarbonBeamLine::Construct()
{
void PassiveCarbonBeamLine::SetDefaultDimensions()
{
/////////////////////////////////////////////////////////////////////////////
void PassiveCarbonBeamLine::ConstructPassiveCarbonBeamLine()
{
    // ------------------------------
    // Treatment room - World volume
    //-------------------------------
    // Treatment room sizes
    const G4double worldX = 400.0 *cm;
    const G4double worldY = 400.0 *cm;
    const G4double worldZ = 400.0 *cm;
```

```
374     G4bool isotopes = false;
375     G4bool checkOverlaps = true;
376     G4Material* airNist =  G4NistManager::Instance()->FindOrBuildMaterial("G4_AIR", isotopes);
377     G4Box* treatmentRoom = new G4Box("TreatmentRoom",worldX,worldY,worldZ);
378     G4LogicalVolume* logicTreatmentRoom = new G4LogicalVolume(treatmentRoom,
379                                                               airNist,
380                                                               "logicTreatmentRoom",
381                                                               0,0,0);
382     physicalTreatmentRoom = new G4PVPlacement(0,
383                                               G4ThreeVector(),
384                                               "physicalTreatmentRoom",
385                                               logicTreatmentRoom,
386                                               0,false,0);
387
388
389     // The treatment room is invisible in the Visualisation
390     logicTreatmentRoom -> SetVisAttributes (G4VisAttributes::Invisible);
391
392     // Components of the Passive Carbon Beam Line
393     //HadrontherapyBeamLineSupport();
394     //VacuumToAirInterface();
395     //ScatteringSystem();
396     //HadrontherapyBeamMonitoring();
397     //HadrontherapyBeamNozzle();
398     //HadrontherapyBeamFinalCollimator();
399   HadrontherapyCollimator1();
400 }
401
402 ////////////////////////////////////////////////////////////////////////////////
403 void PassiveCarbonBeamLine::HadrontherapyBeamLineSupport()
404 {
480
481 ////////////////////////////////////////////////////////////////////////////////
482 void PassiveCarbonBeamLine::VacuumToAirInterface()
483 {
557
558 ////////////////////////////////////////////////////////////////////////////////
559 void PassiveCarbonBeamLine::ScatteringSystem()
560 {
624
625 ////////////////////////////////////////////////////////////////////////////////
626 void PassiveCarbonBeamLine::HadrontherapyBeamMonitoring()
627 {
715
716 ////////////////////////////////////////////////////////////////////////////////
717 ////////////////////////////////////////////////////////////////////////////////
718 void PassiveCarbonBeamLine::HadrontherapyBeamNozzle()
719 {
837
838 ////////////////////////////////////////////////////////////////////////////////
839 void PassiveCarbonBeamLine::HadrontherapyBeamFinalCollimator()
840 {
877
878 //....oooOOOOOooo.....oooOOOOOooo.....oooOOOOOooo.....oooOOOOOooo....
879 ////////////////////////////////////////////////////////////////////////////////
880 void PassiveCarbonBeamLine::HadrontherapyCollimator1()
881 {
882     // Collimator 1
```

```
883         const G4double collimatorlx = .8*mm;
884         const G4double collimatorly = 75.0*mm;
885         const G4double collimatorlz = 2.8*cm;
886         G4bool checkOverlaps = true;
887     solidCollimator1 = new G4Box("Collimator1",
888                                  collimatorlx,
889                                  collimatorly,
890                                  collimatorlz);
891
892     G4LogicalVolume* logicCollimator1 = new G4LogicalVolume(solidCollimator1, collimatorlMaterial, "Collimator1",0,0,0);
893
894
895     //physicalCollimator1 = new G4PVPlacement(0,G4ThreeVector(-32.0*mm,393.8*mm,0.*cm),"Collimator1", logicCollimator1, physicalTreatmentRoom, false, 0);
896
897         for (G4int s =0;s<400;s++)
898         {
899          G4double x2 = ((1+(s-1))* 6 -352)*mm;
900          G4ThreeVector pos = G4ThreeVector(x2,  525 *mm, 0. *cm);
901              new G4PVPlacement(0,pos,"Collimator1", logicCollimator1, physicalTreatmentRoom, false, s);
902             //new G4PVPlacement(0,G4ThreeVector(x2,  525 *mm, 0. *cm);
903         }
904
905         logicCollimator1 -> SetVisAttributes(blue);
906         //darkGreen -> SetForceWireframe(true);
907 }
908
```

6. PassiveCarbonBeamLine.hh

PassiveCarbonBeamLine.hh

```
#ifndef PassiveCarbonBeamLine_H
#define PassiveCarbonBeamLine_H 1
#include "globals.hh"
#include "G4VUserDetectorConstruction.hh"
#include "G4Box.hh"
#include "G4Tubs.hh"
#include "G4VisAttributes.hh"
#include "G4LogicalVolume.hh"
class G4VPhysicalVolume;
class HadrontherapyDetectorConstruction;
class HadrontherapyModulator;
class PassiveCarbonBeamLine : public G4VUserDetectorConstruction
{
public:
    PassiveCarbonBeamLine();
    ~PassiveCarbonBeamLine();
    G4VPhysicalVolume* Construct();
    void HadrontherapyBeamLineSupport();
    // Definition of the beam line support
    // Simulation of the scattering system for the
    // passive spread of the beam
    void ScatteringSystem();
    void VacuumToAirInterface();
    // Definition of the first scattering foil,
    // of the Kapton window, of the stopper
    void HadrontherapyBeamMonitoring();
    // Definition of three monitor chambers
    void HadrontherapyBeamNozzle();
    // Definition of the beam nozzle
    void HadrontherapyBeamFinalCollimator();
    // Definition of the final collimator
  void HadrontherapyCollimator1();
    // The following methods allow to change parameters
    // of some beam line components
        G4Material* kapton;
        G4VisAttributes* redWire;
        G4VPhysicalVolume* mother;
    G4double firstScatteringFoilXPosition;
    G4double firstScatteringFoilYPosition;
    G4double firstScatteringFoilZPosition;
private:
    //passive proton line dimensions
    void SetDefaultDimensions();
    void ConstructPassiveCarbonBeamLine();
    //PassiveCarbonBeamLineMessenger* passiveMessenger;
    G4VPhysicalVolume* physicalTreatmentRoom;
    HadrontherapyDetectorConstruction* hadrontherapyDetectorConstruction;
  //FaradayCup *FC;
    G4double vacuumZoneXSize;
    G4double vacuumZoneYSize;
    G4double vacuumZoneZSize;
```

```
52      G4double vacuumZoneXPosition;
53      G4double kaptonWindowXSize;
54      G4double kaptonWindowYSize;
55      G4double kaptonWindowZSize;
56      G4double kaptonWindowXPosition;
57      G4VPhysicalVolume* physiBeamLineSupport;
58      G4VPhysicalVolume* physiBeamLineCover;
59      G4VPhysicalVolume* physiBeamLineCover2;
60      G4VPhysicalVolume* physiKaptonWindow;
61      G4Tubs* solidStopper;
62      G4VPhysicalVolume* physiStopper;
63      G4LogicalVolume* logicStopper;
64      G4double innerRadiusStopper;
65      G4double heightStopper;
66      G4double startAngleStopper;
67      G4double spanningAngleStopper;
68      G4double stopperXPosition;
69      G4double stopperYPosition;
70      G4double stopperZPosition;
71      G4double outerRadiusStopper;
72      // First scattering foil coupled with the stopper
73      G4Box* firstScatteringFoil;
74      G4VPhysicalVolume* physiFirstScatteringFoil;
75      G4double firstScatteringFoilXSize;
76      G4double firstScatteringFoilYSize;
77      G4double firstScatteringFoilZSize;
78      // Scattering foil coupled with the stopper
79      G4Box* secondScatteringFoil;
80      G4VPhysicalVolume* physiSecondScatteringFoil;
81      G4double secondScatteringFoilXSize;
82      G4double secondScatteringFoilYSize;
83      G4double secondScatteringFoilZSize;
84      G4double secondScatteringFoilXPosition;
85      G4double secondScatteringFoilYPosition;
86      G4double secondScatteringFoilZPosition;
87      G4double innerRadiusFinalCollimator;
88      G4VPhysicalVolume* physiFirstMonitorLayer1;
89      G4VPhysicalVolume* physiFirstMonitorLayer2;
90      G4VPhysicalVolume* physiFirstMonitorLayer3;
91      G4VPhysicalVolume* physiFirstMonitorLayer4;
92      G4VPhysicalVolume* physiNozzleSupport;
93      G4VPhysicalVolume* physiHoleNozzleSupport;
94      G4VPhysicalVolume* physiNozzleSupportHole;
95      G4VPhysicalVolume* physiSecondHoleNozzleSupport;
96      G4Tubs* solidFinalCollimator;
97      G4VPhysicalVolume* physiFinalCollimator;
98    G4VPhysicalVolume* physiCollimator1;
99    G4Box* solidCollimator1;
100     G4VisAttributes* blue;
101     G4VisAttributes* gray;
102     G4VisAttributes* white;
```

```
103     G4VisAttributes* red;
104     G4VisAttributes* yellow;
105     G4VisAttributes* green;
106     G4VisAttributes* darkGreen;
107     G4VisAttributes* darkOrange3;
108     G4VisAttributes* skyBlue;
109     G4Material* beamLineSupportMaterial;
110     G4Material* vacuumZoneMaterial;
111     G4Material* firstScatteringFoilMaterial;
112     G4Material* kaptonWindowMaterial;
113     G4Material* stopperMaterial;
114     G4Material* secondScatteringFoilMaterial;
115     G4Material* layer1MonitorChamberMaterial;
116     G4Material* layer2MonitorChamberMaterial;
117     G4Material* layer3MonitorChamberMaterial;
118     G4Material* layer4MonitorChamberMaterial;
119     G4Material* nozzleSupportMaterial;
120     G4Material* holeNozzleSupportMaterial;
121     G4Material* seconHoleNozzleSupportMaterial;
122     G4Material* finalCollimatorMaterial;
123   G4Material* matW;
124   G4Material* collimator1Material;
125     HadrontherapyDetectorROGeometry* RO;
126 };
127 #endif
128
```

7. Bash script to loop the collimators in the simulation

test.sh

```
1   for i in {1..10}; do
2   mkdir  $i;
3   a='SetCalorimeterPosition(G4ThreeVector(0.0 *cm, ';
4   b='*mm, 0. *cm));';
5   num=$((50*i+475));
6   c="${a} $num ${b}";
7   sed -i -e "s/SetCalorimeterPosition(G4ThreeVector(0.*/$c/g" ../hadrontherapy-allneutron/src/HadrontherapyDetectorConstruction.cc;
8   for j in {1..11}; do
9   mkdir  ./$i/$j;
10  x='G4ThreeVector(x2, ';
11  y='*mm, 0. *cm);';
12  num1=$((50*j+325));
13  z="${x} $num1 ${y}";
14  sed -i -e "s/G4ThreeVector(x2.*/$z/g" ../hadrontherapy-allneutron/src/PassiveCarbonBeamLine.cc;
15  for k in {2..7}; do
16  mkdir  ./$i/$j/$k;
17  m='((1+(s-1))*';
18  n='-352)*mm;';
19  num2=$((k));
20  o="${m} $num2 ${n}";
21  sed -i -e "s/((1+(s-1)).*/$o/g" ../hadrontherapy-allneutron/src/PassiveCarbonBeamLine.cc;
22  make -j272;
23  ./hadrontherapy carbon_beamline.mac;
24  mv CalorimeterGamma.txt ./$i/$j/$k;
25  cp ../hadrontherapy-allneutron/src/HadrontherapyDetectorConstruction.cc ./$i/$j/$k;
26  cp ../hadrontherapy-allneutron/src/PassiveCarbonBeamLine.cc ./$i/$j/$k;
27  done
28  done
29  done
30
```